Structural Health Monitoring of a Reinforced Concrete Beam Using Finite Element Analysis

BY

Shafique Ahmed
Bachelor of Science in Civil and Environmental Engineering
Shahjalal University of Science and Technology, Sylhet, Bangladesh

SUBMITTED IN PARTIAL FULFILLMENT OF THE REQUIREMENTS
FOR THE DEGREE OF MASTER OF SCIENCE
DEPARTMENT OF CIVIL AND ENVIRONMENTAL ENGINEERING
UNIVERSITY OF MASSACHUSETTS LOWELL

Signature of the Author .....
Department of Civil and Environmental Engineering
March, 2013

Signature of Thesis Supervisor .....
Tzu-Yang Yu
Assistant Professor

Committee Member Signature .....
Professor Peter Avitabile
Department of Mechanical Engineering

Committee Member Signature .....
Professor Susan Faraji
Department of Civil and Environmental Engineering

Committee Member Signature .....
Professor Christopher Niezrecki
Department of Mechanical Engineering

Structural Health Monitoring of a Reinforced Concrete Beam Using Finite Element Analysis

BY

Shafique Ahmed
Bachelor of Science in Civil and Environmental Engineering
Shahjalal University of Science and Technology, Sylhet, Bangladesh

ABSTRACT OF A THESIS SUBMITTED TO THE FACULTY OF THE
DEPARTMENT OF CIVIL AND ENVIRONMENTAL ENGINEERING
IN PARTIAL FULFILLMENT OF THE REQUIREMENTS
FOR THE DEGREE OF
MASTER OF SCIENCE
UNIVERSITY OF MASSACHUSETTS LOWELL
2013

Thesis Supervisor: Tzu-Yang Yu
Title: Assistant Professor

Abstract

Damage assessment and condition evaluation of existing civil infrastructure systems are essential to the decision making in routine structural maintenance and disaster remediation. To determine internal conditions using surface strain measurement is a critical, real-life engineering problem, in view of the popularity of using surface strain measurement for structural health monitoring. The objective of this study is to develop a damage detection methodology to relate surface measurement (e.g., strain) with the internal condition (e.g., healthy or damaged) of structures using a singly-reinforced concrete beam as an example. Numerical approach is applied in conducting a parametric study in this research. A finite element model of a benchmark singly-reinforced concrete beam specimen was created using a commercial finite element analysis package, ABAQUS®. The model was validated in laboratory four-point bending test, using fiber optic strain sensor measurement. Artificial damages were modelled by rebars volume reduction, and four types of artificial damages are considered. From the simulation results, relationships between the change in surface strain and intensity of internal damage are developed. It is found that damage introduced in the rebar embedded in a reinforced concrete beam can be accurately located using the surface stress difference. Nonsymmetric damages yield more contour area of surface stress change than the symmetric damages.

Acknowledgements

I would like to thank everyone who has supported and assisted me throughout my graduate studies.

I am grateful to Professor Tzu-yang Yu for his guidance, generosity, and for his continuous encouragement to a higher standard of work. I also appreciate the help of other committee members, Professor Peter Avitabile, Professor Susan Faraji, and Professor Christopher Niezrecki, in reviewing my thesis. I would like to extend my sincerest thanks to Professor Xingwei Wang for her support. I would also like to thank current and formal students Christopher Nonis, Xiaotian Zou, Jiansheng Ouyang, Carlos Jaquez, Alice Chao, Jeremiah K. Otchere-Nyarko, Justin Wilson, Ross Gladstone, Hao Liu, and CheFu Su for their continuous support.

I am also grateful to the U.S. Department of Transportation (DOT) Research and Innovative Technology Administration (RITA) for their support of this work.

And last but not least, I would like to thank my family and friends for their support and encouragement.

Contents

List of Figures

List of Tables

Chapter 1

Introduction

Civil infrastructure systems are built to be sustainable for many years. Structural damages can occur by mistakes in planning and construction, and due to aging of materials, excessive use, overloading, severe climate conditions, inadequate maintenance, and chemical attacks. Damage assessment and condition evaluation of existing civil infrastructure systems are essential to be decision making in routine maintenance and disaster remediation. Many nondestructive techniques are available to detect damages in structures, including visual inspection (*e.g.*, boroscope and binocular), optical (*e.g.*, optical fiber, speckle, infrared thermography, and endoscopic), digital image correlation (DIC) techniques, acoustic emission, electromagnetic, and ultrasonic. Measurable quantities by nondestructive testing sensors are: a) mechanical quantities (*e.g.*, displacement, length, volume, acceleration, and strain), b) thermal quantities (*e.g.*, temperature and heat), c) electromagnetic/optical quantities (*e.g.* frequency and magnetism), and d) chemical quantities (*e.g.*, moisture and pH value). In this study, measurements of mechanical quantities (surface strain) is used to determine internal damage in a structure.

Strain studies in civil structures are pivotal in avoiding unexpected catastrophic failures. Over the past few decades, fiber optic sensor (FOS) and DIC have emerged as suitable, accurate, and cost effective tools for strain measurement. FOS can measure surface and subsurface strains, while DIC can only measure surface strain. For example, Maalej *et al.* (2004) [21] demonstrated the feasibility to monitor corrosion-induced damage in reinforced concrete (RC) structures using embedded FOS where visual inspection is not possible. Another example, Kenel *et. al.* [15] measured strain in rebars throughout the length of a RC structure; any unusual strain at a location indicates the presence of damage. However, the commercial use of embedded FOS started in last decade of twentieth century [35]. Thus, there are many structures without embedded FOS. In addition, installation and maintenance of embedded FOS are expensive and tedious. For existing structures, surface strain can be precisely measured by FOS. DIC can also measure surface strain in a zone of interest. But structural health of RC structures depends on the internal condition. To determine internal condition using surface strain measurement is a critical, real-life engineering problem.

In this research, the determination of the internal condition of a RC beam using surface strain measurement is an inverse problem. In solving inverse problems, knowledge developed from solved forward problem is necessary. As described by Kubo (1988) [17], a direct problem involves determining the response of a system given the following information: the domain of a problem and its boundaries, governing laws or equations, and the boundary conditions and forcing functions. In practice, this informa-

tion may not be complete, making a direct analysis of a problem infeasible. However, if additional information, such as a prescribed system response, is specified, an inverse problem is constructed to determine the required input for the direct problem. An inverse problem can be solved using a theoretical approach, experimental approach, and numerical approach. The numerical approach is suitable for parametric studies. The parametric studies develop knowledge for solving an inverse problem using solutions of forward problem.

In numerical approach for damage detection, measurements of system variables such as displacement and strains are available, while the physical properties of the system itself are unknown. Typically, the solution of inverse problems consists of an iterative process with multiple solutions of changing forward problem. It is expected that the iterative process will converge to the true solution by minimizing the error between the predicted and measured quantities (geometry of the structure).

Therefore, it is advantageous to determine internal damages in a structure using surface measurements and a numerical approach.

1.1 Research Objective

The research objective of this study is to develop a damage detection methodology to relate surface measurement (e.g., strain) with internal conditions (e.g., healthy or damaged) using a singly RC beam as an example.

1.2 Thesis Approach

This study proposes a condition assessment methodology to identify, locate, and quantify internal damages in a RC structure using surface strains. A commercially available FE package, widely used ABAQUS® is used to create finite element models of RC structures for the numerical simulation advantages.

In the first phase of the study, a FE model of a benchmark beam specimen, a singly RC beam, is developed using ABAQUS®. In the FE model, the concrete section is considered to be homogenous, uniform and intact (no initial cracks) throughout the length of the RC beam. Three dimensional rebars are modelled in the continuum concrete section.Linear material properties are considered in FE models. Strains obtained from the FE model are compared with the theoretical calculations. To validate the FE model experimentally, a series of four-point bending tests is designed.

A benchmark RC beam specimens is constructed to perform the series of four-point bending tests. In four point bending tests, a monotonic cyclic load is applied on the simply supported benchmark RC beam. The maximum load in the monotonic cyclic loading is selected in such a way that internal moment due to applied load in critical section of the benchmark beam specimen is kept below the theoretically calculated cracking moment. The testing involves measuring the surface strains using FOS and DIC techniques during the cyclic monotonic loading. FOSs are installed at several discrete points in compression zone of the benchmark beam specimen and DIC system is

used to measure on plan (perpendicular to cross-sectional area of the specimen) surface strains.

The physical parameters of the tested benchmark beam specimen (Young's modulus, density, geometric dimensions, etc.) are updated in the FE model. In addition, the mesh sizes, support conditions, and loading conditions of the FE model are tuned such a way that it can generate results (strain/stress magnitude in longitudinal direction) tended to experimental measurements. To select the mesh size computational expenses and research objectives are carefully preserved. Eventually, the FE model is validated by the experimental results.

In the second phase, in the validated FE model, artificial internal damages in the benchmark beam specimen are introduced by reducing rebar cross sections. An area (zone) of interest is selected on the surface of FE model which is perpendicular to damaged rebars. The surface stresses on the area of interest are mapped from both intact and damaged models which created two stress matrixes for each case of damage, and then subtraction of stress matrixes yielded a matrix of surface stress differences. From the matrix of surface stress differences, a contour area below a certain surface stress difference and maximum surface stress difference are found. By considering many damage cases, the area of contour and pick stress difference are presented as functions of rebar volume reductions in percentile. Another correlation is established between contour volume of stress differences and rebar volume reductions.

In this research, the research tasks are

- To develop a FE model of an intact RC beam
- To construct the RC beam and experimentally measure surface strains using FOS and DIC
- To validate the FE model using the experimental surface strain measurements
- To develop damaged RC beam models by introducing damages on steel rebars in validated FE model of RC beam
- To determine relationships between surface strain change and internal artificial damage intensity using simulated results
- To propose a damage detection methodology to detect internal damages in RC structures

Fig. 1-1 illustrates the research activities required to solve the inverse problem of detecting internal damage in a RC structure using surface strain measurement.

1.3 Organization of the Thesis

The organization of this thesis is in the following.

Chapter 2 reviews the literature related to the research objective. The literature review is divided into three parts. First, to survey suitable methodologies for solving inverse problems corresponding to determine internal/subsurface condition using surface information. Secondly, investigate the applicability and reliability of FE commercial

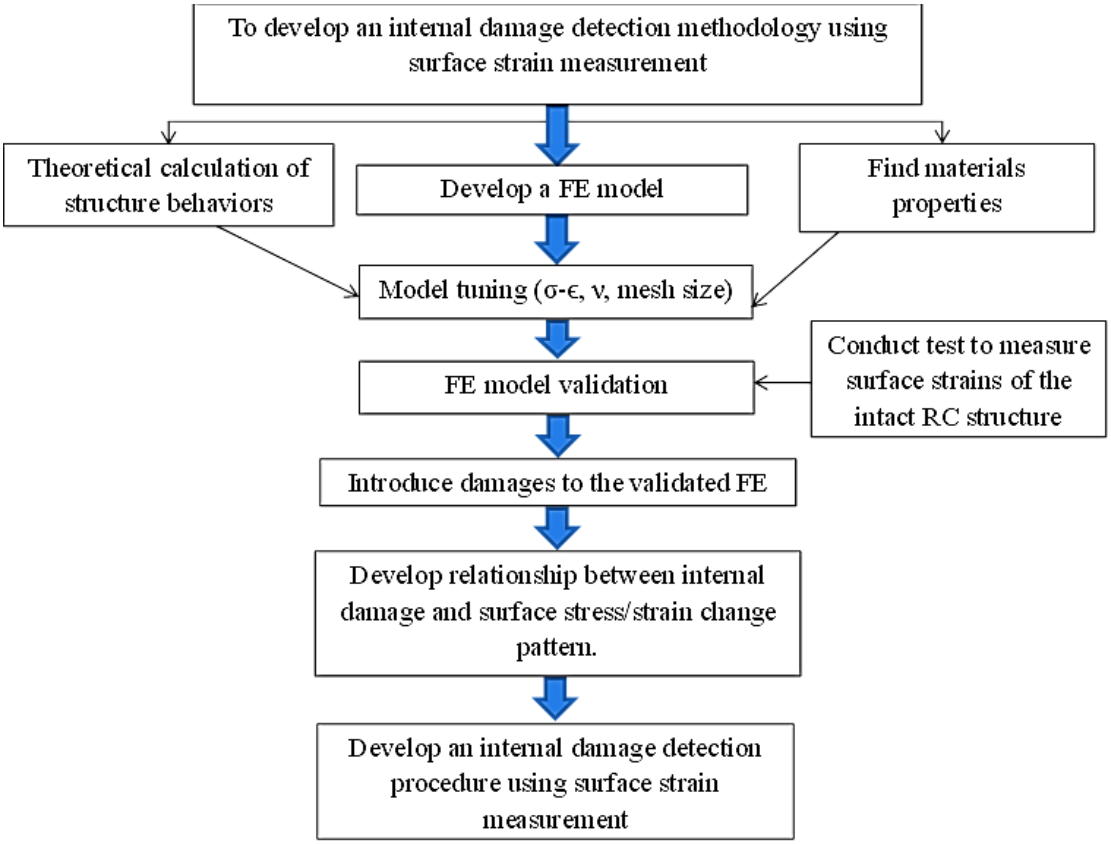

Figure 1-1: Research roadmap

packages (particularly ABAQUS®) for simulating RC structures under bending test. In addition, review material parameter extraction methods using the standard material tests. Thirdly, survey measurement techniques (FOS and DIC techniques) for detecting surface strain precisely.

Chapter 3 describes modelling strategies of a RC beam, development of damaged RC beam models by introducing artificial damages on steel rebars in a RC beam using ABAQUS®. Geometry, meshing scheme, boundary conditions, and material properties are discussed in the strategy part.

Chapter 4 describes specifications and manufacturing procedure of a RC beam. It also contains the description of materials testing and four-point bending tests.

Chapter 5 reports experimental and numerical results. Validation of FE model (intact RC beam) is included. Simulated responses of artificially damaged models are discussed. From the FE analysis results, relationships are developed between the change in surface strain-field/stress-field and intensity of internal damages.

Chapter 6 summarizes research findings, contributions and the future work in this study.

Chapter 2

Literature Review

2.1 Introduction

The literature review is divided into three parts. First, to survey suitable methodologies for solving inverse problems corresponding to determine internal/subsurface condition using surface information. Secondly, investigate the applicability and reliability of FE commercial packages (particularly ABAQUS®) for simulating RC structures under bending test. In addition, review material parameter extraction methods using the standard material tests. Thirdly, survey measurement techniques (FOS and DIC techniques) for detecting surface strain precisely.

2.2 Internal Damage Assessment:

As described by Kubo (1988) [17], a direct problem involves determining the response of a system given the following information: the domain of a problem and its bound-

aries, governing laws or equations, and the boundary conditions and forcing functions.In practice, this information may not be complete, making a direct analysis of a problem infeasible. However, if additional information, such as a prescribed system response, is specified, an inverse problem may be constructed to determine the required input for the direct problem. Researchers used both numerical and theoretical approaches to solve the inverse problem.

1. Wang *et. al.* (2001) [34] studied damage identification algorithm using static test data and change in natural frequencies. They used damage signature matching (DSM) techniques to locate damage in structures by properly defining measured damaged signatures (MDS) and predicted damage signatures (PDS).

   A beam with two fixed ends and planer truss in damaged and intact conditions were used in experiments and FE simulation. In experiment, static displacement at different locations in the structures were measured at different loading conditions. The experimentally obtained results were de-noised using wavelets from MATLAB® and compared with numerically obtained results. Damage location was determined using normalized damaged index (NDE).

2. Nazmul *et. al.* (2007) [25] studied practical and theoretical approaches to measure crack opening displacement (COD) and rebar force of a reinforced concrete (RC) beam. A theoretical derivation proposed by the author in 2003 was used to compute a theoretical COD profile, and a practically measured COD profile was yielded from the image analysis. The rebar force was calculated using the inverse analysis of practical and theoretical CODs. Rebar location was determined from

the calculated rebar force. A four point bending test was performed to illustrate the applicability of the method.

A size of 10cm x 10cm x 40cm, eight RC beams were casted in laboratory for the study. Compressive strength of concrete (f_c') and tensile strength of deformed steel rebar (f_y) were determined 30 MPa (4.35 ksi) and 345 MPa (50 ksi) respectively. The RC beams were casted under reinforced using two 6mm diameter steel rebars. 20mm side cover was provided, when clear cover varied 25-35 mm among the specimens. 3mm wide and 10mm depth notches were created at bottom face of the RC beams to ensure the crack location at middle.

A displacement controlled universal testing machine was used to perform four-point static bending tests. Service loading range was split by several intervals (16.9 kN, 18.9 kN, 24.6 kN, and 27.9 kN) to take pictures by microscope. Raw COD data computed from image analysis were filtered (linear) to get smoothened COD profile. Theoretical COD profile was computed from fracture mechanical approach proposed by author in 2003. Analytical solution also presented considering addition of slippage of steel rebar. Moreover, the integral solution also computed by using numerical to get numerical solution. To calculate rebar force, the author used his proposed method to solve inverse problem. The rebar force also computed from the practical CODs. A peak rebar force indicates the center of a rebar.

Practically obtain CODs depends on the image resolution, when computed rebar force accuracy depends on accuracy of CODs data, accuracy in prediction of material properties and correct choice of regularization parameters. The proposed

method should be applicable to health monitoring of existing structures; since COD and rebar force estimation do not depend on cross sectional parameters in the proposed method.

3. Nazmul *et. al.* (2004) [24] applied inverse analysis to obtain a rebar force from a surface measurement of crack opening displacement (COD) using fracture mechanics base approach for a reinforced concrete beam. Embedded sensor can measure rebar force. The proposed method is applicable to obtain rebar force of the structure without embedded sensor. For the first time, COD was used to obtain the re-bar force without cross sectional details of a structure. The method efficiency was demonstrated in a numerical example.

   To generate crack profiles using Castigliano's theorem, weight function (to determine stress intensity factors), and Heaviside step function (to obtain distribution of bridging stress), several assumptions were made: (i) linear elastic materials response, (ii) total stress transformation occurs between steel and concrete between two crack surfaces, (iii) ignore all micromechanical parameters, (iv) bridging stress due to post peak strain softening was neglected. Computation of variation of strain energy functional with an imaginary point loading at any location yielded crack profiles in a RC beam. An inverse analysis was used to obtain rebar forces. Since the transformation of COD and rebar force was opposite of an integral function; thus a small error in COD can induce an unacceptable error in rebar force values.

   A RC beam with a cross section of 250mm x 554mm, and three layers of steel

were used in a numerical example. Steel cross sections of three layers were 900 mm^2, 400 mm^2, and 200 mm^2 with concrete clear covers of 25 mm, 65 mm, and 101mm respectively. A RC beam section was cracked under a pure bending of 176 kN-m, when 20 MPa compressive strength of concrete and 200 GPa Young's modulus of elasticity were considered. Crack profiles were determined using forward analysis. Depressions were observed at rebar locations in COD profile. Random numbers of Gaussian distribution were added to generate noisy COD profiles with error at a range of 1.32% to 7.25%. Using Tikhonov method, the rebar forces were calculated from noisy COD profiles.

It was revealed that higher noise in COD introduced higher inaccuracy in re-bar force calculation using inverse analysis (e.g., very lower level of noise retrieved the exact stress obtained from the theoretical calculation using a forward analysis). Since rebar calculation was highly sensitive to COD profile noise level, high accuracy sensor should be used to acquire data and thereafter an accurate analysis process to retrieve CODs from the field measurement. The study was limited in terms of considering ideal case of single edge cracked specimen, and monotonic loading condition.

4. Cox *et. al.* (1991) [6] applied inverse analysis method to obtain bridging stress (p)-opening displacement (u) using Tikhonov regularization when p was considered to be a continuous function of u. The feasibility of the method was demonstrated in a simulation using synthetic data. Since the original function $p(u)$ was known as it was numerical simulation, the accuracy of the inverse problem was

easily assessable.

A convenient formula,$u(x) = \frac{4}{E}\int_x^c \int_0^5 G(t,s,w)\sigma_a(t) - [p[u(t)]or\varphi(t)]dtG(x,s,w)ds$, where 2c is the crack length, w is specimen dimension, E' is combination of elastic constant, G is a weight function obtainable from handbooks for specimen, was linearize by expanding, $P(u) = \sum_{i=0}^{n} \alpha_i f_i(u)$ where $\{fi\}$ is Legendre polynomials and $\{f_i\}$ is coefficients. To obtain i experimental data, $\{x_j, u_j, j = 1, 2,.....\}$ need to use; the experimental data always contain some level of experimental noise. But the solution of α_i is very sensitive to noise level, even in some case unstable. Tihonov's regularization was used to overcome the difficulty.

A numerical simulation was performed to illustrate the feasibility of proposed method using synthetic data. In the numerical simulation, some known typical function $p(u)$ was used. Gaussian distribution, zero mean value with a varying width (w), was added to simulate experimental noise in u_j. Two different crack patterns were considered in the numerical testing i) cracks without notches, and ii) cracks growing from a notch. Bridging track was successfully obtained from a noisy data. Accuracy to obtain p(u) was reasonably accurate when noise level w ≈ 0.01 in both cases of cracks without notches and cracks growing from a notch. For a large crack, such as crack mount opening displacement of a 3" straight edge crack in typical reinforced concrete is approximately 3mm, is liberal. In case of experimental data, Monte Carlo approach is a viable and straight forward method to estimate the accuracy due to unavailability of $p(u)$ function.

The above survey show that theoretical solution requires very precise local measurement when location of interest is known or given [25, 24]. But numerical result can predict the global response. Recently, sensitivity-based FE updating methods, which overcome the limitations of the direct methods, have been frequently used for damage identification purposes [34].

2.3 FE Modelling of RC Beam

Creating numerical model of RC structures is complicated due to the followings:

- RC structures are made up of two different materials, concrete and steel, which have different physical and mechanical properties.
- Concrete mechanical properties are complicated. For example, compressive and tensile stress behavior of concrete under uniaxial, biaxial, and triaxial are different.
- Interaction of reinforcing rebars and concrete is complex in terms of bond-slip and aggregate interlocking.

Researchers used ABAQUS®, a commercial FE package, to study behaviors of RC beam structures. FE models were validated using experimental results.

1. Sinaei *et. al.* (2012) [30] studied numerical solution of behavior of RC concrete beam using commercial finite element package ABAQUS®. They validated the FE model using experimental results. The experiment was conducted by Kachlakev *et. al.* (2001) [13].

In this study, they modeled the RC beam used in the experiment. The RC beam was 6095mm long with 770mm x 305mm uniform cross-sectional area. The beam had only longitudinal reinforcement (main rebars, no shear rebar). The beam was subjected to four-point bending where the effective span was 5485mm and 1825mm apart concentric loads were applied symmetrically.

An elastic perfectly plastic material was used for the steel bar with equal behavior in tension and compression as proposed by Li *et. al.* (2006) [20] and Poisson's ratio was assigned to be 0.3. The transfer of load across the concrete cracks through the rebars was defined by tension stiffening proposed by Hu et al (2010) [12]. The concrete damaged plasticity model proposed by Lee and Han (1998) [19] was used to simulate concrete material behavior in the inelastic range.

All the elements in the model were meshed in a same size that ensured sharing of same node by two different materials. 3-D solid, C3D8R, and 2D truss, T3D2 were selected as mesh element for concrete box and rebar, respectively.

FE result such as displacement, tension strain of the main rebars, compression strain of concrete and crack pattern had good agreement with experimental results.

2. Alih *et. al.* (2012) [1] studied tension stiffening behavior of a RC beam where reinforcing was provided by inoxidable (stainless) steel rebars. FOS was installed to measure strains of embedded rebars in the RC beam during a four-point bending test. A FE model of the RC beam was developed using ABAQUS®. FE simulation results were compared with experimental result to verify the tension

stiffening numerical model used in the FE model.

The RC beam specimen size was 150mm x 280mm x 2950mm. 2-ϕ20 rebars in tension zone and 2-ϕ8 stainless steel rebars in compression zone were placed. Reinforcement of the beam also included shear reinforcing. Both of the rebars in tension zone were equipped with FOSs at six different locations throughout the length. The RC beam specimen was subjected to a four-point bending test. Loading condition in the test were 2700mm effective span and equally spaced two concentrated load at the mid-span. The maximum loading level was 80kN. Displacement at the mid-span of the RC beam specimen was recorded using LVDT. All six fiber optic strain sensors were used to measure strain on embedded rebars. To simulate the material property of stainless steel, experiments were conducted to obtain full scale stress-strain behavior of two types of stainless steel. They proposed a numerical models to obtain full scale stress-strain diagrams of the the stainless steels. The numerical models were compared with the Ramberg-Osgood models [32]. The transfer of load across the concrete cracks through the rebars was defined by tension stiffening proposed by Rim and Hayder (1998) [28].

ABAQUS®standard version 6.4 was used to model the beam. 8-node 3-D solid element was select to model concrete box and 2-node embedded bar was used to simulate rebars in the structure. Meshing scheme was selected such way that the model produced 396 elements.

Experimental results (e.g., displacement at the mid-span and strains from six fiber optic strain gauges) were compared with numerically obtained results. Strains obtained from FE simulation were higher than the experimental results, since the

tension stiffening model only considered input parameter of concrete strength rather than the actual behavior of interaction between rebars and concrete.

3. Wahalathantri *et. al* (2011) [31] studied numerical modelling of material properties for a commercial FE package, ABAQUS®. The models were validated using different experimental results of RC beam structures.

   Experimentally verified Hsu and Hsu (1994) [11] numerical method was used to obtain complete stress-strain curve for concrete under uniaxial compression.

$$\sigma_c = \frac{\beta\frac{\epsilon_c}{\epsilon_o}}{\beta - 1 + (\frac{\epsilon_c}{\epsilon_o})^{\beta}}\sigma_{cu} \tag{2.1}$$

   where,

$\beta = \dfrac{1}{1 + \dfrac{\sigma_{cu}}{\epsilon_o E_o}}$

$\epsilon_o = 8.9 \times 10^{-5}\sigma_{cu} + 3.28312 \times 10^{-3}$

$E_o = 1.12432 \times 10^{2}\sigma_{cu} + 3.28312 \times 10^{3}$ β = A dependent parameter

ϵ_o = Strain at peak stress

E_o = Peak tangential modulus

σ_c= compressive stress value

σ_{cu}= ultimate compressive stress

ϵ_c= compressive strain

   Required parameters (*e.g.*, inelastic strain, damage parameter, plastic strain) to simulate nonlinear behavior of concrete in ABAQUS® were obtained from the

following expressions:

$$\epsilon_c^{in} = \epsilon_c - \epsilon_{oc}^{el} \tag{2.2}$$

$$\epsilon_c^{pl} = \epsilon_c^{in} - \frac{d_t \sigma_c}{(1 - d_t) E_o} \tag{2.3}$$

$$d_t = \frac{\epsilon_c^{in}}{\epsilon_c} \tag{2.4}$$

where, $\epsilon_{oc}^{el} = \frac{\sigma_c}{E_o}$, inelastic strain = ϵ_c^{in}, and plastic strain = ϵ_c^{pl}

To validate Eq. (2.3) in the FE package the ϵ_c^{pl} have to be increasing and positive when σ_c is increasing. They used tension stiffening model proposed by Nayal and Rasheed [27] with a minor modification.

Load vs. displacement results of a three point bending test of a RC beam were reported by Peeters et al (2006) [26]. In his loading configuration the RC beam was supported at 1.2m distance from either of the edges and loaded at the centre. The compressive strength of concrete was 51.2 MPa. A FE model of the beam was created using ABAQUS®. Material properties was obtained from the numerical model of material properties (e.g. stress-strain under uniaxial loading, tension stiffening behivor) were used in the FE model. The FE modeling results and test results showed good agreement.

A four-point bending test reported by Maeck (2003) [22] were also used to validate the FE model. RC beam was supported at 1.15m and 5.85m and loaded at 2.0m and 4.0m from the of the left edges of the beam with 4kN point load. The reported experimental results and FE model result had good agreement.

The input from numerical models of material properties performed well by vali-

dating FE model of the reported [22, 26] three-point and four point bending tests.

FE model can simulate the behavior of RC beams. FE model results (e.g., displacement and strain) shows good agrement with experimental result. The literature study also shows that a FE model can simulate strain pattern on embedded rebars.

2.4 Surface and Subsurface Strain Measurement Techniques:

FOS can be used to measure external as well as internal strain of a structure element on discrete points or on a line when DIC system can measure strain on a plane. In addition, the DIC system can also measure out of plane strain.

2.4.1 FOS

1. L. Deng and C.S. Cai (2007) [8] performed a literature review on applications of FOS in civil engineering.

   Typical FOSs were classified in three types:1) strain sensors, 2) crack sensors, and 3) corrosion sensors. Many researchers used crack sensors to measure crack opening displacement, detection of formation of cracks, and crack locations etc. Strain sensors are used to measure strain either by embedding or attaching onto surface of structures or test specimens. It had been proved that FOSs can successfully measure strains below 4000$\mu\epsilon$. It is also noteworthy that the difference between FOSs and ESGs were always below 5% in different observations.

In this literature reviews, they (authors) mentioned several existing problems with FOSs: (1) strain and temperature discrimination, (2) effects of coating materials on strain measurement, (3) the bonding of FOSs, and (4) effect of embedded optical fibers on properties of the hos material.

2. Yang *et. al.* (2009) [35] proposed several packaging and embedding in concrete techniques. Performances of pre-embedded FOS in concrete specimens were evaluated by one-dimensional and two-dimensional press experiments.

   Three types of pre-embedded bar sensors were introduced: (1) steel bar sensor, (2) epoxy bar sensor, and (3) concrete bar sensors. Concrete bar sensors shapes could be regular rectangular, cylindrical, corrugated rectangular and cylindrical corrugated etc. A 25mm x 25mm x 120mm concrete bar sensor with 100mm fiber gauge length was embedded in a 100mm x 100mm x 300mm concrete specimen. A testing machine was used to conduct one-dimensional press test. Also, 160mm x 160mm x 160mm specimen was used to conduct two-dimensional press test. Theoretical prediction and mechanical behavior of concrete had a good agreement.

   Practical pre-embedded FOSs were successfully installed and tested. However, this paper also mentioned that in laboratory, it is possible to directly embed the FOS within concrete specimen or structures.

3. Kesavan *et. al.* (2010) [16] proposed a technique to embed FOS in concrete, and evaluate the efficient of the proposed method.

   Two types of embedment techniques (protective measures) were introduced: (1)

steel rod encapsulation, and (2) cast epoxy sheet encapsulation. In first technique, a 10mm FOS sensor was protected by a 60mm long steel tube with flanges and relevant sealing materials. The flanges were made of 4mm thick 25mm diameter steel dishes. Both types of embedment techniques were applied to embed FOSs in the cores of 150mm diameters and 300mm long cylinders. The cylinders also were equipped with Electrical Resistance Strain Gauges (ERSG). Standard compression tests and high-stress, low-cycle loading test were performed using an UTM to measure strain at core and surface. Also, grad M45 cylinders along with embedded sensor were used to perform fatigue test using servo-controlled UTM; where loading range was 8.49 to 14.1 MPa at a frequency of 10 Hz. In addition, sensors were embedded in a 150mm x 200mm x 1500mm beam to perform bending test to measure internal strain when surface strain was measured using electrical resistance strain gauges.

In compression test, the embedded sensors measured maximum 2000$\mu\epsilon$ and showed only within 1% deviation with ERSGs measurement of strain up to the elastic limit. In fatigue test, 2% variation was found between the measurements of strain from embedded FOSs and ERSGs. 2 million cycles were used to assess the evaluation of FOSs. In high-stress, low-cycle loading test, FOSs were measured strain up to 1500$\mu\epsilon$ In beam test, the deviation of 7% was found between the measurement of FOSs and ERSGs. All in one, the embedded FOSs using both of techniques were performing well in axial compression test, high-stress low-cycle loading test, fatigue test, and bending test.

4. Kenel *et. al.* (2005) [15] measured strains along reinforcing bars embedded in a reinforced concrete beam subjected to four-point bending using wavelength multiplexed optical fiber brag grading sensors. Bond shear stress between rebar and concrete was calculated using stress gradient along the rebar and compared it with three bond shear stress-slip model. Moreover, a deflection calculation method of partially cracked beams was proposed, providing lower and upper bounds corresponding to maximum and minimum theoretical crack spacings, respectively.

   A 4000mm long along with a 1000mm x 200mm uniform cross section through the length reinforced concrete beam was used in four-point bending. Both lateral, mm @ 300mm c/c, and longitudinal, 4- mm, reinforcement was provided. An optical fiber with a total 286 Bragg grading spacing at 10.4mm was installed onto one 10mm rebar. A 1mm long and 1mm wide groove was created along the 10mm rebar to epoxy-glue the fiber. The beam was placed upside down; supports were provided 600mm apart from the centerline and a deformation controlled loading system were placed to load the beam 200mm from each edge of the beam. Loading was divided into 14 loading stages (24.4kN maximum). Each loading stage crack widths and deflection were measured by demountable strain gauges (deformeters). At the beginning and end of each loading stage, fiber-optic strain measurements were taken.

   Optical fiber Bragg grating sensor successfully measured maximum strain, 2800$\mu\epsilon$ (28 millistrains), and maximum strain gradient, 2 millistrain per millimeter. Theoretical, tension cord model, and experimental deflection values were in good agreement. An additional suggestion to minimize the eccentricity effect in ex-

perimental measurements was made: sensors should be used in symmetric pair creating two groves opposite of each other in a rebar.

2.4.2 DIC

1. Mulle *et. al.* (2009) [23] studied mechanical behavior of a composite beam under bending tests by using different techniques. They also used FEA to compare results with experimental results. Prime objective of the study was to compare global and local mechanical measurements obtained from different techniques for instance FBG, DIC, and FEA.

   A beam type specimen was used to execute 3 and 4 points load tests. The specimen was made of a carbon/polymeric Hexply M21 T700. 300 mm long specimen had central reinforced zone and thinner side zone. The central reinforced zone was constructed by 28 plies (7.7 mm thick), on the other hand thin latter zone thickness was 5.6 mm which contained 20 plies. Laminated FBGs were installed in 4 different layers during stacking. 3 and 4 points bending test were executed on the test specimen by using Instron mechanical testing machine. The testing machine accuracy precision was 10-6. Loading measurement was taken for each 2mm displacement, the process continued until the upper cylinder displacement of 16mm. Two rigid bound cameras, Quimaging Retiga 1300 CCD, captured digital images, 1280 x 1024 pixel resolution, in each 2mm displacement interval. 3-D digital image correlation technique was implemented by using Vic-3D commercial software. SAMCEF software was used to execute three dimensional

FEA. All the mechanical properties used as input in software obtained from standard testing.

In global scale, experimental results showed a linear evolution up to a certain displacement. Thereafter nonlinear behavior of the materials may be cause of more deviation from FEA. In local scale, each technique showed linear behavior but different slop. 3-D DIC measurement of strain only agreed with FBG and FEA in the lower part of the specimen (tension zone). Since 3D-DIC delivered information of surface strain while FGB can provide the core strain, two measurements can be expected to be different, this study proved it as reality.

2. Destrebecq *et. al.* (2011) [9] studied crack detection and measurement technique, to measure beam deflection and curvature of a full scale reinforced concrete beam after 25 years of service in severe industrial environment by using DIC techniques. Authors revealed existence of a compressive force in beam and compared with theoretically obtained values from Eurocode 2.

   Test specimen was 7,840 mm long, and cross sectional area was 160 x 450 mm2. The specimen had $4 - \phi$14mm longitudinal deformed rebar and ϕ6mm web reinforcement at the rate of 170 mm center to center. Rebar were not corroded. Mechanical properties of concrete found from a standard compression test of cylinder, drilled out from companion beam: compressive strength 29.8 MPa 1.7Mpa, and actual longitudinal Young modulus of elasticity 30.1 GPa 0.8 GPa. A residual deflection was about 2.6mm. In specimen, a region of interest (ROI) with 718 x 102 mm at tension zone in the middle of two loading was assigned to use DIC

technique. The ROI was divided into 10 x 10 pixels zone of interest (ZOI). They used a 2D image correlation system with 12 bits dynamic Philips camera. The CCD camera had 1024 x 1024 pixels. A SeptD developed by Vacher was used to process the captured images. Moreover, LVDT sensor was placed at mid span to measure the beam deflection. The specimen was tested in four points bending the upside down with 7000 mm effective span. Two hydraulic jacks located at a distance of 700 mm both sides of the mid-span of the beam exerted required load with 5 kN gradual increment and downgrading. Authors used 5 cycle loading, in last cycle the beam was crashed.

By processing the image taken by DIC system, displacement values were acquired by one ZOI line only. Longitudinal displacement discontinuity revealed appearance of crack, the vertical amplitude of discontinuity correlates crack opening. It also observed from the study that the cracks did not completely close upon unloading due to interlocking phenomenon. Since the cracking on concrete strain should have a strong influence on vertical displacement values, the average vertical displacement of six vertical lines located between adjacent cracks were considered as local deflection. Thereafter, a second degree polynomial fitting was used in this study to illustrate the average deflection line along the beam. Maximum deflection value found at mid span. From the theoretical calculation of crack opening, the authors observed that crack opening rate was much lower than expected in pure bending. The appearance of a longitudinal compressive force in the beam may responsible for the delay.

DIC technique is suitable for early crack detection and measurements. DIC mea-

surement has fair agreement with values measured by LVDT sensor. DIC should also be suitable for in situ damage detection.

3. Hild *et. al.* (2006) [10] proposed an approach to evaluate mode I and II stress intensity factor by combining image correlation and elastic displacement field identification.

   In case of brittle materials, crack length and crack opening measurement to quantify the stress intensity factor and toughness. Thus determining crack tip location is a major challenge. The authors used DIC to acquire the goal. In test set up, they used sandwich beam to obtain stable crack propagation. The sandwich beam was made of place silicon carbide (SiC) specimen in between two steel beams. Since the crack is complex and depending on complex geometry and surface friction, authors did not use analytical or numerical identification of the stress intensity.

   Two CCD cameras were used to take 1008 x 1016 pixels resolution picture. 6 nm physical crack was detected. Also the test results showed that the error were 2%, 3%, and 10% for 10-3, 5 x 10-4, and 2.5 x 10-4 strain.Finally, using known values of elastic properties of silicon carbide (E = 410 GPa, γ= 0.15), they calculated stress intensity factor by using crack opening displacement.

   The authors claimed that the technique can almost perfectly measure crack opening displacements in perspective of accessing scales were well below light wavelength. It reveals the way to crack identification and even quantify toughness measurement.

4. Kamaya *et. al.* (2011) [14] determined a procedure to find true stress-strain

curve. They also proposed a procedure to measure post necking strain. They used hourglass type specimens, which material was carbon steel plate for welding structures. Three specimens each of which had different notch radius, 10mm, 5mm and 2mm, along with minimum diameter of 6mm were used in tension test. Tension test were execute in ambient air at room temperature. Tension test speed was fixed as 0.2mm per minutes. Couple of 5M-pixel CCD cameras was used to determine nominal strain distribution and local displacement. The specimens were dot painted to implement digital image correlation technique.

In this study, they used general purpose program ABAQUS standard version 6.9, to conduce finite element analysis (FEA). Material properties, Young's modulus and Poisson's ratio, were provided to software. They modeled quarter of the specimen, since the specimen was geometrically symmetric. J2 flow law was bestowed to simulate stress triaxiality. Initially, σ_t was assumed to get a certain strain ϵ_t, thus P_{FEA} was found. P_{FEA} was compare with P_{exp}, and σ_t was modified till P_{FE} approached to P_{exp}. This procedure was repeated in each sampling points. Total number of sample points was 57, and number of FEA was 294. The validity of the estimated stress-strain curve can be confirmed by comparing experimental and FEA. The study result revealed that the test had been simulated successfully. From this study, it may conclude that the power low equation should provide a comprehensive approximation of the true stress-strain curve.

5. Wu *et. al.*(2011) [33] examined the properties of the fracture process zone (FPZ) in concrete using DIC. FPZ defined as the microcracking region ahead of the

traction-free crack tip in concrete. This study correlates FPZ length with load and specimen parameters.

The author investigated 6 different size and notch depth concrete specimens. The specimen manufacturing composition was 446 kg/m3 cement, 593 kg/m3 sand, and 1102 kg/m3 coarse aggregates, and water to cement ratio was 0.48. Mechanical properties of concrete were: Young's modulus of elasticity, E=35.0 GPa, compressive strength at 28 days, fc'= 42.9 MPa, and poison's ratio, μ = 0.2. A universal testing machine exerted 0.005 mm/min loading on specimens during testing. A clip gauge installed at the center of the notch to measure the crack mouth opening displacement (CMOD). A camera was placed 1.5m apart perpendicular to the test specimen to capture image at each second till the failure of the specimen, the image was processed by post-processing device. 1024 x 768 pixels resolution was adopted.

Authors concluded that DIC measurement to obtain development and length of FPZ is reasonably accurate. During crack propagation, the FPZ length increase; in contrast, FPZ length decrease after the FPZ is fully developed at a crack extension length to ligament length ratio of about 0.91. If the length of the specimen increase, the peak load and maximum FPZ length increases; on the other hand, the length decrease in case of increment of notch depth to specimen height ratio.

6. Lecompte *et. al.* (2006) [18] investigated detection of crack on prestressed concrete beam using DIC technique and LED-CCD technique. Authors used Green-Lagrange strain expression to calculate deformation. Since classical experimental

techniques, strain gauge, extensometers, etc., do not provide sufficient illustration to comprehend local damage mechanism which is responsible for structural failure, authors used full field measurement techniques focused on a given region of interest (ROI) of the target.

A 17.6 m long prestressed beam specimen. Four point bending was performed on the specimen, where the two bending points are decoupled. Four loading unloading cycle were performed where 45, 65, 76, 95 kN respectively were exerted from per jack. In DIC technique, images were taken every 10 kN loading interval. Subsequently, the displacement and deformation field at the surface of object were calculated on the basis of comparing between images at different loading steps. The image was divided into a number of subsets where the subset size was 7 x 7, 11 x 11, or 15 x 15 pixels. The software determined the displacement values of the centers of the subsets.

The study showed that crack detects appearance and evolution of cracks before the cracks become visually detectable. DIC system can be utilized to accurately locate the crack in the Zone of Interest (ZOI).

7. Bay *et. al.* (1988) [3] reported three dimensional version of two dimensional digital correlation. An X-ray topography was used to generate digital image volume. Displacements were calculated by tracking a corresponding subvolume. Gradient displacement technique was used to calculate strains from the displacement fields. In this study, a bone near the knee was investigated. This method also has significant implementation in the field of traditional engineering; for instance, a

non-destructive inspection of internal flaws and damages.

A trabecular bone with 15mm of diameter and 18mm of height was used as a specimen. The specimen was placed within a stepper-motor-controlled loading system that has an X-ray transparent polycarbonate standoff tube to mount axial loading. Area projections were collected through 3600 rotation of the sample. A cone beam algorithm was used to reconstruct the image volumes. The algorithm reconstructed a 520 x 520 voxel image volume.

A correlation between the loaded and unloaded image volumes provided a discrete displacement vector. Three contend requirements had to be mitigated in the algorithm for displacement measurement: speed, accuracy, and robust minimization. The correlation pattern matching relied on variation of voxel intensity. The correlation problem can be described simply as finding the best matches deformed shape produced from an unreformed subvolume.

The strain tensor field was calculated from the displacement vectors in two steps: (1) smoothing the displacement field by using local polynomial fit, (2) approximation of strain tensor. C code was used to develop all the algorithms.

The digital image correlation technique was upgraded to digital correlation for certain class of materials. The approximate precision reported in this study was 0.0003 ($300\mu\epsilon$).

The literature reviews in the above show that FOS can measure strain on a discrete point as well as on a discrete line. The FOS internal and external strain measurements also showed good agrement with FE models. While DIC system can measure strain

on a surface. The surface measurements showed good agreement with FE models. X-ray topography can provide internal strain measurement. However, X-ray topography techniques are not applicable for concrete structures.

2.5 Summary

In this literature review, a survey was conducted to find a suitable method to solve inverse problems. This survey contains the numerical and theoretical approaches to solve inverse problems. It was found that the numerical approach is advantageous to solve the inverse problem in this research.

Another survey was conducted on applicabilities of FE package ABAQUS® to simulate the behavior of RC structures. The survey reveals that many researchers used ABAQUS® to model RC structures under four-point bending tests. In addition, several empirical models to predict the material properties and interaction between steel rebars and concrete were investigated. The focus of the investigate was to use the empirical models to determine required parameters in ABAQUS® to model the materials and interactions.

Two techniques (FOS and DIC) to measure surface and subsurface strains were studied. The applicabilities and reliability of the techniques were the focuses on the reviews.In the next chapter (Chapter 3), applied numerical approach is introduced based on the literature reviews and additional objectives of this research.

Chapter 3

Finite Element Modelling

3.1 Introduction

In this chapter, applied numerical approach in this research is introduced. At the beginning of the chapter, a very brief overview of the FE modelling theory is discussed. The prime focuses of this chapter are discussing the strategies to create a FE model of a RC beam, define several artificial damage scenarios of the RC beam, and simulating the damage scenarios using a commercial FE package, ABAQUS®. Geometry, meshing scheme, boundary conditions, and material properties are discussed in the strategy part. In Chapter 2, a literature survey has been conducted to find required standard materials testing and suitable empirical models to predict materials properties. In this chapter, necessary empirical models are used to yield suitable input for ABAQUS® to simulate materials properties. Four artificial damage scenarios are defined and illustrated. FE modelling strategies of the damaged structures are described.

3.2 Finite Element Methods

The standard FE equation [29, 4] for a static analysis:

$$[K]\{u\} = \{f\} \tag{3.1}$$

In Eq. (3.1), [K] is the assembled global stiffness matrix, {u} is the nodal displacement vector, and {f} is the nodal force vector. The displacement vector {u} can be calculated using $\{u\} = [K]^{-1}\{f\}$.

Damage in the structure can cause change in the stiffness matrix by an amount $\Delta[K]$. Eq. (3.1) converts to the following:

$$([K] + \Delta[K])\{u^*\} = \{f\} \tag{3.2}$$

$\Delta[K]$ in Eq. (3.2) [34] can be determined by applying the following equation:

$$\Delta[K] = \sum_{i=1}^{ND} \tilde{B}_i^T \Delta k_i^* \tilde{B}_i \tag{3.3}$$

In Eq. (3.3), $\tilde{B}_i$ is Boolen matrix corresponding to ith element, ND indicates the number of damage finite elements and Δk_i^*. Expression to determine Δk_i^* is $\Delta k_i^* = \alpha_i E_i \Delta k_i$.

where, α_i = the damage fraction of the element i, E_i = the undamaged stiffness property in element i and Δk_i involves with geometric quantities or terms containing the Poisson's ratio.

3.3 Finite Element Modelling Strategies

Three-dimensional finite element analysis is conducted to determine the surface stress on a RC beam using ABAQUS®. The RC beam was made of concrete which is internally reinforced with steel rebars. A 6" x 6" x 33" deformable solid box was created to model the concrete part of a RC beam. Two 0.5" diameter and 33" long circular bars were created to model 2 – #4 rebars. The modeled rebars are embedded in the concrete elements, since ABAQUS® provides a solid-in-solid embedding option. Interaction module was used to constrain the embedded region. Absolute and frictional tolerance method was considered where fractional exterior tolerance was selected to be 0.05.

The most commonly used finite element families in a stress analysis are continuum, shell, beam, rigid, membrane, infinite, connector, and truss elements. The concrete is modeled using continuum elements (a quadratic element C3D20). Typically, in ABAQUS®, reinforcement in concrete structures is provided by means of rebars, which are one dimensional rods can be defined singly or embedded in oriented surface [7]. In this study, a continuum (solid), C3D8, element was used to model reinforcing steel rebars. Fig. 3-1 illustrates the elements used in this study.

In order to select suitable mesh size to be used, the finite element model was meshed into different numbers of elements. The meshing scheme was selected depending on the computational capacity and research objective (to observe the local stress difference due to damage(s) introduced on the embedded rebars). In process, 0.3" x 0.3" x 0.3" mesh size was selected for the concrete part. The selected rebar meshed element size

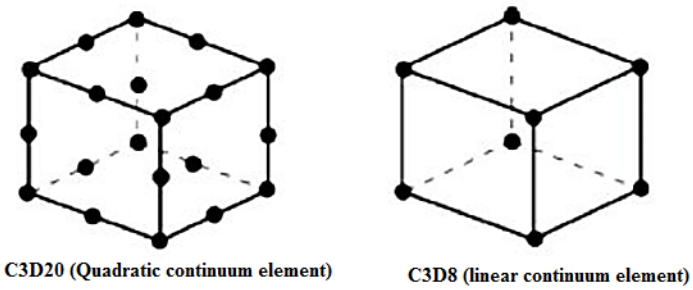

Figure 3-1: Continuum elements used in FE modeling

was 0.25” x 0.25” x 0.25”. The total number of finite elements in the model was 45,056 and the total number of nodes was 193,095. In this meshing scheme, the simulation consists of 579,285 variables. The number of variable is determined by the degree of freedom plus the maximum number of Lagrange multiplier variable. Fig. 3-2 shows the meshing scheme.

In the FE simulation the RC beam was simply supported with two point loads at one-

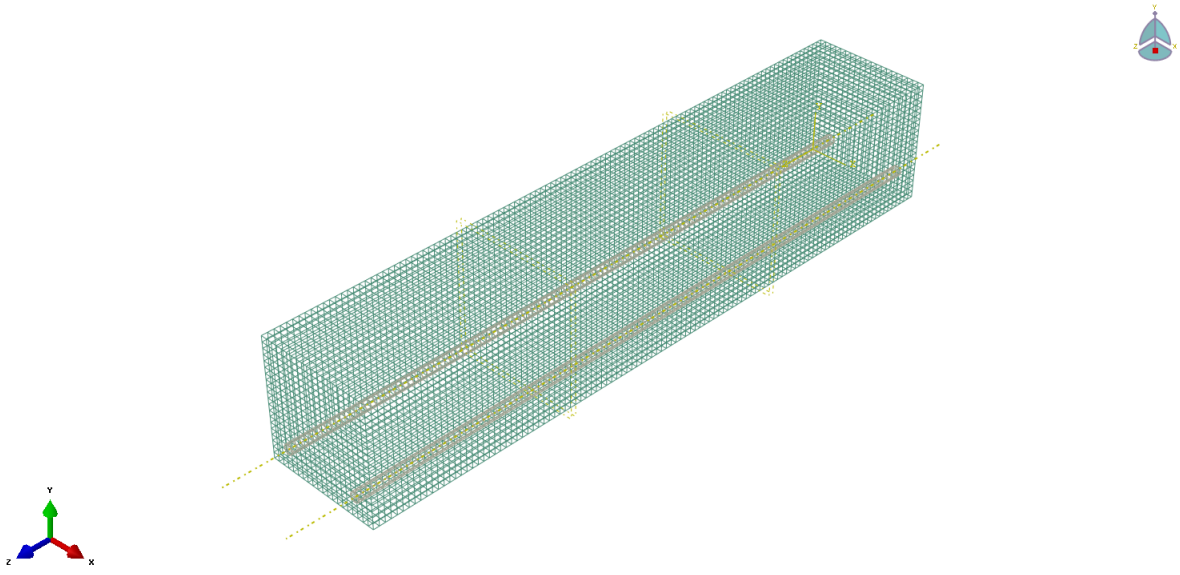

Figure 3-2: Meshing scheme of the RC beam model

third and two-third span from one end. The difference between two point loads was 12”.

The applied loads were distributed evenly on constraint area to minimize the localization effect. The size of the constraint loading area was 0.125” x 6” and the maximum load on each area was 2.2 kips. The loading procedure was divided into four steps. In the chronological order, the highest loading levels in four steps was 0.5 kip, 1.0 kip, 1.5 kips, and 2.2 kips. To simulate the loading procedure the whole time frame (1.0) was divided evenly into four steps (each time step = 0.25). Fig. 3-3 illustrates the loading scheme and boundary conditions.

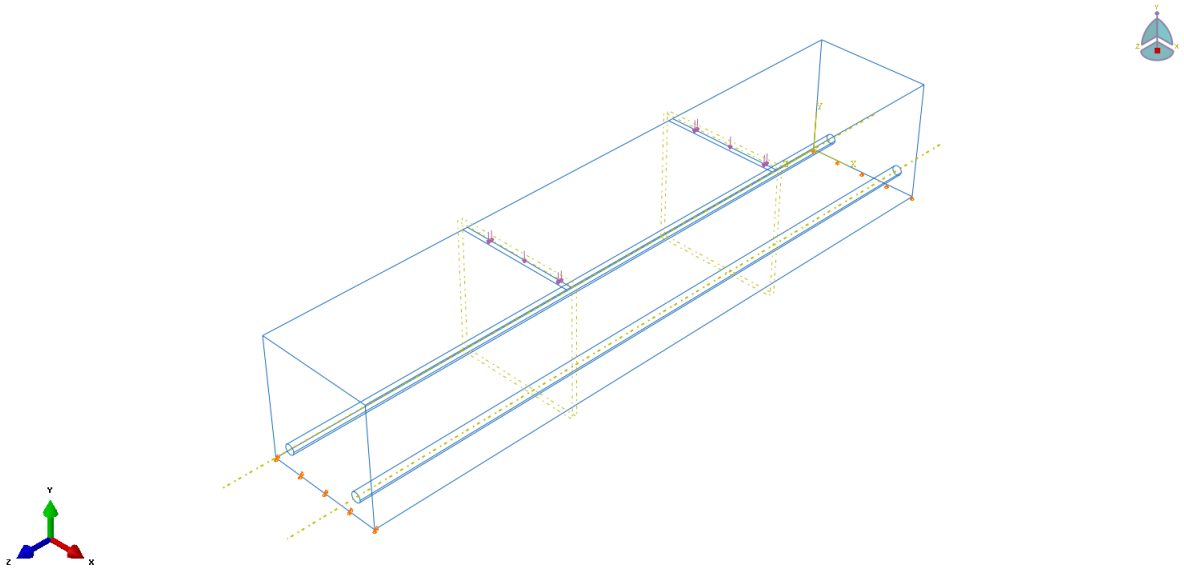

Figure 3-3: Loading scheme and boundary conditions of the RC beam model

In this study, elastic materials were used to simulate the behavior of the RC beam. The loading levels were selected to keep the strain within elastic limit of the materials. Materials’ properties were determined from standard materials tests and empirical equations (numerical formulae). The elastic parameters of concrete and steel used in the finite element simulation are:

- Young's modulus of concrete, $E_c = 4.5 \times 10^6$ psi

- Poisson's ratio of concrete, $\nu_c = 0.16$ [5]

- Young's modulus of steel, $E_s = 30 \times 10^6$ psi

- Poisson's ratio of steel, $\nu_s = 0.3$

The interaction between steel rebars and concrete was simulated using a tension stiffening model proposed by Nayal and Rasheed (2006) [27] with a minor modification proposed by Walhalathantri *et. al.* [2011] [31]. Fig 3-4 illustrates the tension stiffening model used in the FE model of the RC beam to simulate interaction between the rebar and concrete.

The Table 3.1 shows the tension stiffening input parameters used in ABAQUS®. To

Table 3.1: Tension stiffening input parameters in ABAQUS®

Stress, σ_t	Strain, $\epsilon_o t$	Elastic strain, ϵ_t^{el}	Cracking strain, ϵ_t^{ck}	Damage parameters, d_t	Plastic strain, ϵ_t^{pl}
604.669	1.48E-04	1.48E-04	0.00E+00	0.00E+00	0.00E+00
465.595	1.85E-04	1.14E-04	7.10E-05	3.84E-01	7.09E-05
272.101	5.91E-04	6.65E-05	5.25E-04	8.88E-01	5.17E-04
60.467	1.29E-03	1.48E-05	1.27E-03	9.89E-01	-7.48E+02

obtain the values tabulated in Table 3.1, Eq. (3.4), Eq. (3.6), and Eq. (3.5) were used.

$$\epsilon_t^{ck} = \epsilon_t - \epsilon_{ot}^{el} \tag{3.4}$$

$$\epsilon_t^{pl} = \epsilon_t^{ck} - \frac{d_t \sigma_t}{(1 - d_t) E_o} \tag{3.5}$$

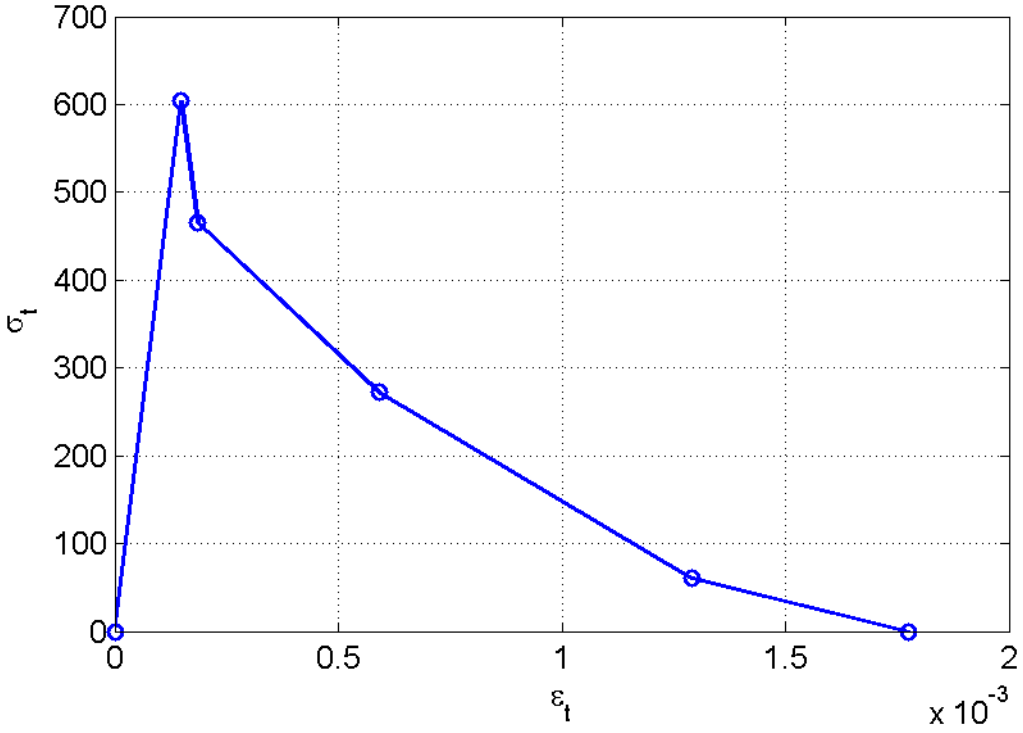

Figure 3-4: Tension stiffening model

$$d_t = \frac{\epsilon_c^{ck}}{\epsilon_t} \tag{3.6}$$

An experimentally verified Hsu and Hsu (1994) [11] numerical method was used to obtain the complete stress-strain curve for concrete under uniaxial compression.

Fig. 3-5 illustrates the predicted stress-strain curve of the concrete using Hsu and Hsu numerical method, where only σ_{cu} value was known (obtained from ASTM stand cylinder compression test, C39/C39M). Eq. (2.1) is used to obtain Fig. 3-5. The experiment is reported in Chapter 4.

The Table 3.2 shows the inelastic strain and damage parameter input parameters used in ABAQUS®. To obtain the values tabulated in Table 3.2, Eq. (2.2), Eq. (2.4),

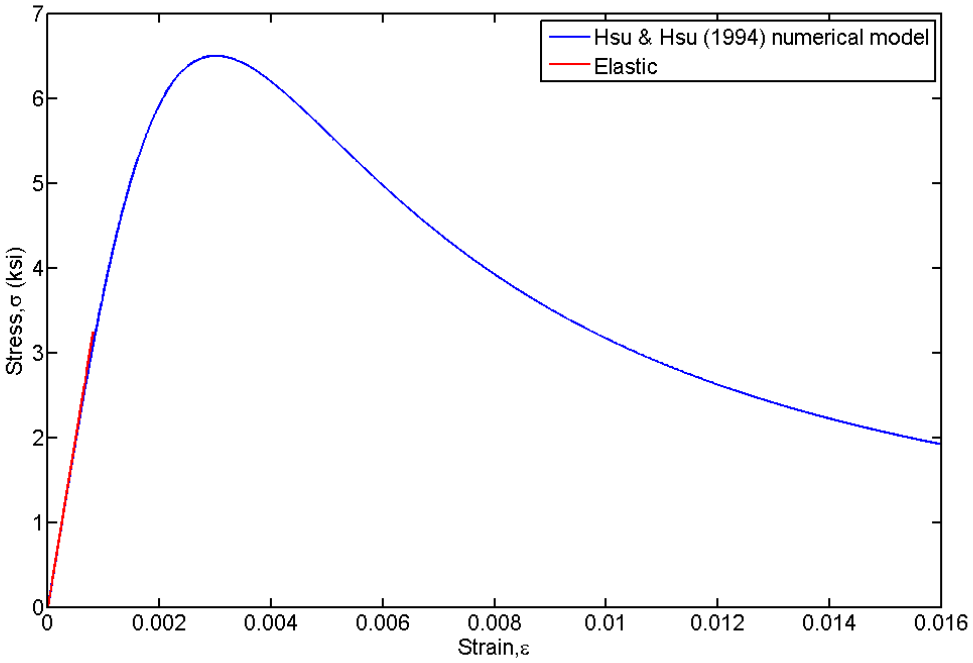

Figure 3-5: Complete stress-strain curve of concrete when σ_{cu} = 6.5 ksi

and Eq. (2.3) were used.

The numerical model of the complete stress-strain curve of concrete is compared with response of a 6" x 6" concrete cube FE model under uniaxial loading. In this loading scheme the loading range was from 0 psi to 6,500 psi. Fig. 3-6 shows the comparison.

The materials property of steel was modelled as a perfectly elastic-plastic material. The yielding stress (σ_y) of steel was determined by a standard tension test. The test result is reported in Chapter 4.

Table 3.2: Inelastic strain and damage parameter in ABAQUS®

Stress, σ_c	Damage parameters, d_t	Inelastic strain, ϵ_c^{el}
3.25E+03	0.00E+00	0.00E+00
3.56E+03	8.69E-03	6.20E-05
3.72E+03	1.01E-02	7.24E-05
3.88E+03	1.17E-02	8.38E-05
4.03E+03	1.35E-02	9.64E-05
4.17E+03	1.54E-02	1.10E-04
4.31E+03	1.74E-02	1.25E-04
4.45E+03	1.96E-02	1.41E-04
4.58E+03	2.20E-02	1.58E-04
4.71E+03	2.45E-02	1.76E-04
4.83E+03	2.72E-02	1.95E-04
4.95E+03	3.01E-02	2.16E-04
5.06E+03	3.31E-02	2.38E-04
5.17E+03	3.63E-02	2.61E-04
5.27E+03	3.96E-02	2.85E-04
5.37E+03	4.31E-02	3.11E-04
5.47E+03	4.68E-02	3.37E-04
5.55E+03	5.06E-02	3.65E-04
5.64E+03	5.46E-02	3.94E-04
5.72E+03	5.87E-02	4.24E-04
5.79E+03	6.30E-02	4.55E-04
5.87E+03	6.75E-02	4.88E-04
5.93E+03	7.20E-02	5.21E-04
5.99E+03	7.67E-02	5.56E-04
6.05E+03	8.16E-02	5.91E-04
6.11E+03	8.66E-02	6.28E-04
6.16E+03	9.17E-02	6.65E-04
6.20E+03	9.70E-02	7.04E-04

3.4 Artificial Damage Scenarios

Artificial damages on steel rebars were introduced by making two concave parabolic longitudinal boundaries in the damage length. The cross sectional reduction (ΔA_s) is calculated in percentile.

$$\Delta A_s = \frac{A_{so} - A_{sr}}{A_{so}} \times 100(\%) \tag{3.7}$$

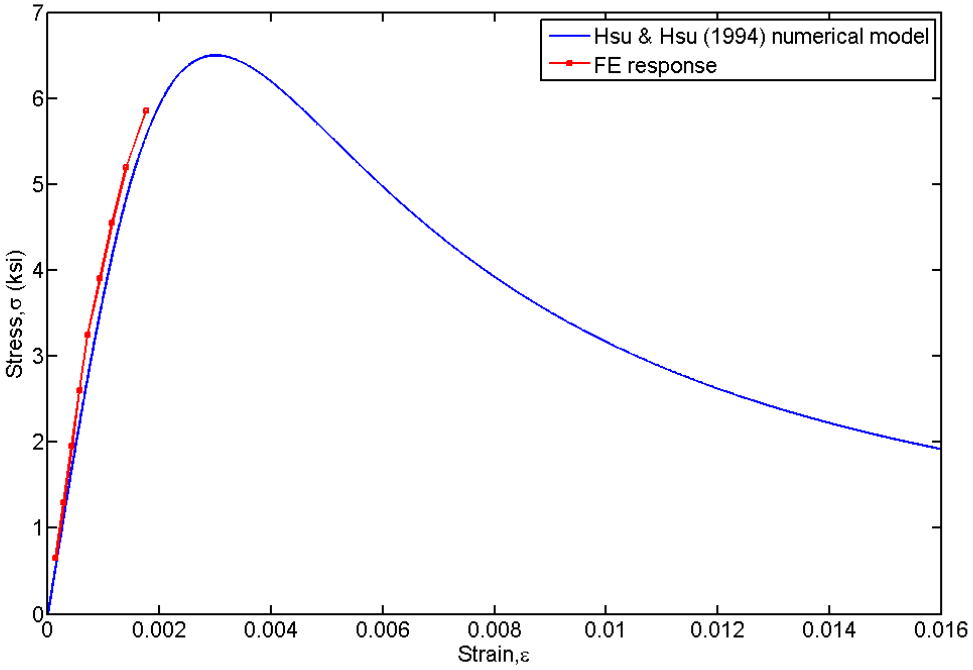

Figure 3-6: Stress-strain response from FE model vs. material model provided in simulation

The cross sectional reduction at the center of the damage used in this study were 10%, 15%, 20%, 25%, 30%, and 36%. Two damage lengths were considered: a) 1 inch and b) 5 inches. The intact diameter of the steel rebar as shown in Fig. 3-7 is 0.5 inch ($A_{so} = 0.196\ in^2$) and rebar diameter at the center of the damage is 0.4 inch ($A_{sr} = 0.125$). Using Eq. 3.7, calculated ΔA_s is 36%.

Due to the reduction of cross sectional area, the rebars wane volume. Fig. 3-8 illustrates a slice of lost volume. The slice creates 60^o angles at the center of the steel rebar. The relative volume changes are tabulated in table 3.4. ΔV_s in table 3.4 is calculated according to Eq. 3.8.

$$\Delta V_s = \frac{V_{so} - V_{sr}}{V_{so}} \times 100(\%) \tag{3.8}$$

Table 3.3: Imperial models for FE simulations

Model	Purpose	Year
Hsu and Hsu [11]	To obtain a complete stress strain curve of concrete	1994
Nayal and Rasheed [27] model modified by Walhalathantri et. al.[31]	To simulate interaction between rebars and concrete	2006 &2011(Modified)
Perfect elastic-plastic material property	To simulate the stress-strain behavior of steel	-

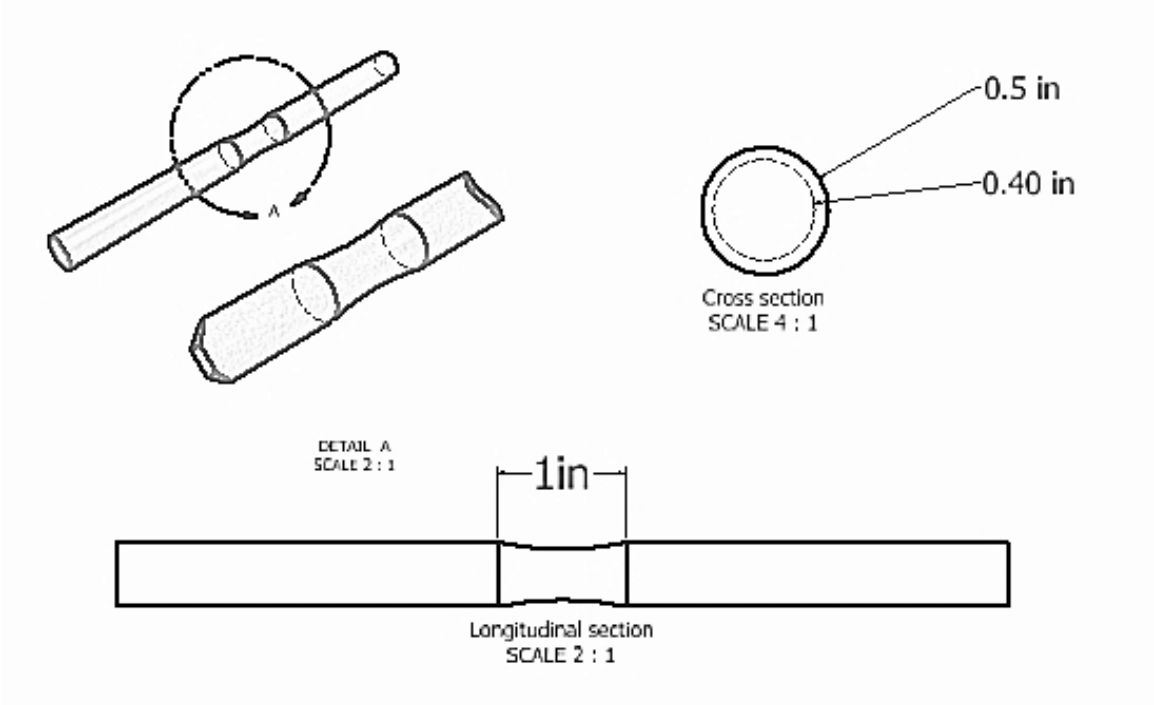

Figure 3-7: Schematic of a 1-in long artificial damage

In this study, four types of damages were introduced in the FE model of RC beam. The definition and illustration are shown in the following:

1. Type I: Cross sectional reduction of area, ΔA_s of the rebars at the mid-span and the center of the damage are 36%, 30%, 25%, 20%, 15%, and 10%. The damage length is 1 inch. Type I is classified into two categories: a) symmetric damage (Type I-I) and b)nonsymmetric damage (Type I-II). In Type I-I damage, an ar-

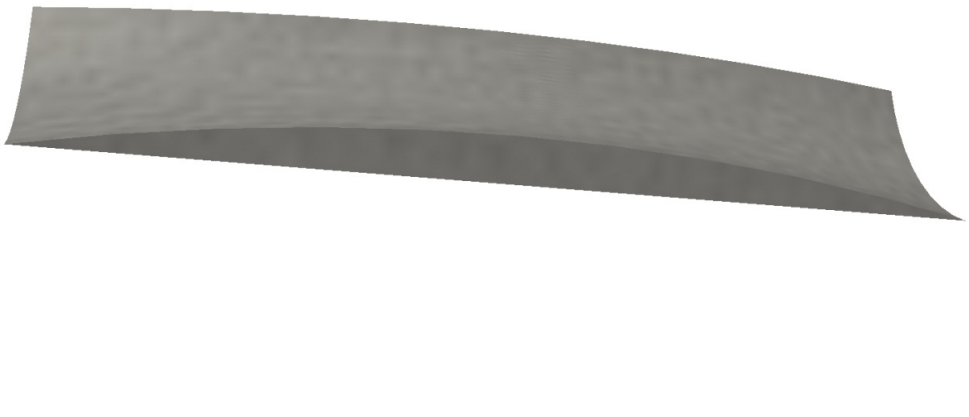

Figure 3-8: A slice of lost volume of the rebar

Table 3.4: Cross sectional reduction vs. volume reduction of the rebars

ΔA_s(%)	$V_{so} - V_{sr}(in^3)$	ΔV_s (1-in damage)	ΔV_s (5-in damage)
10	0.013	6.633	5.736
15	0.020	10.204	8.768
20	0.026	13.265	11.402
25	0.033	16.837	14.419
30	0.040	20.408	17.836
36	0.048	24.48	21.635

tificial damage is introduced to both rebars while in Type II only one rebar has the damage. Fig. 3-9 and Fig. 3-10 illustrate Type I-I and Type I-II damage, respectively.

2. Type II: Cross sectional reduction of area, ΔA_s of the rebars at 8.5 inches from the right support and the center of the damage are 36%, 30%, 25%, 20%, 15%, and 10%. Damage length is 1 inch. Type II is classified into two categories: a) symmetric damage (Type II-I) and b)nonsymmetric damage (Type II-II). In Type II-I damage, an artificial damage is introduced to both rebars while in Type II-II

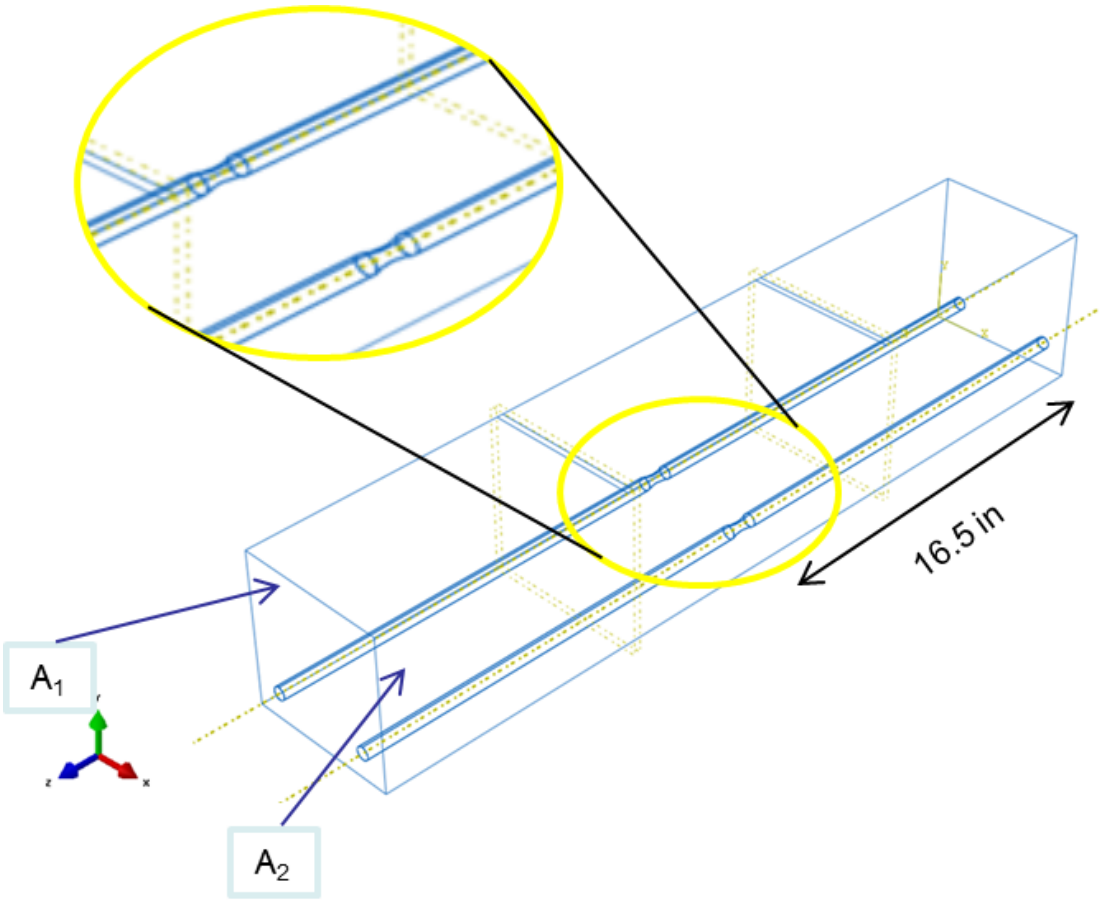

Figure 3-9: Artificial damage Type I-I

one of the rebars has the damage. Fig. 3-11, and Fig. 3-12 illustrate Type II-I and Type II-II damage, respectively.

3. Type III: Cross sectional reduction of area, ΔA_s of the rebars, one at 8.5 inches from the right support and another one 8.5 inch from left support and the center of the damages are 36%, 30%, 25%, 20%, 15%, and 10%. The damage length is 1 inch. Fig. 3-13 illustrates the Type III damage.

4. Type IV: Cross sectional reduction of area, ΔA_s of the rebar at the mid-span and the center of the damages are 36%, 30%, 25%, 20%, 15%, and 10%. The damage length is 5 inches. Type IV is classified into two categories: a) symmetric damage

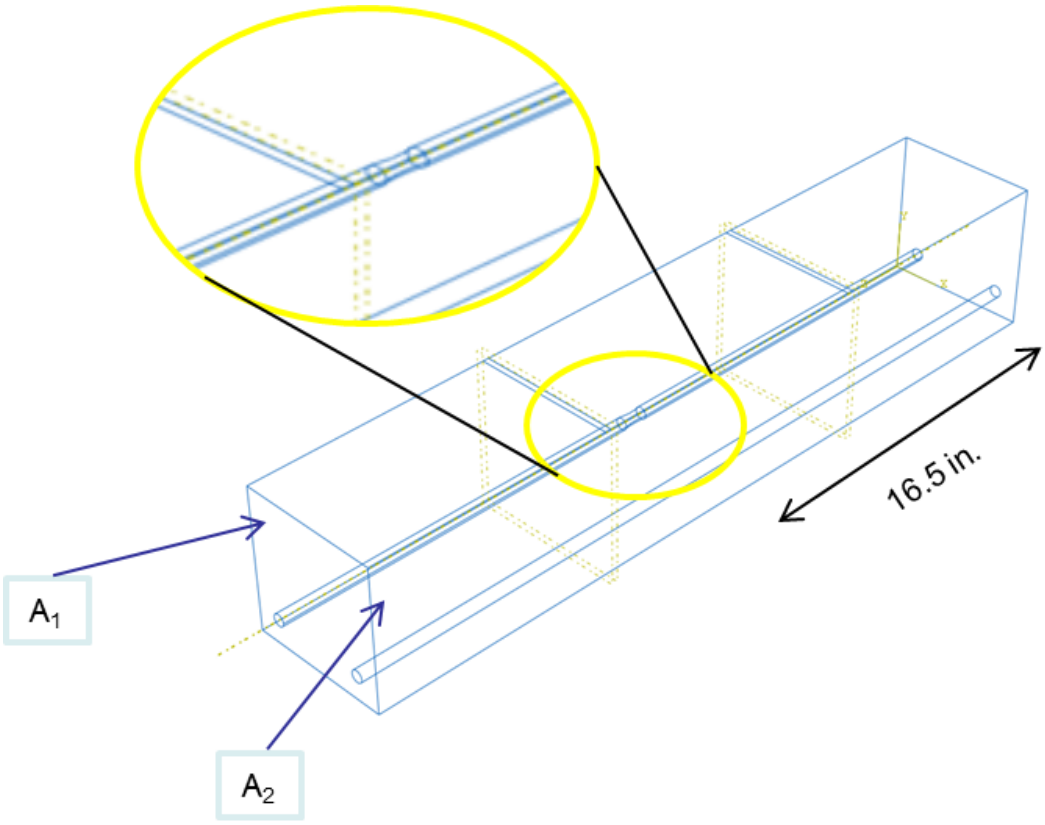

Figure 3-10: Artificial damage Type I-II

(Type IV-I) and b)nonsymmetric damage (Type IV-II). In type IV-I damge, an artificial damage is introduced to both rebars while in type IV-II only one rebar has the damage. Fig. 3-14 and Fig. 3-15 illustrate Type IV-I and Type IV-II damage, respectively.

From Fig. 3-9 to Fig. 3-15 define beam sides as $A1$ and A_2. The side definition will be used in Chapter 5 to illustrates the FE results.

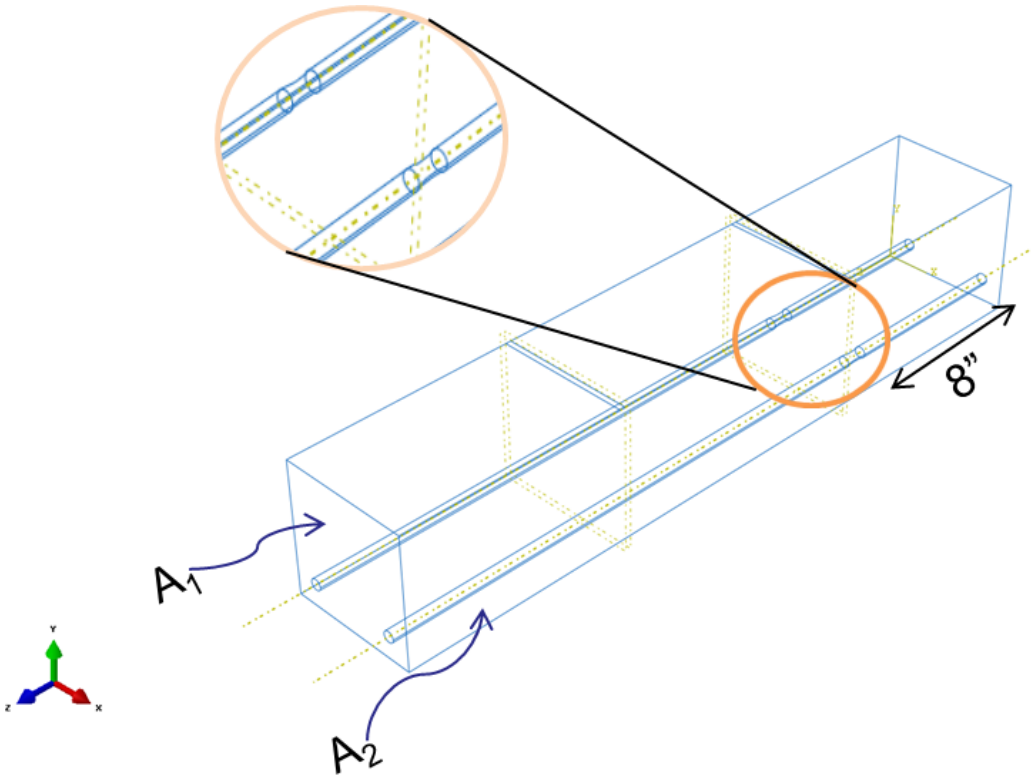

Figure 3-11: Artificial damage Type II-I

3.5 Finite Element Modelling of Artificial Damages

The damages in rebar were simulated in the FE model of the RC beam according to the geometric change in the rebar(s). The meshing scheme of rebars and concrete were kept identical to the intact model. The interaction between rebars and concrete was also kept identical to the intact model.

3.6 Summary

FE modelling strategies of a RC beam were discussed. Several empirical models of material properties were used to determine materials parameters required in the FE

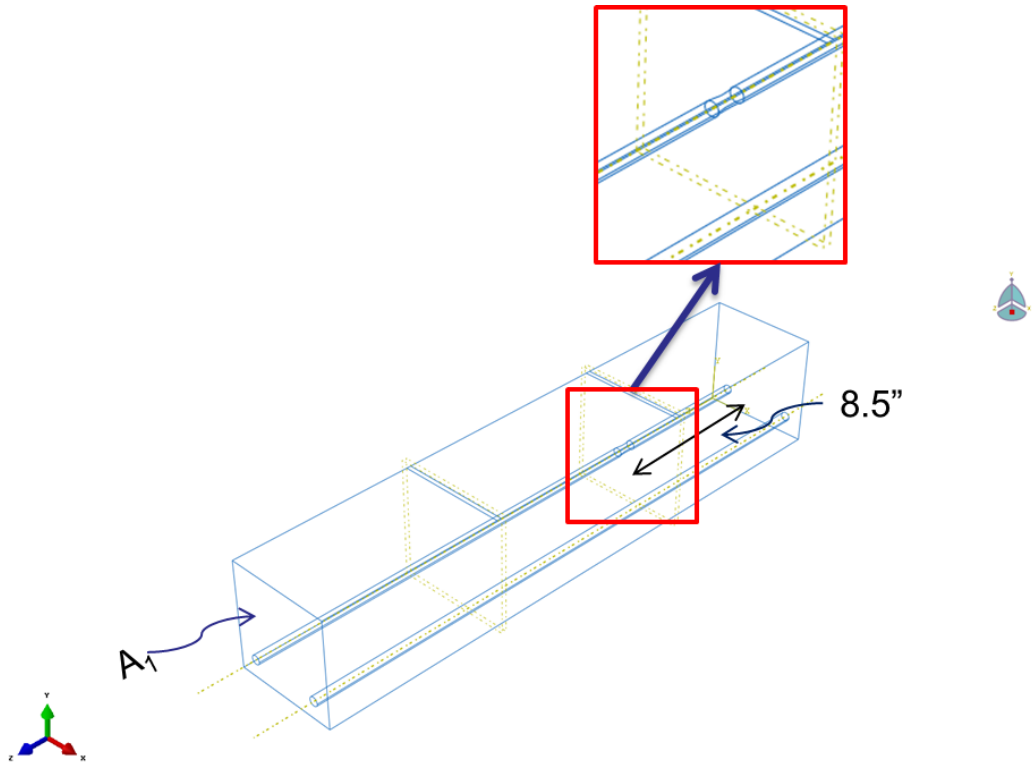

Figure 3-12: Artificial damge Type II-II

Table 3.5: A sketch of artificial damages

Type	Damage length	Location	Subcatagories
I	1 in	Midspan	Symmetric & Non-symmetric
II	1 in	8.5 in from right support	Symmetric & Non-symmetric
III	1 in	one rebar 8.5 in from right and another rebar 8.5 in from left support	No
IV	5 in	Midspan	Symmetric & Non-symmetric

simulate of the RC beam using ABAQUS®. Use of a suitable model to simulate the interaction between concrete and rebars was illustrated. Four damage scenarios of the RC beam were defined along with the FE modelling strategies. To validate the FE model a series of Four-point bending tests on the RC beam were conducted. The details of the four-point bending test is illustrated in the next chapter. Chapter 4 also contains the description of the standard material tests.

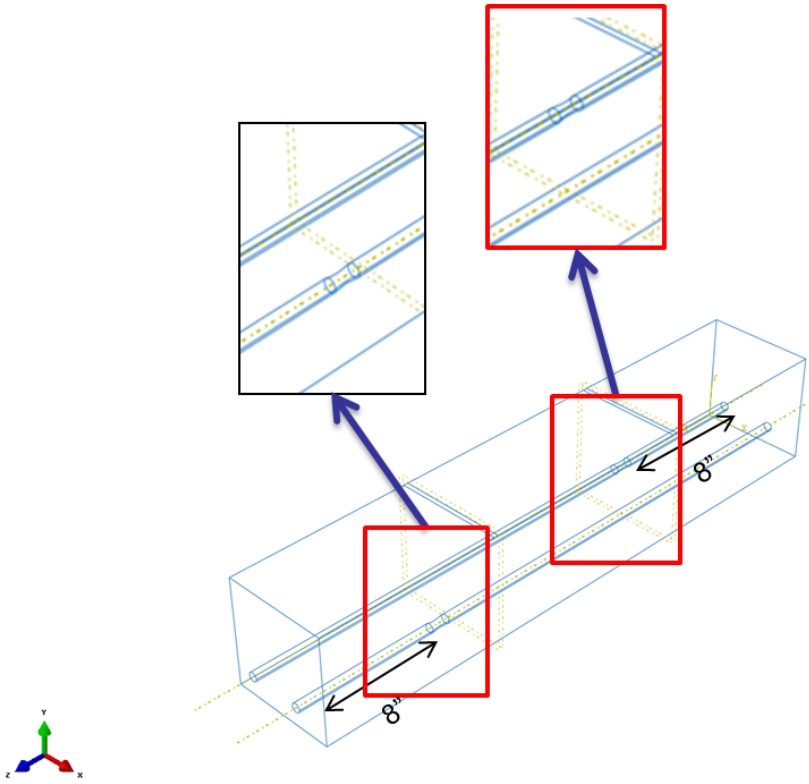

Figure 3-13: Artificial damage Type III

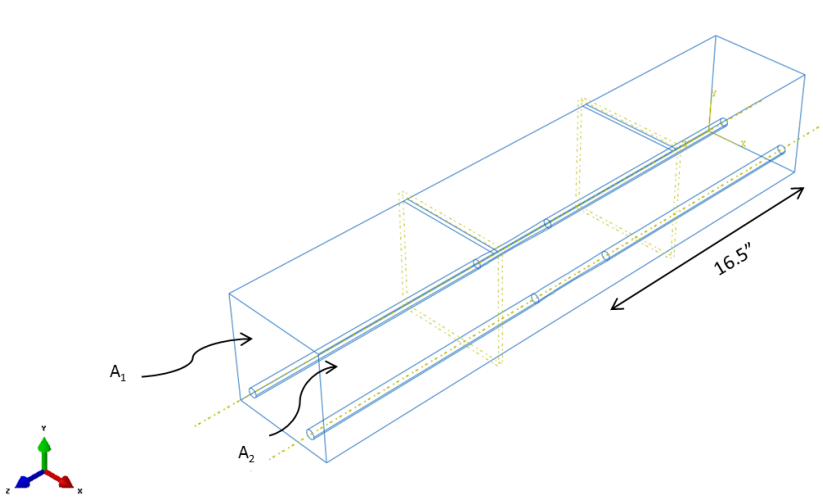

Figure 3-14: Artificial damage Type IV-I

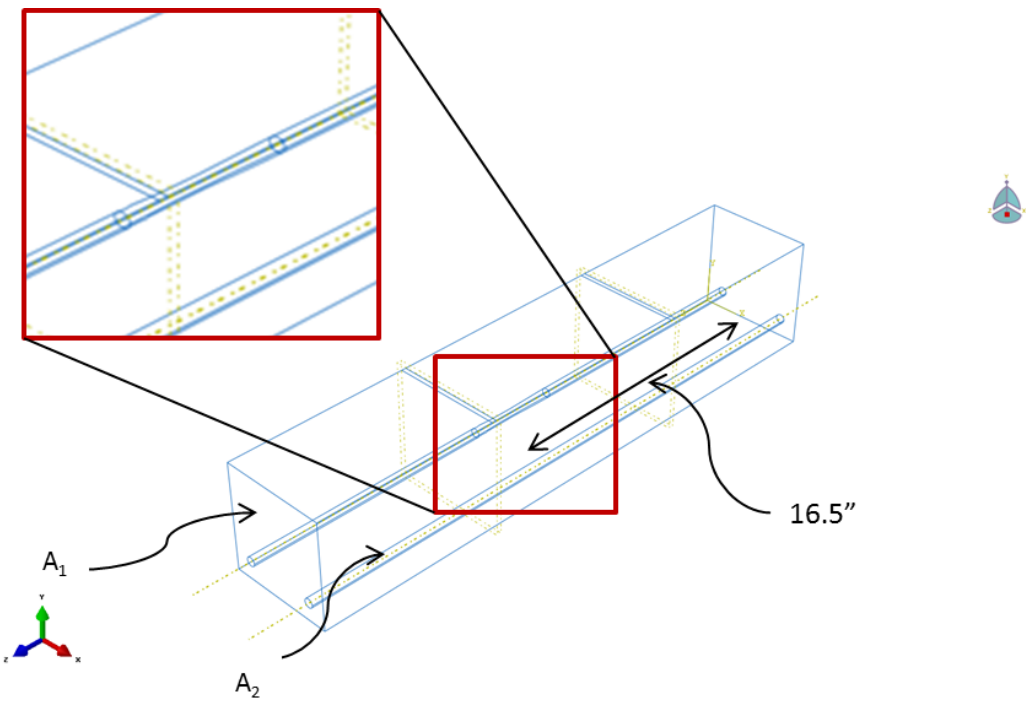

Figure 3-15: Artificial damage Type IV-II

Chapter 4

Experimental Work

4.1 Introduction

In this chapter, the specifications and manufacturing procedure of a test specimen (the RC beam), materials testing, and a details of a four-point bending test are described. The materials testing results are processed to yield required parameters for the FE package, ABAQUS® to simulate the behavior of the cast RC beam. The materials testing results are also used to determine the theoretical capacity (e.g., nominal moment capacity, cracking moment capacity) of the RC beam. The cracking moment of the RC beam is calculated to determine the maximum loading level in the four-point bending test. Experimental setup of the four-point bending test is illustrated and surface strain measurements from the collected raw data are briefly discussed. The FE model developed in the Chapter 3 will be validated using the four-point bending test results in the Chapter 5.

4.2 RC Beam Specimen

In this experiment, the RC beam specimen size was 6” x 6” x 35”. Mix proportion was 1:1.5:3 (Cement: Fine Aggregate: Coarse Aggregate) and water/cement ratio was 0.50. Two #4 steel rebars were used. Fig. 4-1 illustrates the dimensions of the RC beam.

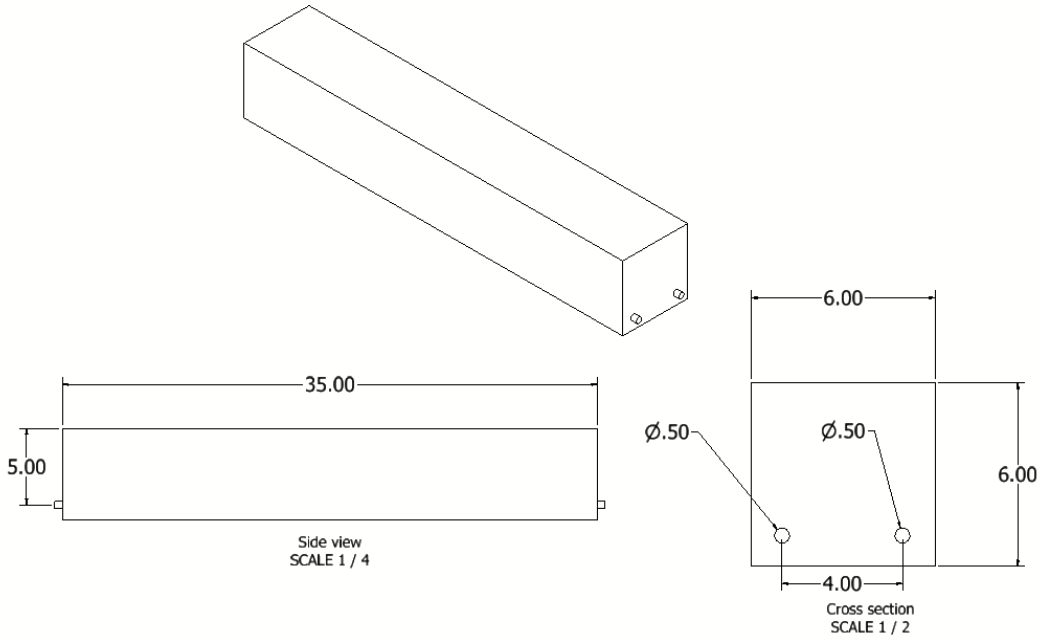

Figure 4-1: Dimensions of the RC beam specimen

4.2.1 Materials Testings

Two 4” x 8” cylinders were cast to determine the compressive strength of concrete (f_c'). Measurements of f_c' and the tensile strength of steel (f_y) were important to determine the loading levels of the experiment without introducing cracks to the RC beam on the tension side. The materials testing results are also processed to yield required parameters for the FE package, ABAQUS® to simulate the behavior of the cast RC beam.

Tension Test of the Steel Rebar

Specimen specifications:

- Length =14 inches

- Size = #4 steel rebar (Cross-sectional area, A_s= 0.2 in^2, and diameter, ϕ=0.5 in)

A FOS was used to find a true stress-strain diagram of the steel rebars using in the RC beams. A FOS, os3110-1552-1UT-1UT manufactured by Micron Optics, Inc., was attached with rebar as shown in the Fig. 4-2. The rebar surface was grinded to make a smooth surface to attach the FOS. Regular epoxy (Welder Contact Adhesive) was used to attach the sensor onto the rebar. The Rebar was mounted, attachment points distance was 7.5 inch, on Instron 1332 fatigue testing machine (maximum capacity approximately 22.5 kips) to conduct a conventional tension test. The maximum load was selected to be 15 kips. The maximum load was selected such a way that it should exit the yielding point but should not exit the fracture load. The test was load controlled;loading rate was 2000 lbs per minutes (prefixed).

Fig. 4-3 illustrates the time vs. loading. A double check of loading rate was made from the slope of the straight line = $\frac{(10359.54 - 8430.26)}{(307.98 - 250.38)}$ = 33.49 lb/sec = 2009.66 lb/min.

Fig. 4-4 represents the load vs. the total elongation of the re-bar. An approximation of stress-strain can be made considering that cross sectional area of the rebar was 0.2

Figure 4-2: FOS attached with rebar

in^2 and length to be elongated was 7.5 inch. However, this approximation should be erroneous, since the true length to be elongated is a unknown quantity, also the cross sectional area was selected from a standard chart. Moreover, the machine has machine compliances. Therefore, FOS should provide the true strain.

FOS sensor provided a time domain strain measurements. The time domain curve can be easily converted to the load domain curve and eventually can be converted to stress domain. Conversion equation is $P(t) = s \times t$ where s is load increment rate, found from figure 2 (33.49 lb/sec) and stress = P/A_s. Fig. 4-5 represents the time domain strain measurement. Above mentioned conversions were made to determine the stress-strain graph of the rebar; Fig. 4-6 represents the strain-stress graph of the rebar.

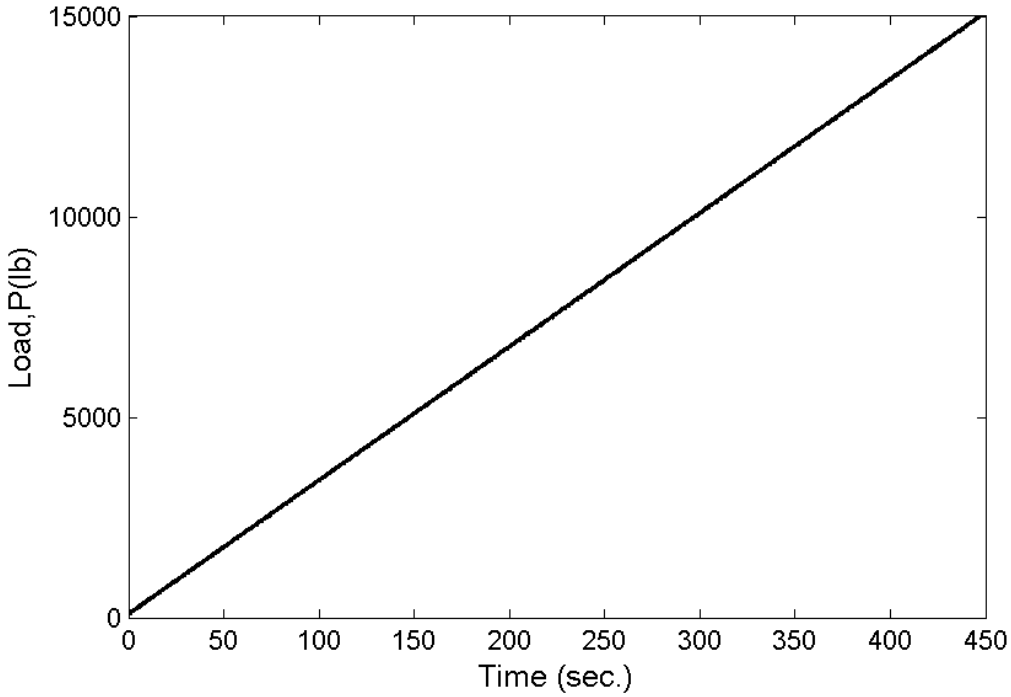

Figure 4-3: Loading rate of Instron 1332 fatigue testing machine

Compressive Test of Concrete

Two 4” x 8” cylinders were tested to determine compressive strength of concrete according to ASTM C39/C39M. 6488 psi and 6608 psi compressive strength were found with an average of 6548 psi. The values satisfied the ASTM C39 [2] precision statement. Thus, 6500 psi was used as a compressive strength of concrete to calculate cracking moment of the RC beam specimen.

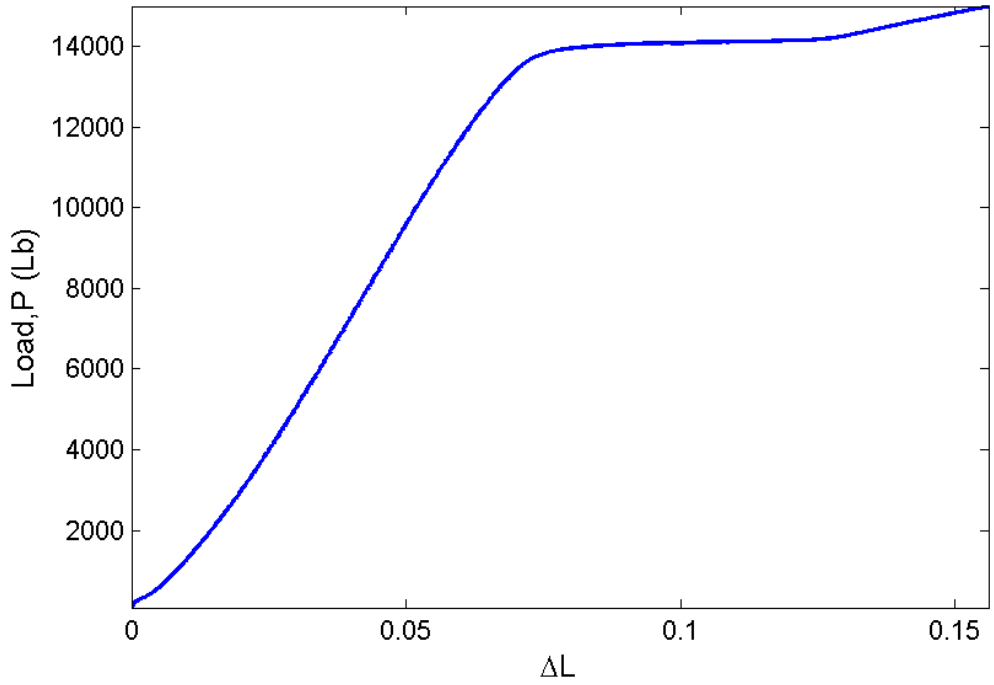

Figure 4-4: Load Vs. elongation

4.2.2 Theoretical Calculation of the RC Beam Capacity

From Euler-Bernoulli beam theory,

$$M_{int} = EI\varphi \tag{4.1}$$

where, E = elastic modulus, I = moment of inertia, and φ = curvature

From the Fig.4-7, $\varphi = \frac{\epsilon_t + \epsilon_c}{h} = \frac{\epsilon^*}{y}$. By replacing φ in Eq. (4.1),

$$M_{int} = EI\frac{\epsilon^*}{y} \tag{4.2}$$

$$\therefore \epsilon^* = \frac{M_{int}y}{EI} \tag{4.3}$$

Effective flexural rigidity, EI in Eq. (4.3) can be computed using layer by layer

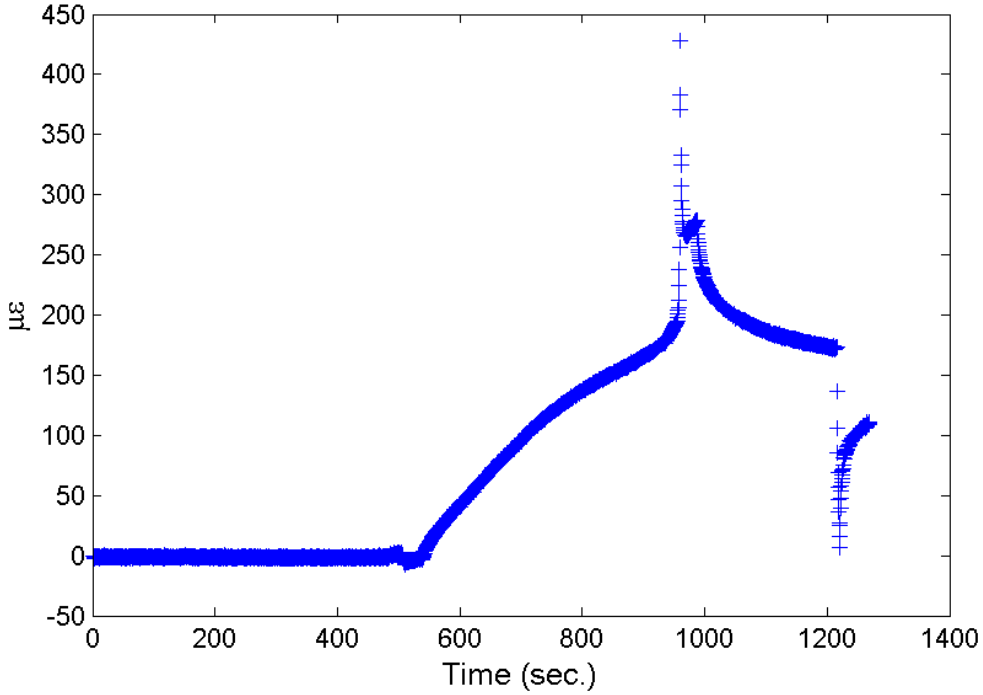

Figure 4-5: FOS sensor response

integration (Eq. 4.4). A layer distribution is shown in Fig. 4-8.

$$EI = \Sigma_{i=1}^{NL} E_i I_i \tag{4.4}$$

Here, NL is number of layer considered. For uncracked section an equivalent area approach can be used.

$$EI = E_c\{\frac{bh^3}{12} + bhe_1^3 + (n-1)A_s e_2^3\} \tag{4.5}$$

By modifying Eq. (4.3), cracking moment (M_{cr}) of the RC beam specimen is calculated using Eq. (4.6)

$$M_{cr} = \frac{\sigma_r I_g}{y_t} \tag{4.6}$$

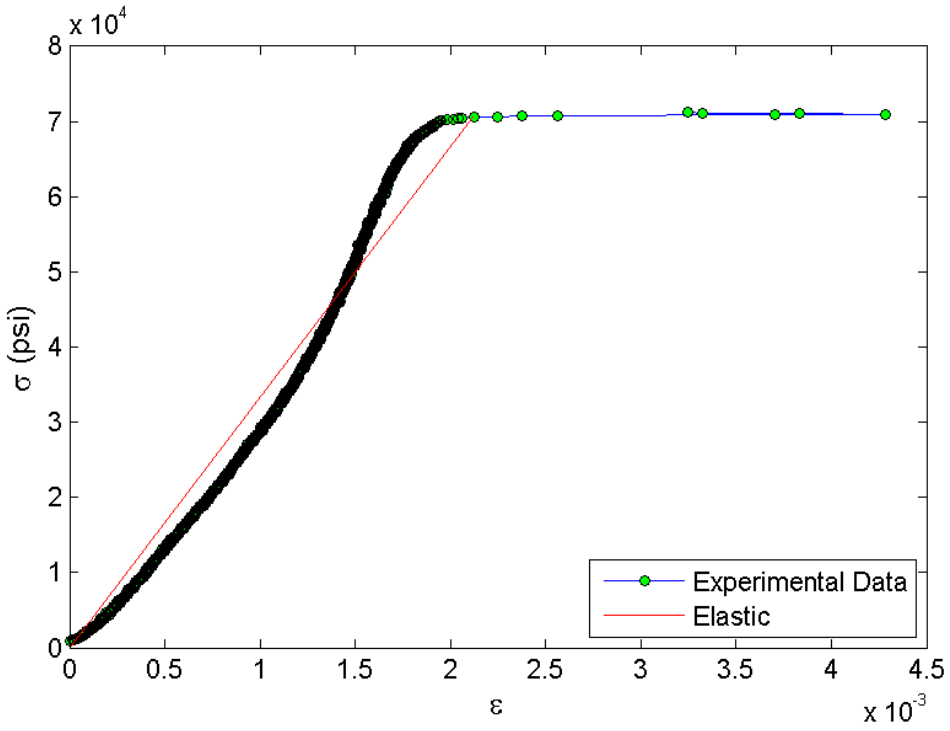

Figure 4-6: Stress-strain graph of the specimen rebar

where,

$\sigma_r = 7.5\sqrt{f'_c} = 604.66$ psi

$E_c = 57000\sqrt{f'_c} = 4.59 \times 10^6$ psi

$E_s = 30 \times 10^6$ psi

$$n = \frac{E_s}{E_c} = \frac{30}{4.59} = 6.53$$

$$y = \frac{(bh^2/2)(n-1)(A_s d)}{bh + (n-1)A_s}$$

$$I_g = \frac{bh^3}{12} + A_1(\frac{h}{2})^2 + (n-1)A_s(d-y)^2 = 108 + 0.36 + 7.28 = 115.64\ in^4$$

$\therefore M_{cr} = 24.11$ k-in

If the loading point, where applied load is P, and support distance is considered 10.5 inches in four point bending test configuration, bending moment at midsection of the RC beam specimen is $10.5 \times P$. If $10.5 \times P = 24.11$ which yields P = 2.29 kips at each

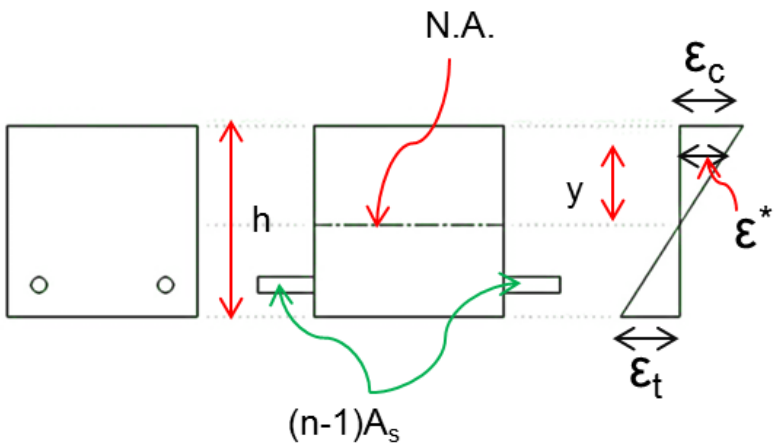

Figure 4-7: Strain variation through-thickness

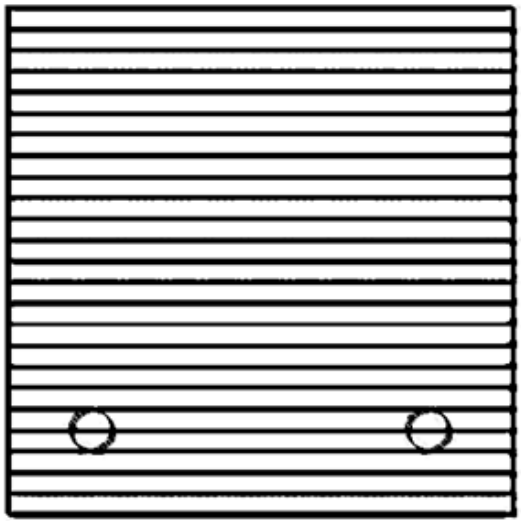

Figure 4-8: Layers to find effective rigidity

point, no crack should be induced. Select $P = 2.2$ kips, therefore $M = 10.5 \times 2.2 = 23.1$ k-in.

$$M = C\eta h_o = \omega\sigma_c\xi b\eta h_o \therefore \sigma_c = \frac{M}{\omega b\eta\xi h_o^2} \tag{4.7}$$

$$M = T\eta h_o = \sigma_s A_s \eta h_o \therefore \sigma_s = \frac{M}{A_s \eta h_o} \tag{4.8}$$

$$\bar{\varphi} = \frac{\bar{\epsilon_c} + \bar{\epsilon_s}}{h_o} = \frac{\frac{\sigma_{c,x}}{\beta E_c} + \frac{\sigma_{s,x}}{E_s}}{h_o} = \frac{\frac{M}{\omega b \eta \xi h_o^2} + \frac{M}{A_s \eta h_o}}{h_o} = \frac{1}{h_o}\{\frac{M}{\omega b \eta \xi h_o^2 \beta E_c} + \frac{M}{A_s \eta h_o E_s}\} \quad (4.9)$$

$$\therefore \bar{\varphi} = \frac{M}{h_o}\{\frac{1}{\chi b h_o^2 E_c} + \frac{1}{A_s \eta h_o E_s}\} \quad (4.10)$$

$$\bar{\varphi} = \frac{M}{EI} \therefore EI = \frac{M}{\bar{\varphi}} = \frac{1}{\frac{1}{h_o}\{\frac{1}{\chi b h_o^2 E_c} + \frac{1}{A_s \eta h_o E_s}\}} \quad (4.11)$$

where,

h_o=distance between rebars center and the outmost compression fiber of the section or effective depth of the section

ω = Normalization factor of σ_c. In elastic case ω is 0.5

ξ =Coefficient of h_o to find compression zone.

η= Coefficient to find moment arm

ϵ_S = Strain in steel at tension zone

ϵ_c = Strain in concrete at compression

β = Variable reduction factor

E_c = Elastic modulus of concrete

E_s = Elastic modulus of steel

χ = Average strain coefficient of compression concrete.

4.2.3 Procedure to Cast a RC Beam Specimen

The RC beam specimen was cast. Specimen size was 6” X 6” X 35” reinforced by 2-#4 steel rebar at 1” concrete cover from the bottom. Mixture proportion (volumetric) used for the casting was 1:1.5:3 (Cement: Fine aggregate: Coarse Aggregate), and 0.5 water to cement weight ratio was used. Ordinary Portland cement, surface dried sand and surface dried crushed stones were used for the cement, fine aggregates, and coarse aggregate, respectively. As ingredients, 0.205 cft cement, 0.307 cft sand, 0.614 cft crushed stones, and 9.00 pounds of water were used to cast the test specimen.

Firstly, crashed stones were washed by drinkable water, thereafter it was air dried for around 3 hours. Finally, the coarse aggregates (CA) were toweled to ensure surface dryness.

A mixture machine was used to perform the mixing process. Approximately 10 rotations of the dry mixture were performed to ensure the proper dry mixing before adding water. To ensure a good mixing and to avoid segregation, sufficient amount of rotation were considered for wet mixing. During placing the concrete, sufficient rodding was conducted. After placing the concrete, the curing process was started after approximate 14 hours.

Figure 4-9: Casting of the RC beam

4.3 Mechanical Testing of the RC Beam Specimen

Equipments and equipments' specifications are described below which were used in the mechanical four-point testings of the RC beam.

1. Load cell: Load cell, Lebow 3175 manufactured by Inter Technology, Inc., used in the mechanical testing. The capacity of the load cell is 50,000 lb. Creep is (in 20 minutes of rated output) 0.025%. Usable temperature range of the equipment is -50 C to +93 C while temperature effect on output is 0.002%. Fig. 4-10 shows the model used in the mechanical test.

2. FOS: A FOS model, os3110 manufactured by Micron Optics, Inc., was used to determine the surface strain of the RC beam. The specification of the FOS are tabulated in the Table 4.1.

   Mechanically induced strains are calculated using Eq. (4.12). In Eq. (4.12) ϵ_{TO} is found from Eq. (4.13).

Figure 4-10: Load cell, Lebow 3175

Table 4.1: Specification of FOS, os3110

Variable	Description	Value	Units
FG	Gage Factor	0.89 @ 22^{o}C	-
C1	Gage Constant 1	6.156 @ 22^{o}C	$\mu m/m -^o C$
C2	Gage Constant 2	0.70	$\mu m/m -^o C$
ΔT	Temperature Change	Measured	^oC
CTEs	CTE of Test Specimen	User defined	$\mu m/m -^o C$
$\Delta\lambda$	Wavelength Shift	Interrogated	nm
λ_o	Nominal Wavelength	Initial Value	nm

$$\epsilon = \frac{\Delta\lambda}{FG\lambda_o} \times 10^6 - \epsilon_{TO} \tag{4.12}$$

$$\epsilon_{TO} = \Delta T[\frac{C1}{FG} + CTEs - C2] \tag{4.13}$$

3. DIC: Two dimensional DIC is an optical measurement technique that uses pattern recognition algorithms to track features in a series of digital images. To perform DIC, DIC software partitions the image into overlapping square groups of pixels called facets or subsets. Tracking these facets is the foundation of DIC. The DIC software identifies the pattern of each facet based on the light intensity values of the pixels in the facet. The software searches successive images in the series for pixel groups that match the light intensity values of the facet in the original

image. The geometric center of each facet can be interpolated and tracked though out the image series permitting the calculation of strain and displacement fields. Typically a high contrast stochastic pattern is applied to the surface to form more distinct patterns and therefore increase the accuracy of the pattern recognition process.Camera resolution of the system is 4096×3072. GOM^{TM} is used as 3D DIC data processing software.

A FOS sensor was installed at the side of the RC beam in compression zone, distance from the top most fiber of the concrete and middle of the FOS was 0.5 inch, to measure the surface stain. The sensor was calibrated by Micron Optics, Inc., the calibration data was attached. To measure the surface strains of the side of the RC beam using DIC technique, proper dots were painted on the test specimen.The DIC system was calibrated to take the measurements accurately.

RC beam specimen was placed on the load frame and point loads were placed as illustrated in Fig. 4-11. Support condition was simply supported. Fig. 4-12 illustrates a layout of the four point bending test.

In the four loading cycles, the maximum load mounting was limited to 2.2 kips (each loading point). The mounting increment rate was 0.5 kips (each loading point), and unloading rate was a similar decrement rate. Fig. 4-13 illustrates an exemplary loading cycles of the four-point bending tests.

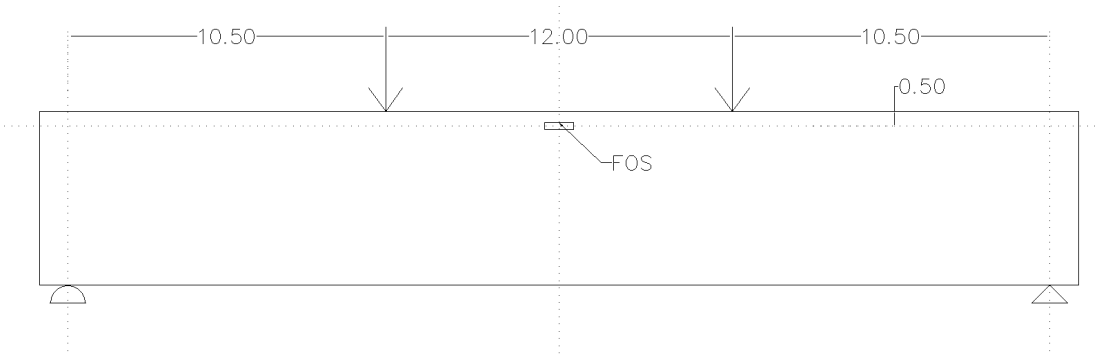

Figure 4-11: RC beam specimen setup for four points bending

The FOS took strain measurements at each 0.5 second while the DIC was measuring the surface strain at each 5 seconds throughout the test. The FOS was taking measurement at a discrete location where it was attached. In contrast, the DIC system took measurement of the side (the whole side that was facing to the DIC system) of the RC beam.

4.4 Summary

Casting of a RC beam was described in this chapter. Rebar tension test and concrete compression test were reported. The test results were used to yield required parameters in FE package. The materials testing results were also used to determine the maximum loading level in the four-point bending test. The RC concrete beam was used in a four-point bending test undergoes a monotonic cyclic loading (four cycles). The test specimen instrumentations and boundary conditions of the experiment were illustrated. Loading conditions and levels were illuminated in this chapter. Data acquitting resolutions were mentioned. The collected data from the four-point bending test will be used to valid the FE model of the RC beam specimen in the next chapter, Chapter 5.

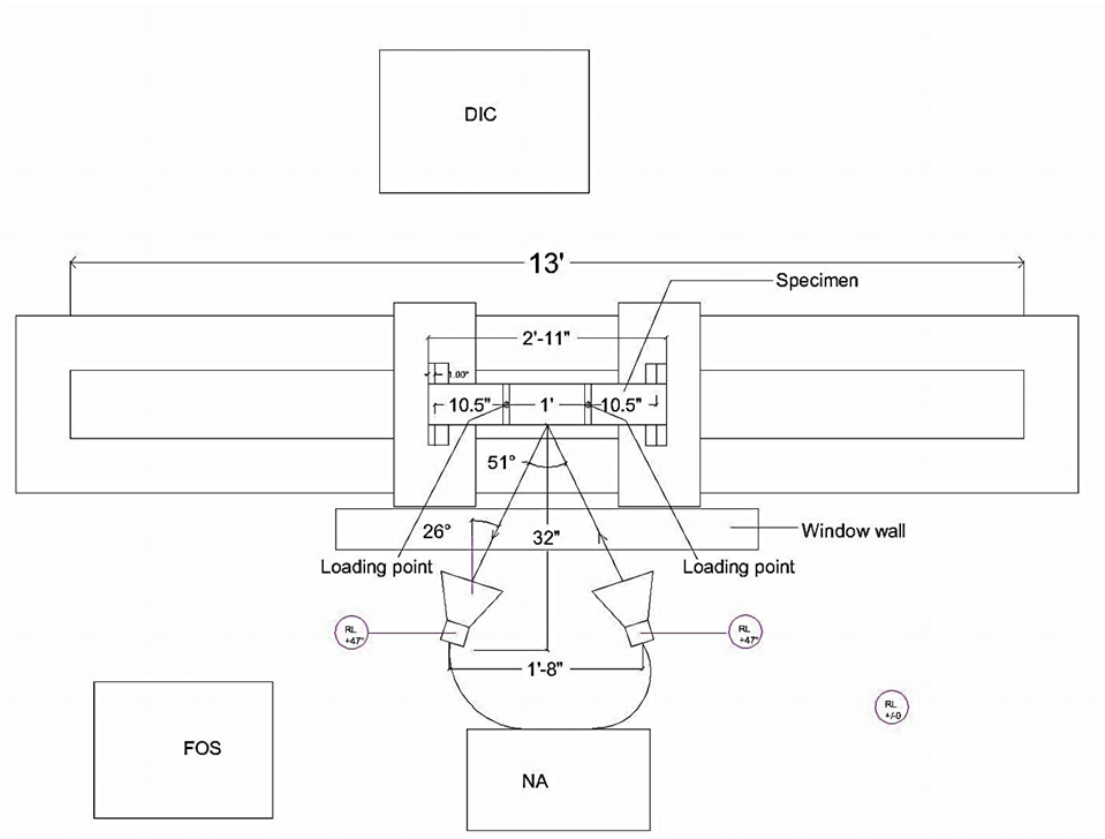

Figure 4-12: The four-point bending beam test layout

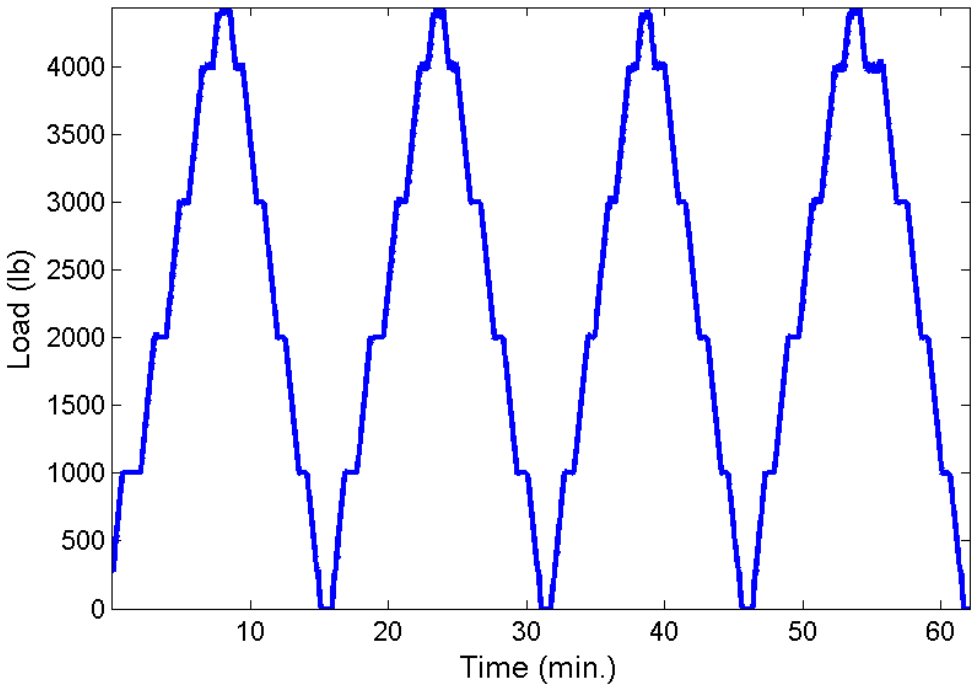

Figure 4-13: Loading cycles of the four-point bending test

Chapter 5

Experimental and Numerical Results

5.1 Introduction

In this chapter, results of the four-point bending tests on a RC beam and simulated responses of RC beam models are reported. The experiment results (surface strain measurement using FOS, ϵ_{33}) are used to validate the FE model of an intact RC beam. Thereafter, FE analysis results of different damage scenarios are discussed. From the simulated response of the damaged RC models, relationships are developed between the change in surface stress-field/strain-field and the internal intensity of damages. Eventually, a procedure is proposed to identify internal damages(s) in the RC beam.

5.2 Experimental Results

Fig. 5-1 shows the FOS configuration in the experiments. The loading cycles in the experiments were shown in Fig. 4-13. The FOS measurements during the monotonic

cyclic loading are shown in Fig. 5-2. A low pass filter, parameters used in the filter design: Fp (frequency at the edge of the passband) = 0.01; Fst (frequency at the beginning of the stopband) = 0.25, Ap (passband ripple in dB) = 0.2, and Ast (stopband attenuation in dB) = 60, Zero-phase filtering (filtfilt function in MATLAB ®) used to prevent phase shift from the fixed time domain, was used to reduce noises in the FOS measurements. Both loading and FOS measurement raw data were in time domain. However, FOS measurements of surface strain due to a known loading level were determined using the FOS measurements during the loading pauses. The FOS measurements at various loading levels were collected using filtered FOS data (*e.g.*, Fig. 5-3). The FOS surface strain measurements at different loading levels were used to validate the FE model of the RC beam.

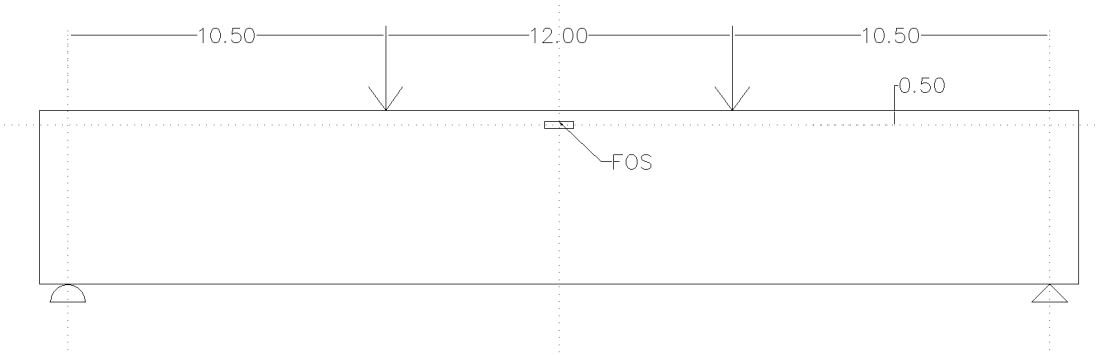

Figure 5-1: FOS configuration during the experiments (all units in inch)

5.3 Numerical Results

Modelling of the RC beam was discussed in the Chapter 3. Fig. 5-4 shows the 3D geometry of the strain field ($\tilde{\epsilon}_{33}$). Fig. 5-5 illustrates the 3D geometry of the strain field on steel rebars. Fig. 5-6 confirms the theoretical relation between rebar stress and concrete

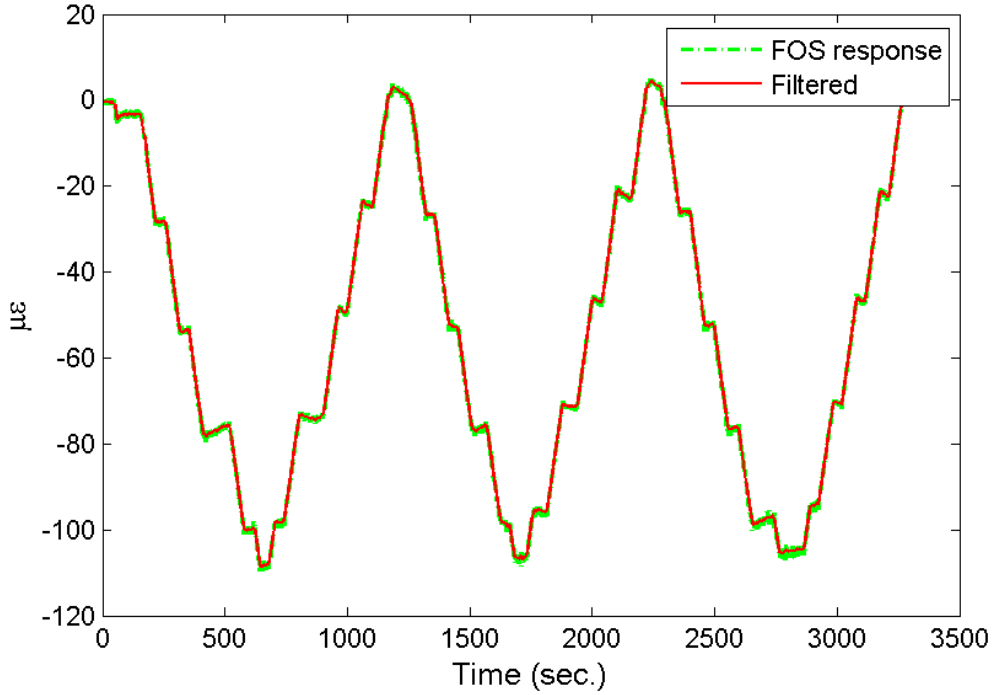

Figure 5-2: FOS response in the beam on January 25, 2013

stress, $(\sigma_{33})_s = n(\sigma_{33})_c$, where $n = \frac{E_s}{E_c}$.

Fig. 5-7 illustrates a good correlation among theoretical calculations, FOS measurements, and FE analysis results. In theoretical calculation, σ_c was computed using Eq. (4.3). Fig. 5-8 compares FE analysis results with FOS measurements at loading levels of 0.5 kip to 2.2 kips. Thus, the intact FE model of the RC beam was validated.

5.4 Artificial Damage Identification

The surface stress matrix ($\tilde{\sigma}_k^o$) of both longitudinal sides of the modelled intact RC beam were extracted from ABAQUS® analysis results. Surface stress matrix ($\tilde{\sigma}_k^j$) on the sides of the RC beam at different damage levels (ΔA_s were 36%, 30%, 25%, 20%,

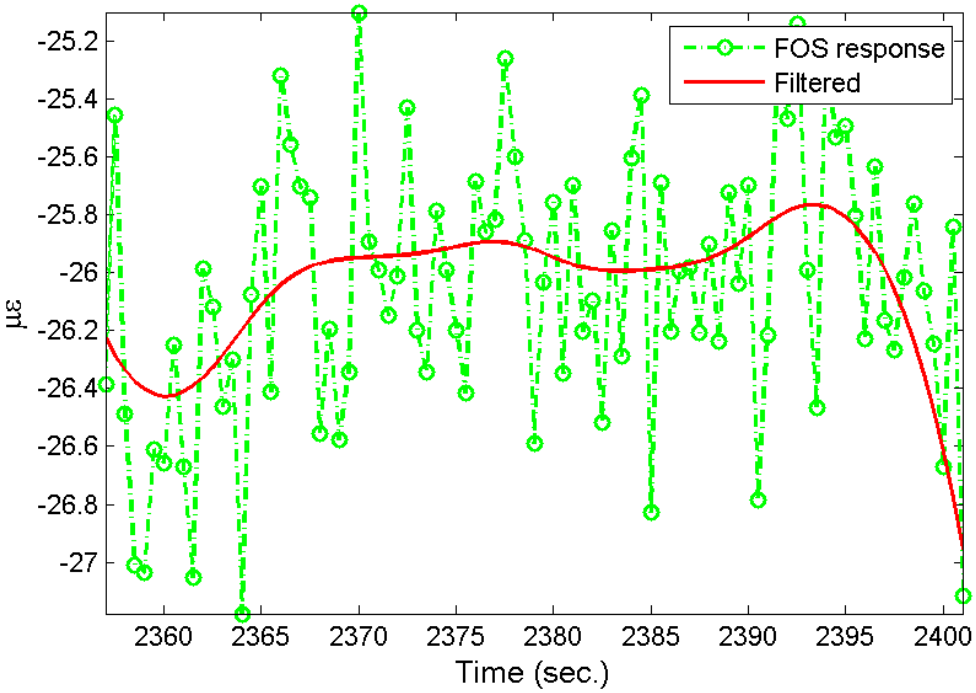

Figure 5-3: FOS response and filtered data

15%, and 10%) in different damage types were also acquired from the FE analysis results. Stress difference ($\Delta_j\tilde{\sigma}_k$) are calculated using Eq. (5.1).

$$\Delta_j\tilde{\sigma}_k = \tilde{\sigma}_k^j - \tilde{\sigma}_k^o \tag{5.1}$$

In Eq. (5.1), superscripted j in $\tilde{\sigma}_k^j$ presents the level of the damage (ΔA_s). By plotting the $\tilde{\sigma}_k^j$, the corresponding location of the damage can be determined. Using $\Delta_j\tilde{\sigma}_k$, contour maps were created for each damage level. The contour area ($A_{\Delta\sigma}$) on the side of the RC beam of a certain stress difference in each damage level was calculated. The highest stress deference ($\Delta\sigma_{max}$) in each matrix was determined. Eventually, the volume losses of the rebar (ΔV_s) as defined in Eq. (3.8) were expressed as the functions of $A_{\Delta\sigma}$ and $\Delta\sigma_{max}$ for each damage case. The general form of the relationships are

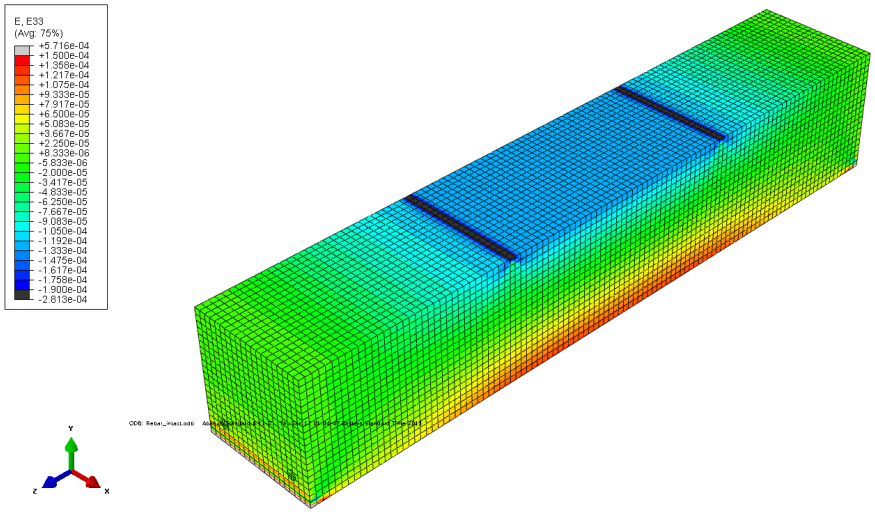

Figure 5-4: Geometry of 3D strain-field ($(\epsilon_{33})_c$) at M = 23.1 k-in

Eq. (5.2) and Eq. (5.3).

$$\Delta V_s = a(A_{\Delta\sigma})^n + b(A_{\Delta\sigma})^{n-1} + c(A_{\Delta\sigma})^{n-2} + \ldots\ldots\ldots + a1(A_{\Delta\sigma}) + C_1 \qquad (5.2)$$

$$\Delta V_s = p(\Delta\sigma_{max})^n + q(\Delta\sigma_{max})^{n-1} + r(\Delta\sigma_{max})^{n-2} + \ldots\ldots\ldots + p1(\Delta\sigma_{max}) + C_2 \qquad (5.3)$$

From the relationship equations (Eq. (5.2) and Eq. (5.3)), damage type and damage intensity can be determined.

A relation between contour area ($A_{\Delta\sigma}$) and contour volume ($V_{\Delta\sigma}$) of the stress-field difference is establish for damage Type I-I. General form of the relationship is a polynomial in Eq. (5.4). $A_{\Delta\sigma}$ in Eq. (5.2) can be replace from Eq. (5.4) and a relationship between ΔV_s and $V_{\Delta\sigma}$ can be established.

$$A_{\Delta\sigma} = A(V_{\Delta\sigma})^n + B(V_{\Delta\sigma})^{n-1} + C(V_{\Delta\sigma})^{n-2} + \ldots\ldots\ldots + A1(V_{\Delta\sigma}) + C_3 \qquad (5.4)$$

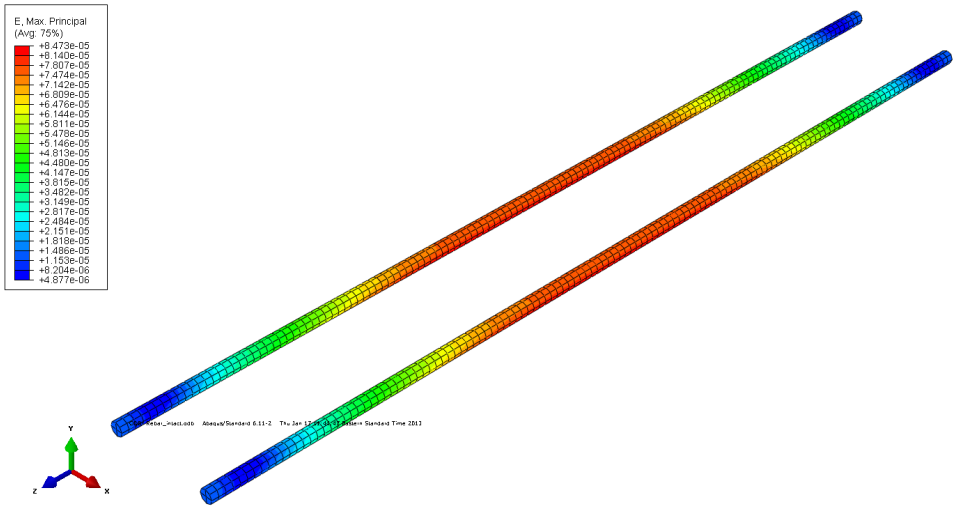

Figure 5-5: Geometry of 3D strain-field ($(\epsilon_{33})_s$) of the rebars at M = 23.1 k-in

5.4.1 Damage Type I

Damage Type I is classified into two categories: a) symmetric damage (Type I-I) and b) nonsymmetric damage (Type I-II).

For damage Type I-I, the cross sections of the both rebars at the mid-span were reduced by 36%, 30%, 25%, 20%, 15%, and 10%. Fig. 3-9 illustrates the artificially introduced damages and locations of the damages. Fig. 3-10 illustrates the artificially introduced damages and locations of the damage Type I-II. In damage Type I-II, one rebar has damaged. Fig. 5-9 illustrates a zone of interest for Type I-I.

Fig. 5-10 shows the $\Delta_{36}\tilde{\sigma}_k$, the the artificial internal damage location (36% cross sectional loss of rebar) can be identified.

In Fig. 5-11, (a) and (b) present $\tilde{\sigma}_k^o$ and $\tilde{\sigma}_k^{36}$ in damage Type I-I, respectively. Using Eq. (5.1), $\Delta_j\tilde{\sigma}_k$ can be determined ((c) in Fig. 5-11). The shaded contour area for $\tilde{\sigma}_k^j$ in Fig. 6.1 was calculated, and maximum stress differences in the $\tilde{\sigma}_k^j$ were determined.

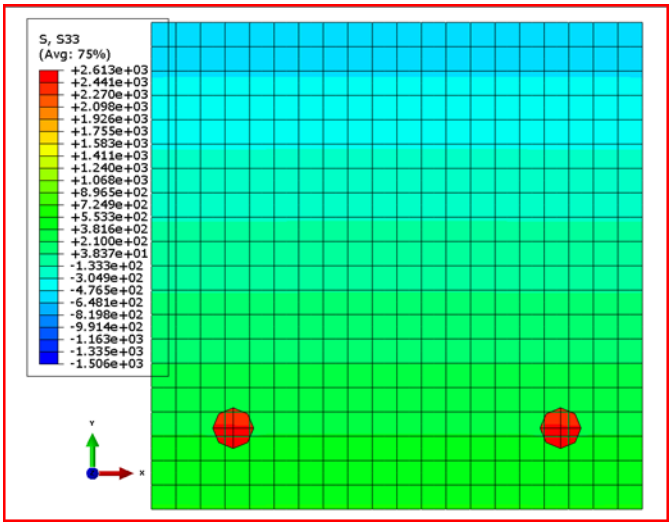

Figure 5-6: Stress-field in the mid-section of the RC beam

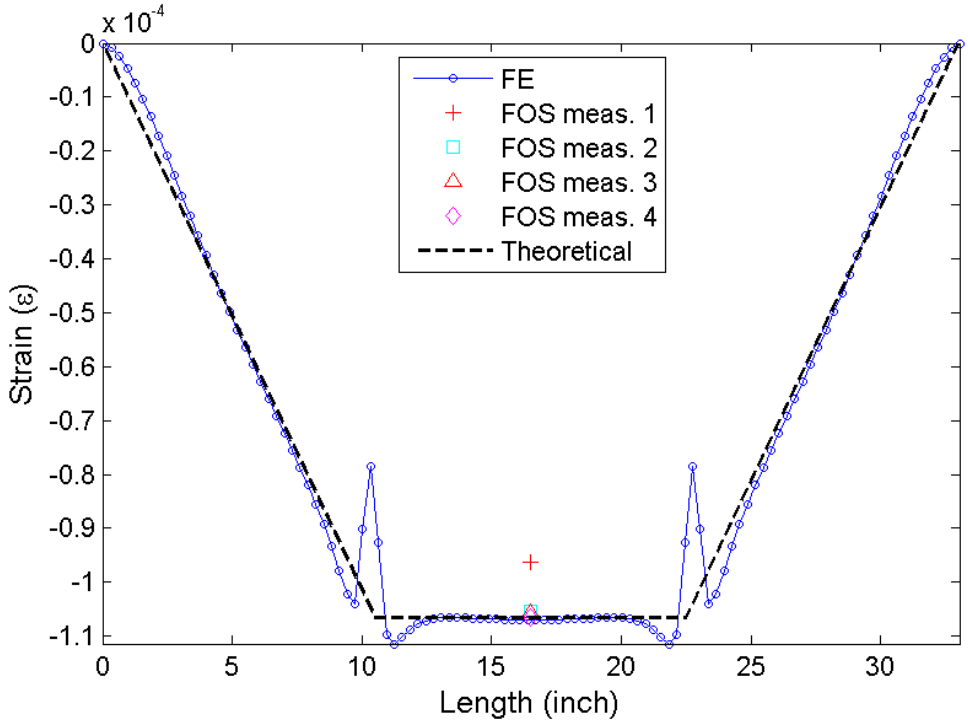

Figure 5-7: Experimental, numerically-obtained and theoretically-calculated strain

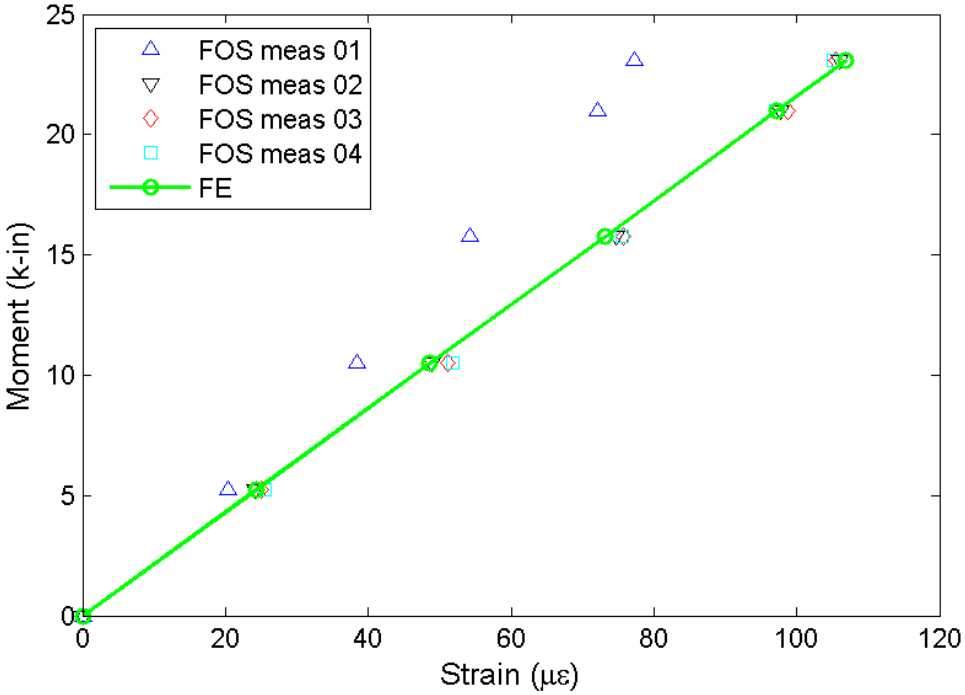

Figure 5-8: Numerical vs. experimental ϵ_{33} values at different loading levels

It is observed that the affected area (stress difference) is larger when the damage is nonsymmetric (Type I-II). In Fig. 5-13, A_1 is considered. In symmetric case (Type I-I), the relationship between the contour area of stress differences and the rebar volume reduction (poly3 in Fig. 5-13) can be expressed in the following:

$$\Delta V_s = 0.00963A_{\Delta\sigma}^3 - 0.05696A_{\Delta\sigma}^2 + 2.169A_{\Delta\sigma} + 0.01394 \quad (5.5)$$

In the nonsymmetric (Type I-II) case, the relationship between the contour area of stress differences and rebar volume reduction ('linear' in Fig. 5-13) can be expressed in the following:

$$\Delta V_s = 1.922A_{\Delta\sigma} + 0.094 \quad (5.6)$$

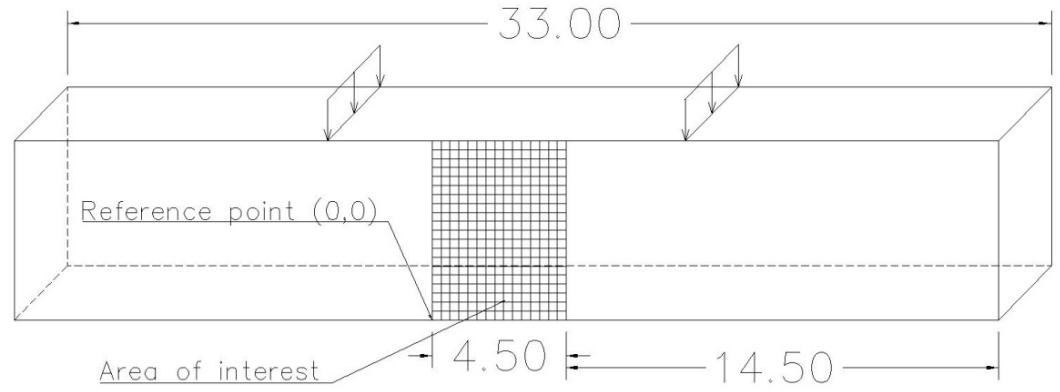

Figure 5-9: Location of ZOI (all units in inch)

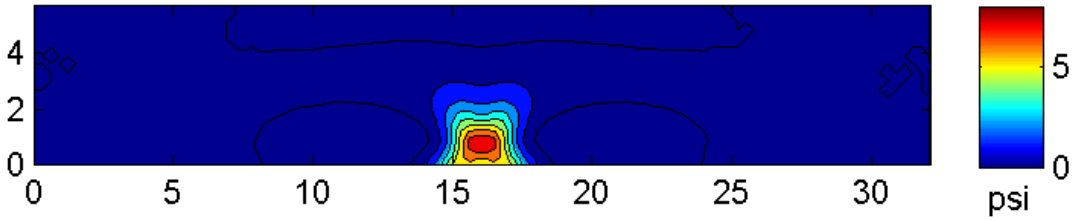

Figure 5-10: Surface stress difference due to damage Type I-I, $\Delta_{36}\tilde{\sigma}_k$ (damage intencity was 36% cross sectional reducton on both rebars)

In Type I-I and Type I-II, the relationship between maximum value on the contour area of stress differences and rebar volume reduction can be expressed in Eq. (5.7) and Eq. (5.8). In Fig. 5-14, Eq. (5.7) and Eq. (5.8) are poly2 and poly2-non-sym.

$$\Delta V_s = -0.0394\Delta\sigma_{max}^2 + 3.442\Delta\sigma_{max} + 0.04076 \tag{5.7}$$

$$\Delta V_s = -0.03449\Delta\sigma_{max}^2 + 3.37\Delta\sigma_{max} + 0.04028 \tag{5.8}$$

Figs. 5-15 to 5-18 illustrate the relationships of $\Delta_j\tilde{\sigma}_k$, $\tilde{\sigma}_k^j$, $\tilde{\sigma}_k^o$ on both sides of the RC beam.

The contour volume ($V_{\Delta\sigma}$) of $\Delta_j\tilde{\sigma}_k$ were computed. Fig. 5-20 illustrate $V_{\Delta\sigma}$ when

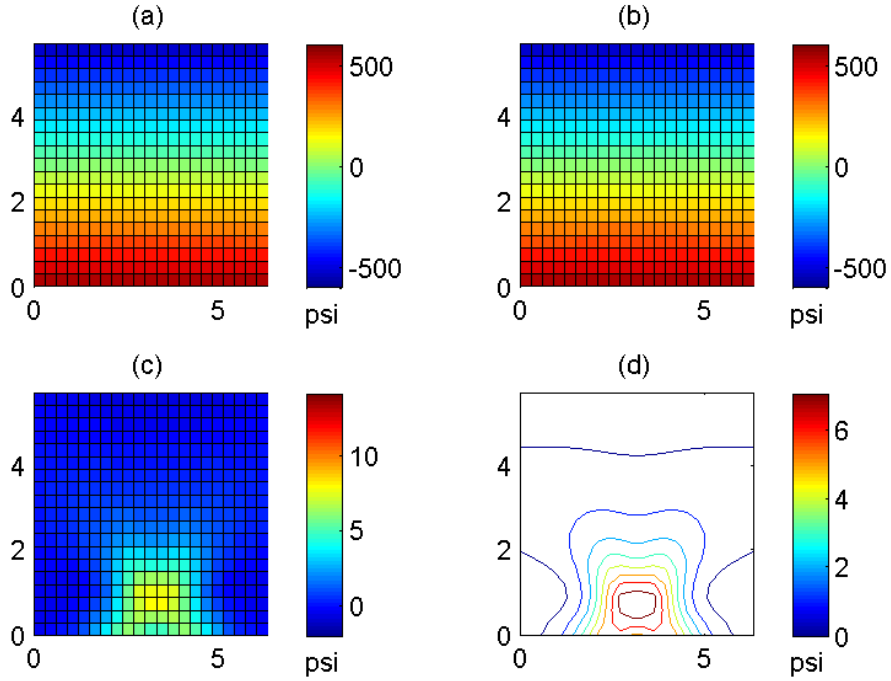

Figure 5-11: Stresses in ZOI in damage Type I-I

ΔA_s = 36% in damage type I-I. A relation between $A_{\Delta\sigma}$ and $V_{\Delta\sigma}$ of the stress-field difference was established. Fig. 5-19 illustrates the relationship between $A_{\Delta\sigma}$ and $V_{\Delta\sigma}$. poly2 in the Fig. 5-19 can be expressed by Eq. (5.9). By replacing $A_{\Delta\sigma}$ from Eq. (5.9) to Eq. (5.5), relationship between $V_{\Delta\sigma}$ and ΔV_s can be established.

$$A_{\Delta\sigma} = -0.002891(V_{\Delta\sigma})^2 + 0.2977(V_{\Delta\sigma}) + 2.156 \quad (5.9)$$

5.4.2 Damage Type II

Cross sectional reduction of area, ΔA_s of the rebars at 8.5 inch from the right support and the center of the damage were 36%, 30%, 25%, 20%, 15%, and 10%. Damage length was 1 inch. Type II was classified into two categories: a) symmetric damage

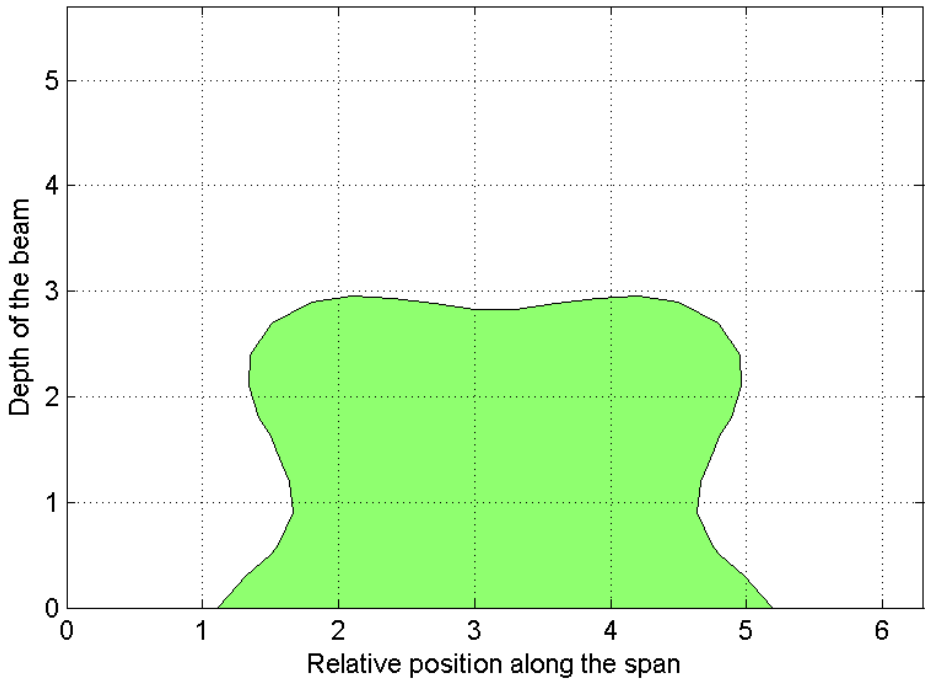

Figure 5-12: Contour area of 1 psi stress difference in damage Type I-I (ΔA_s = 36%)

(Type II-I) and b) nonsymmetric damage (Type II-II). In Type II-I damage, an artificial damage was introduced to both rebars while in Type II-II one of the rebars had the damage. Fig. 3-11 and Fig. 3-12 illustrate Type II-I and Type II-II damages, respectively.

Fig. 5-21 shows the $\Delta_{36}\tilde{\sigma}_k$, the the artificial internal damage location (36% cross sectional loss of rebar) can be identified.

In Fig. 5-22, (a) and (b) present $\tilde{\sigma}_k^o$ and $\tilde{\sigma}_k^{36}$ in damge Type II-I, respectively. Using Eq. (5.1), $\Delta_j\tilde{\sigma}_k$ can be determined ((c) in Fig. 5-22). The shaded contour area for $\tilde{\sigma}_k^j$ in Fig. 5-23 was calculated, and maximum stress differences in the $\tilde{\sigma}_k^j$ were determined.

It is observed that the affected area (stress magnitude difference) is larger when the damage is nonsymmetric (Type II-II). In Fig. 5-24, A_1 is considered. In the symmetric

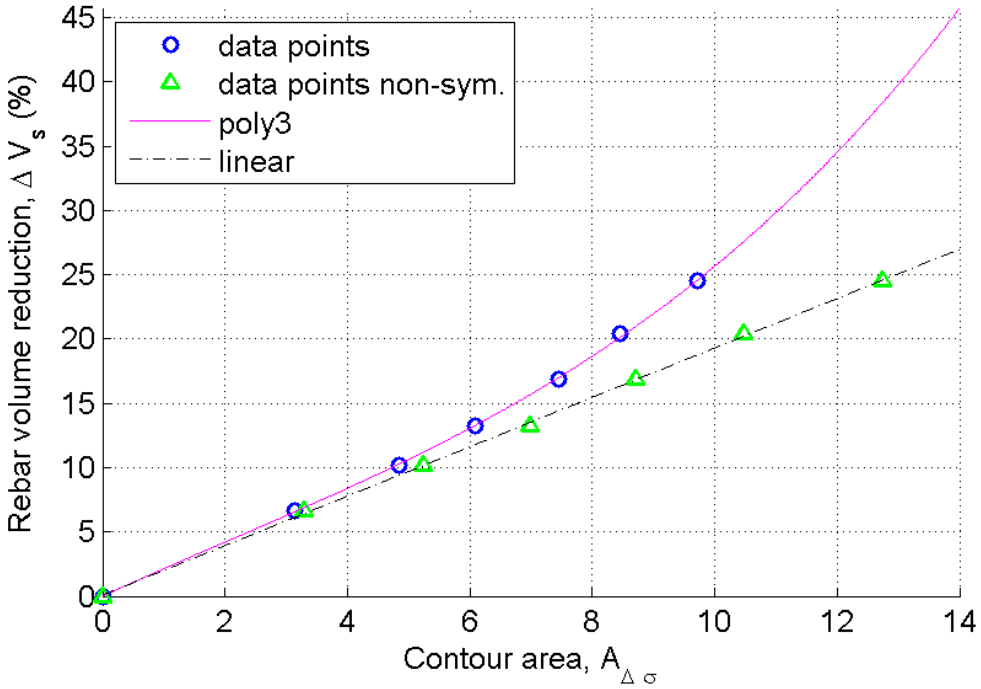

Figure 5-13: Relationship between rebar volume reduction and contour area of stress differences in damage Type I-I and Type I-II (on side A_1)

case (Type II-I), the relationship between contour area of stress differences and rebar volume reduction (poly3 in Fig. 5-24) can be expressed in the following:

$$\Delta V_s = 0.02307A_{\Delta\sigma}^3 - 0.2155A_{\Delta\sigma}^2 + 3.069A_{\Delta\sigma} + 0.05642 \qquad (5.10)$$

In the nonsymmetric (Type II-II) case, the relationship between the contour area of stress differences and rebar volume reduction ('linear' in Fig. 5-24) can be expressed in the following:

$$\Delta V_s = 2.316A_{\Delta\sigma} + 0.4188 \qquad (5.11)$$

In Type II-I and Type II-II, the relationship between maximum value on the contour

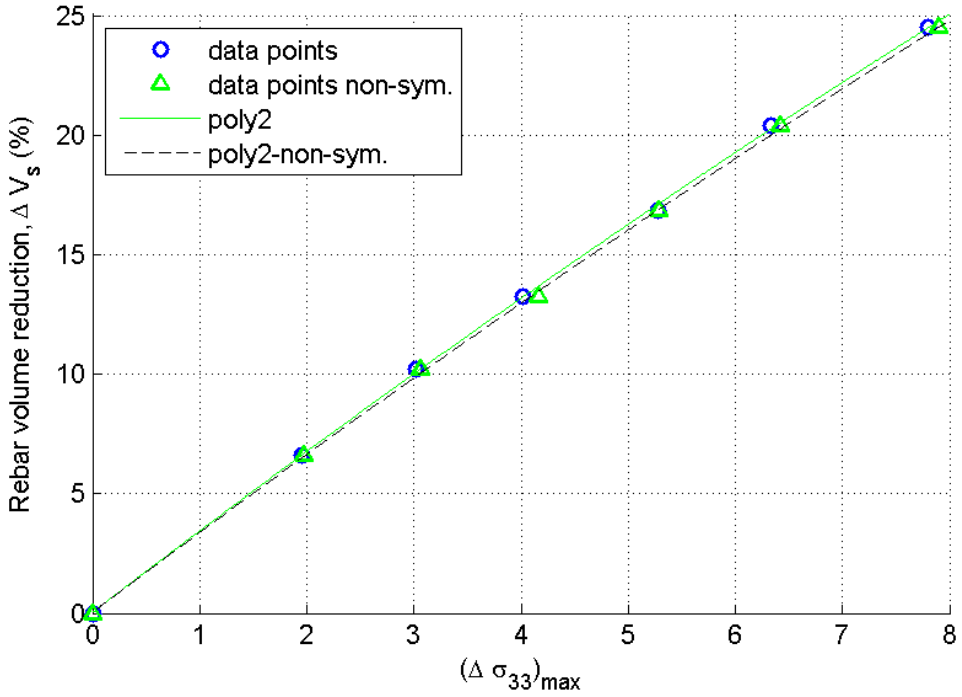

Figure 5-14: Relationship between maximum value on the contour area of stress differences and rebar volume reduction of Type I-II and Type I-II (on side A_2)

area of stress differences and rebar volume reduction can be expressed by Eq. (5.12) and Eq. (5.13). In Fig. 5-25, Eq. (5.12) and Eq. (5.13) are poly2 and poly2-non-sym.

$$\Delta V_s = -0.05026\Delta\sigma_{max}^2 + 4.159\Delta\sigma_{max} + 0.03931 \tag{5.12}$$

$$\Delta V_s = -0.0784\Delta\sigma_{max}^2 + 4.307\Delta\sigma_{max} + 0.06134 \tag{5.13}$$

Figs. 5-26 to 5-29 illustrate the relationships of $\Delta_j\tilde{\sigma}_k$, $\tilde{\sigma}_k^j$,$\tilde{\sigma}_k^o$ on both sides of the RC beam.

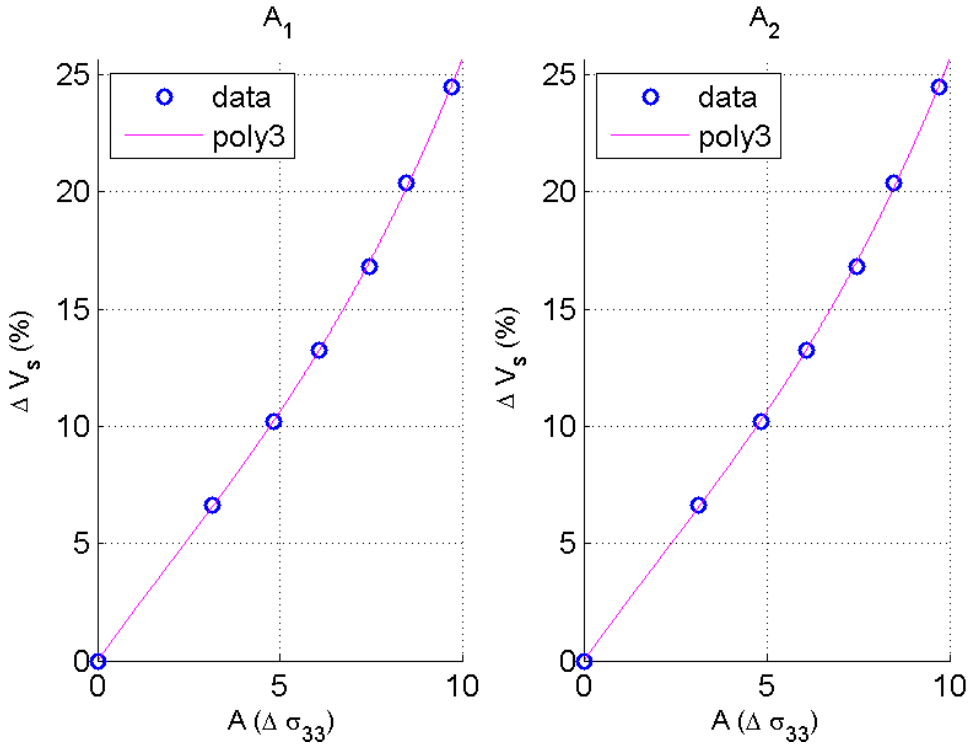

Figure 5-15: Relationship between rebar volume reduction and the contour area of stress difference in the damage Type I-I

5.4.3 Damage Type III

Cross sectional reduction of area, ΔA_s of the rebars, one at 8.5 inches from the right support and another one 8.5 inches from left support and the center of the damages were 36%, 30%, 25%, 20%, 15%, and 10%. The damage length was 1 inch. Fig. 3-13 illustrates the Type III damage.

Figs. 5-30 and 5-31 show the $\Delta_{36}\tilde{\sigma}_k$ on both side of the RC beam, the artificial internal damage location (36% cross sectional loss of rebar) can be identified using the these figures.

Relationships of ΔV_s, $A_{\Delta\sigma}$, and $\Delta\sigma_{max}$ on both sides of the beam are identical to the relationships in Eq. (5.10) and Eq. (5.12).

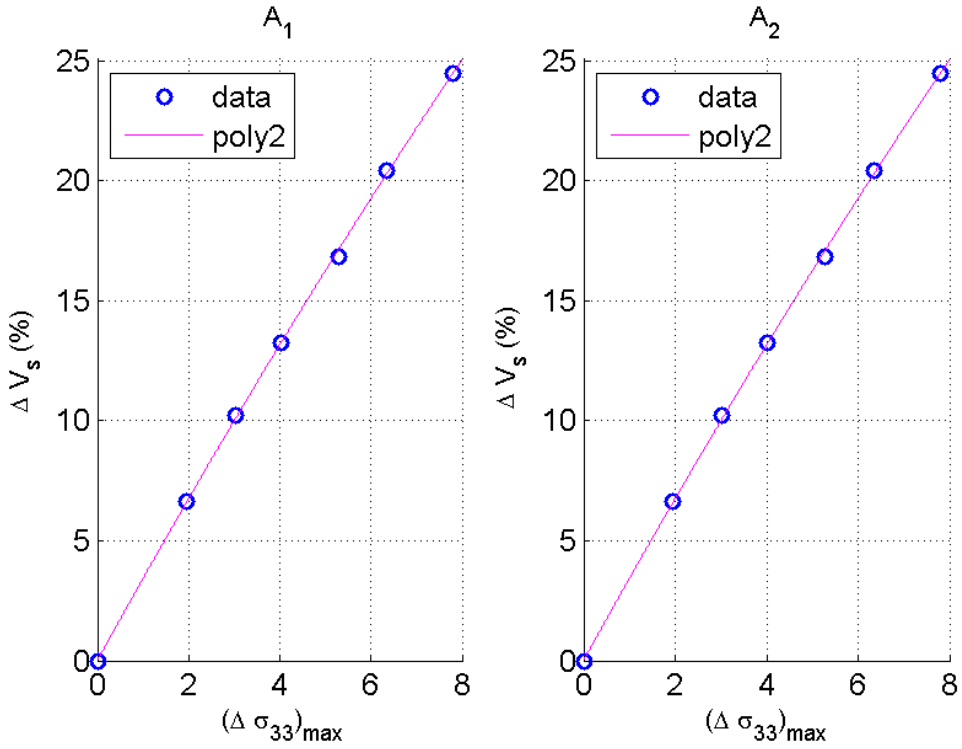

Figure 5-16: Relationship between rebar volume reduction and the maximum of stress difference in damage Type I-I

5.4.4 Damage Type IV

Cross sectional reduction of area, ΔA_s of the rebar at the mid-span and the center of the damage were 36%, 30%, 25%, 20%, 15%, and 10%. The damage length was 5 inches. Type IV was classified into two categories: a) symmetric damage (Type IV-I) and b) nonsymmetric damage (Type IV-II). In type IV-I damage, an artificial damage was introduced to both rebars while in type IV-II only one rebar had the damage. Figs. 3-14 and 3-15 illustrate Type IV-I and Type IV-II damage, respectively.

Fig. 5-32 shows the $\Delta_{36}\tilde{\sigma}_k$, in which the the artificial internal damage location (36% cross sectional loss of rebar) can be identified.

In Fig. 5-33, (a) and (b) show $\tilde{\sigma}_k^o$ and $\tilde{\sigma}_k^{36}$ in damage Type IV-I, respectively. Using

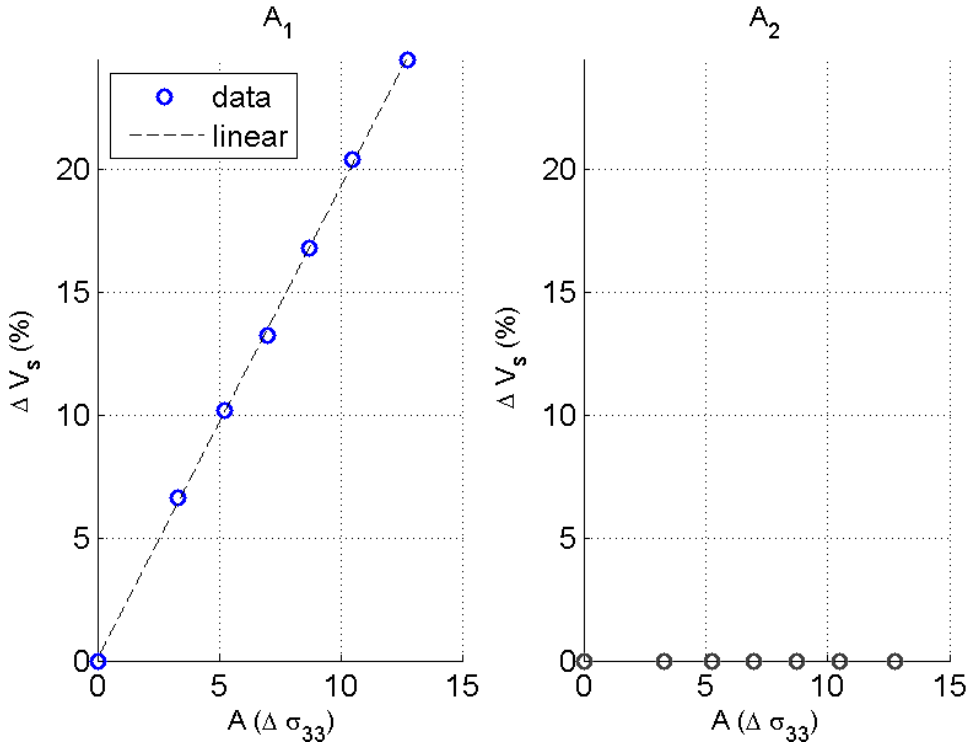

Figure 5-17: Relationship between maximum value on the contour area of stress differences and rebar volume reduction of Type I-II

Eq. (5.1), $\Delta_j\tilde{\sigma}_k$ can be determined ((c) in Fig. 5-22). The shaded contour area for $\tilde{\sigma}_k^j$ in Fig. 5-34 was calculated and maximum stress differences in the $\tilde{\sigma}_k^j$ were determined.

It is observed that the affected area (stress magnitude difference) is larger when the damage is nonsymmetric (Type IV-II). In Fig. 5-35, A_1 is considered. In the symmetric case (Type IV-I), the relationship between the contour area of stress differences and the rebar volume reduction (poly3 in Fig. 5-35) can be expressed by:

$$\Delta V_s = 0.001717A_{\Delta\sigma}^3 - 0.04166A_{\Delta\sigma}^2 + 0.5687A_{\Delta\sigma} + 0.002163 \qquad (5.14)$$

In the nonsymmetric (Type IV-II) case, the relationship between the contour area of stress differences and rebar volume reduction, ('linear' in Fig. 5-35), can be expressed

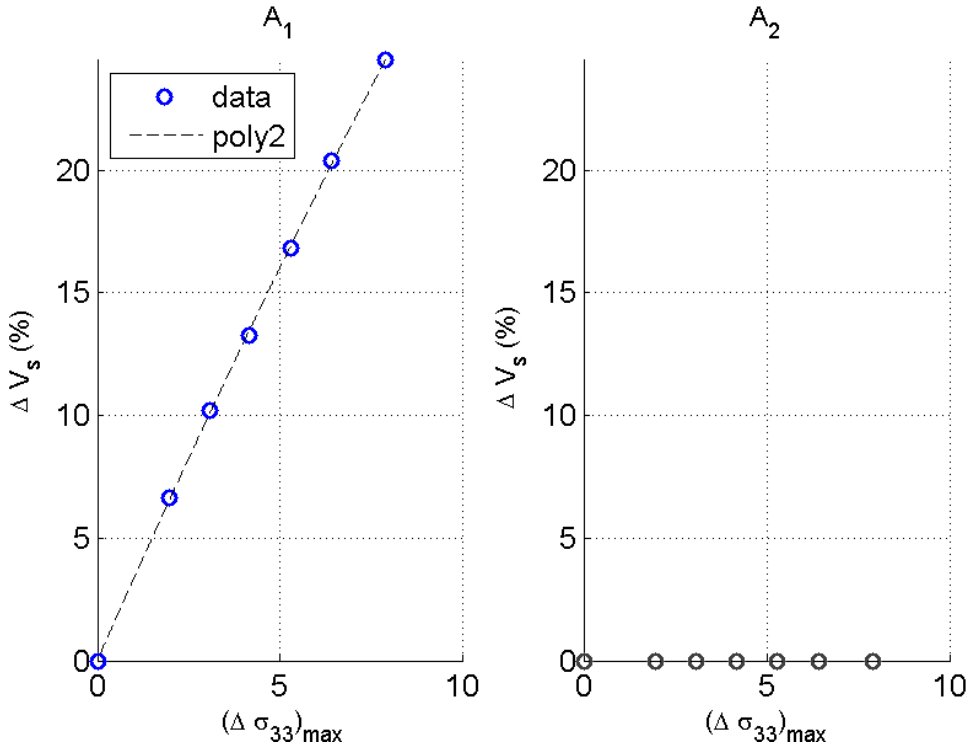

Figure 5-18: Relationship between rebar volume reduction and the maximum of stress difference in the damage Type I-II

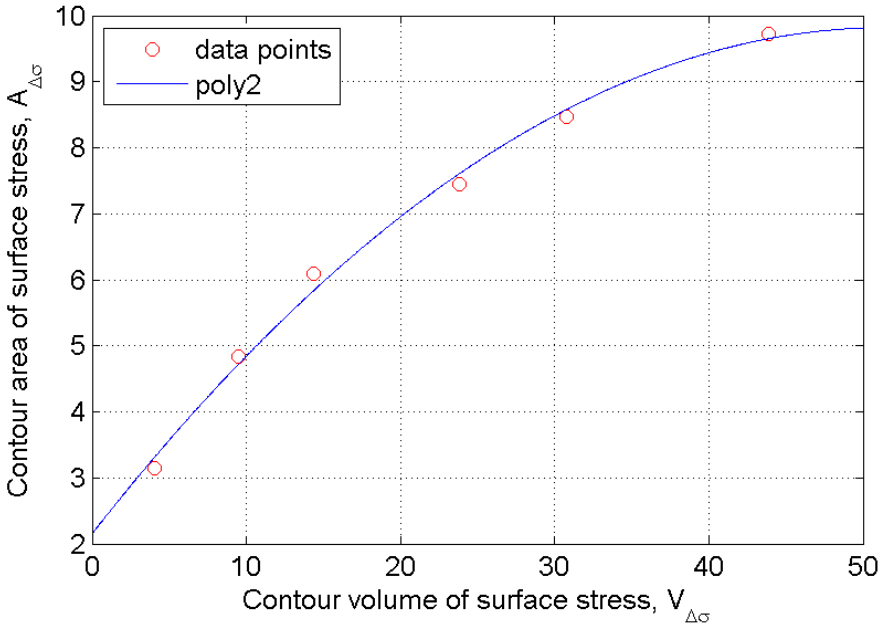

Figure 5-19: Relationship between ($A_{\Delta\sigma}$) and ($V_{\Delta\sigma}$) in the damage Type I-I

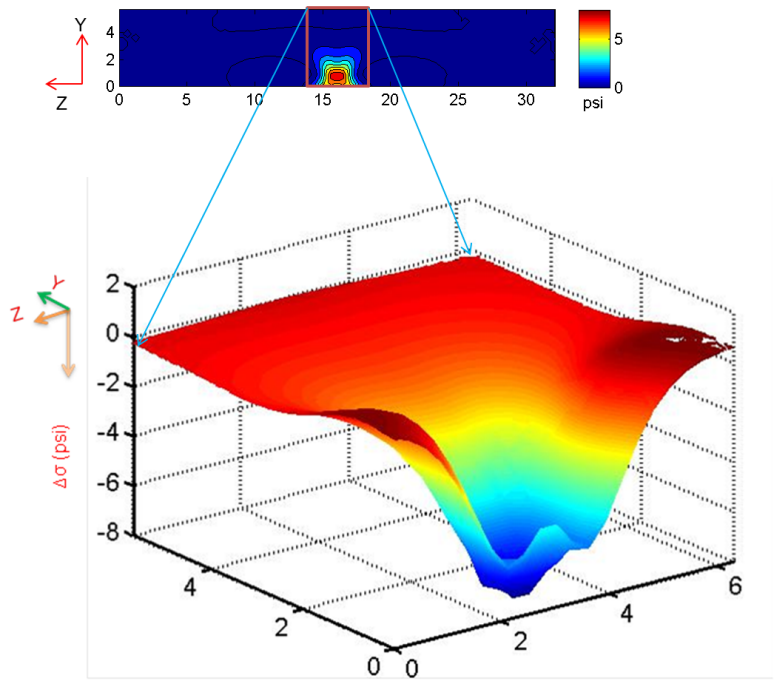

Figure 5-20: $V_{\Delta\sigma}$ in the damage Type I-I when $\Delta A_s = 36\%$

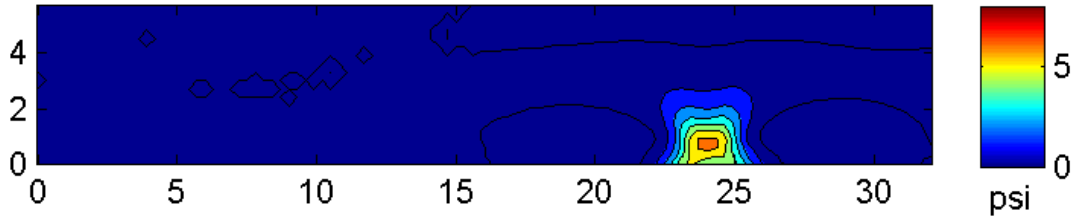

Figure 5-21: Surface stress difference due to damage Type II-I, $\Delta_{36}\tilde{\sigma}_k$ (damage intencity was 36% cross sectional reducton on both rebars)

by:

$$\Delta V_s = 0.005145A_{\Delta\sigma}^2 + 0.1077A_{\Delta\sigma} + 0.1344 \qquad (5.15)$$

In Type IV-I and type IV-II, the relationship between the maximum value on the contour area of stress differences and the rebar volume reduction can be expressed in Eq. (5.16) and Eq. (5.17). In Fig. 5-36, Eq. (5.16) and Eq. (5.17) are poly2 and poly2-

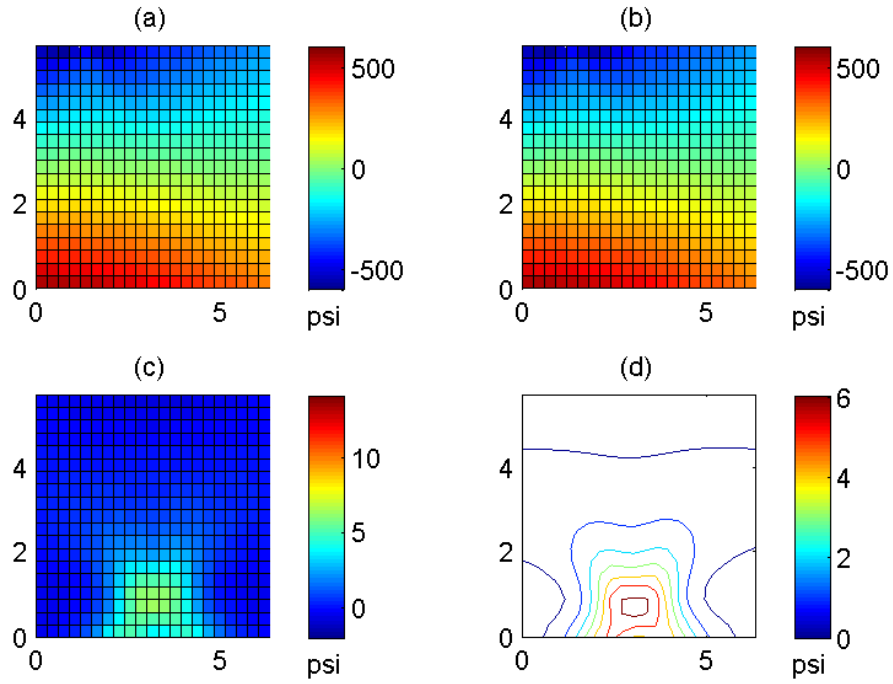

Figure 5-22: Stresses in zone of interest in damage Type II-I

non-sym.

$$\Delta V_s = -0.002078\Delta\sigma_{max}^2 + 0.7823\Delta\sigma_{max} + 0.006746 \tag{5.16}$$

$$\Delta V_s = -0.001835\Delta\sigma_{max}^2 + 0.7849\Delta\sigma_{max} + 0.006225 \tag{5.17}$$

5.5 Proposed Methodology to Identify Damages in RC structures

In this methodology, a FE model of a RC structure need to create according to design specifications and material properties. A load test of the intact RC structure need to conduct to collect surface strain measurements. The FE model may need to fine tune to

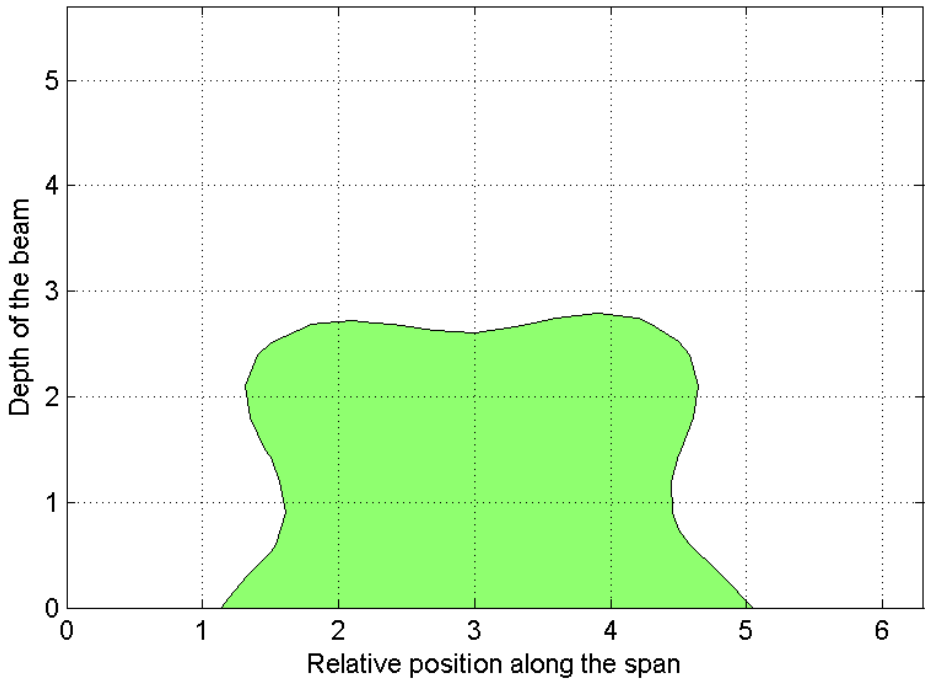

Figure 5-23: Contour area of 1 psi stress difference in damage Type II-I (ΔA_s = 36%)

achieve simulated behaviors of the RC structure (*e.g.*, displacement and surface strain). Potential damages need to introduce to get a data base of surface strain change patterns against the damage types. Relationship between the damage intensity and internal damages need to establish for each damage type. The RC structure should monitor regular interval. If there are any surface strain change observe, a pattern recognition algorithm should use to recognize the damage type. After detecting the damage type, using the relationship between the surface strain change and internal damage intensity, the intensity of internal damage can be detected. A flow chart in the Fig. 5-37 shows a proposed methodology to identify damage type, location(s), and intensity.

Flow chart in Fig. 5-38 illustrates a technique to identify the damage type.

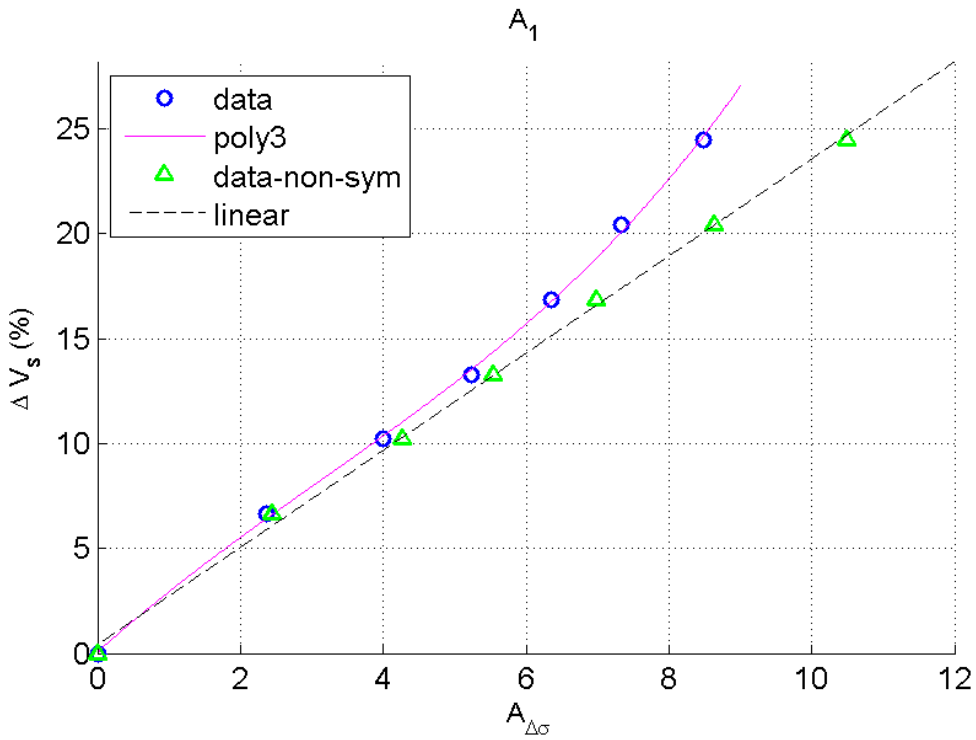

Figure 5-24: Relationship between rebar volume reduction and contour area of stress differences in damage Type II-I and Type II-II (on side A_1)

5.6 Summary

Surface measurements from the FOS during the four-point bending tests were reported. FE models of an intact RC beam were validated using the fiber optic surface strain measurements. FE analysis results of the four damage scenarios (Four damage sceneries were defined in Chapter 3. The damages were modelled by rebars volume loss) were reported. The volume loss of the rebar (ΔV_s) was expressed as functions of $A_{\Delta\sigma}$ and $\Delta\sigma_{max}$ in each damage case. The expressions can be used to determine the internal damage intensities. A methodology is proposed to identify internal damage(s) in the RC beam.

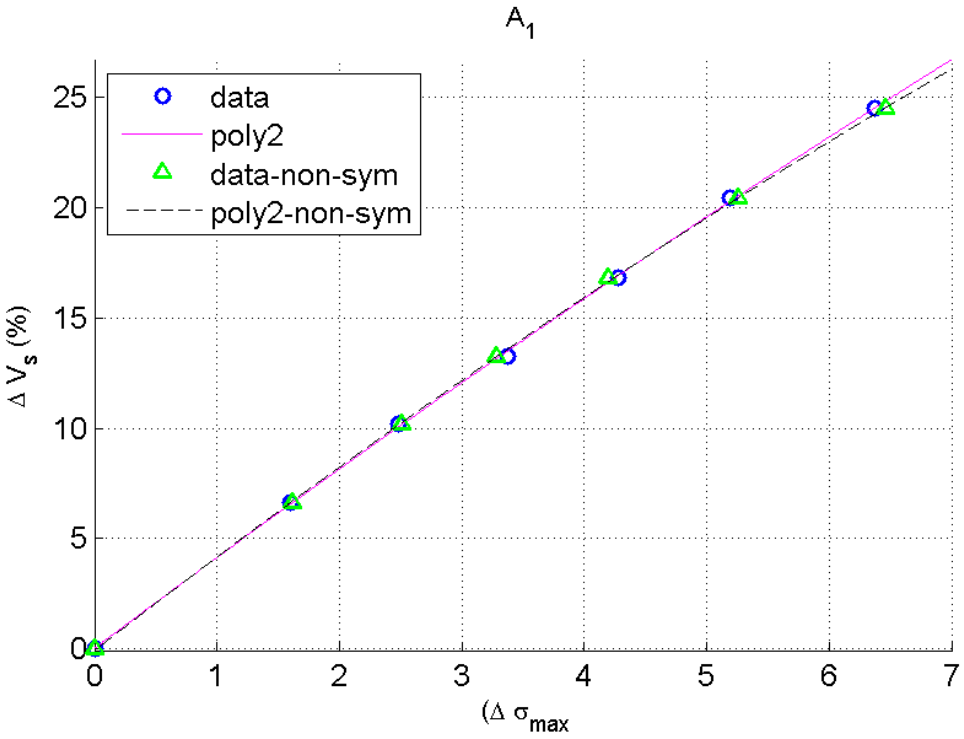

Figure 5-25: Relationship between maximum value on the contour area of stress differences and rebar volume reduction of Type II-I and Type II-II (on side A_1)

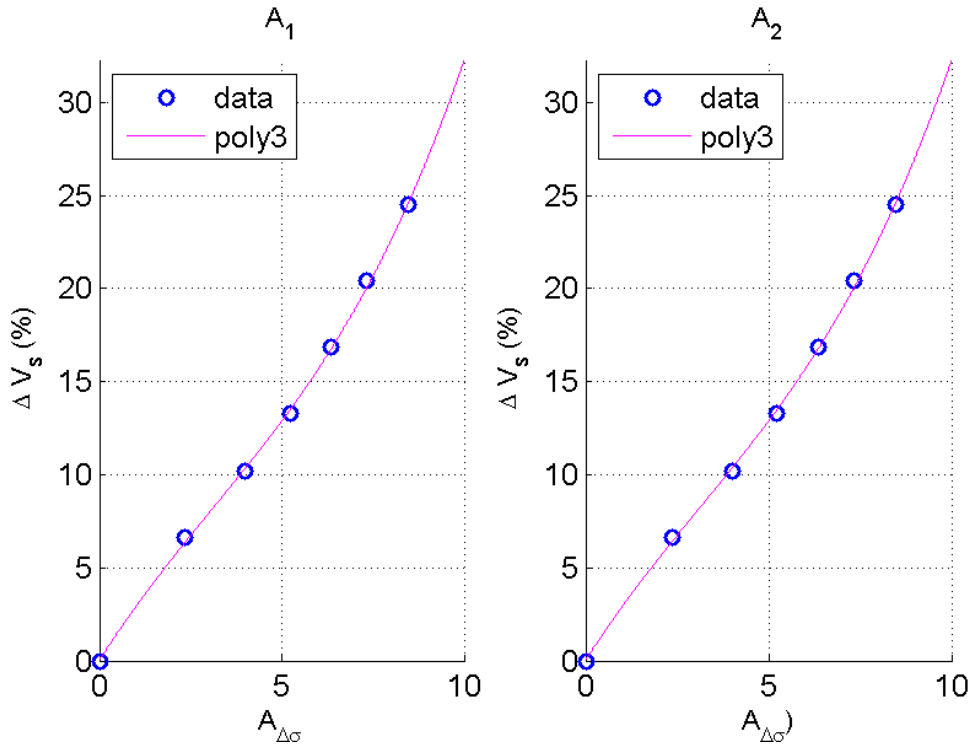

Figure 5-26: Relationship between rebar volume reduction and the contour area of stress difference in the damage Type II-I

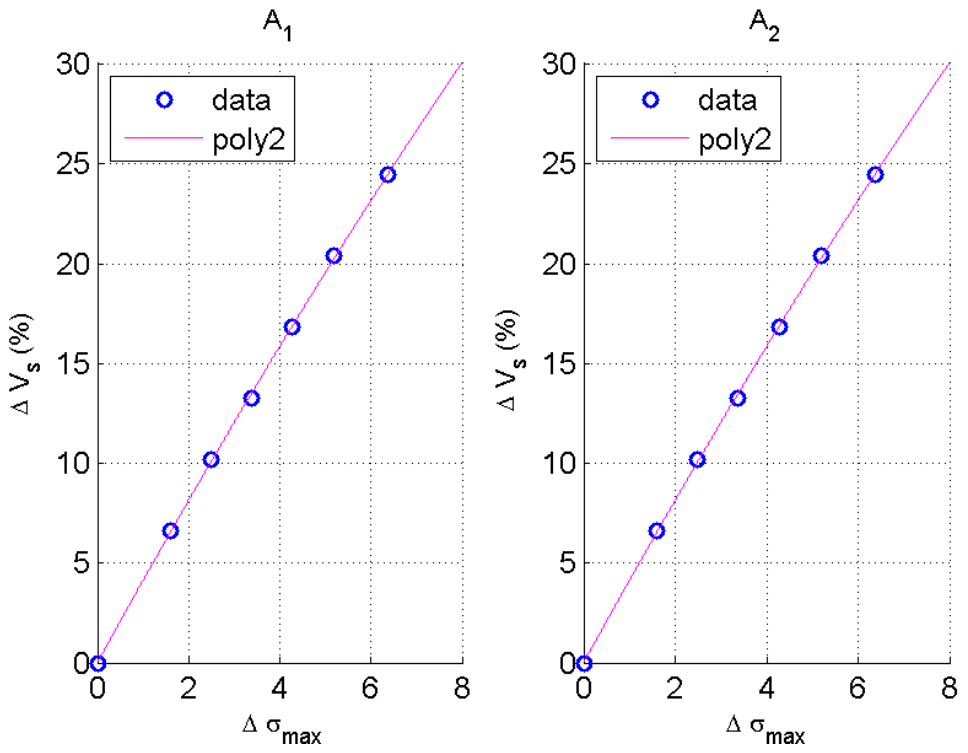

Figure 5-27: Relationship between rebar volume reduction and the maximum of stress difference in damage Type II-I

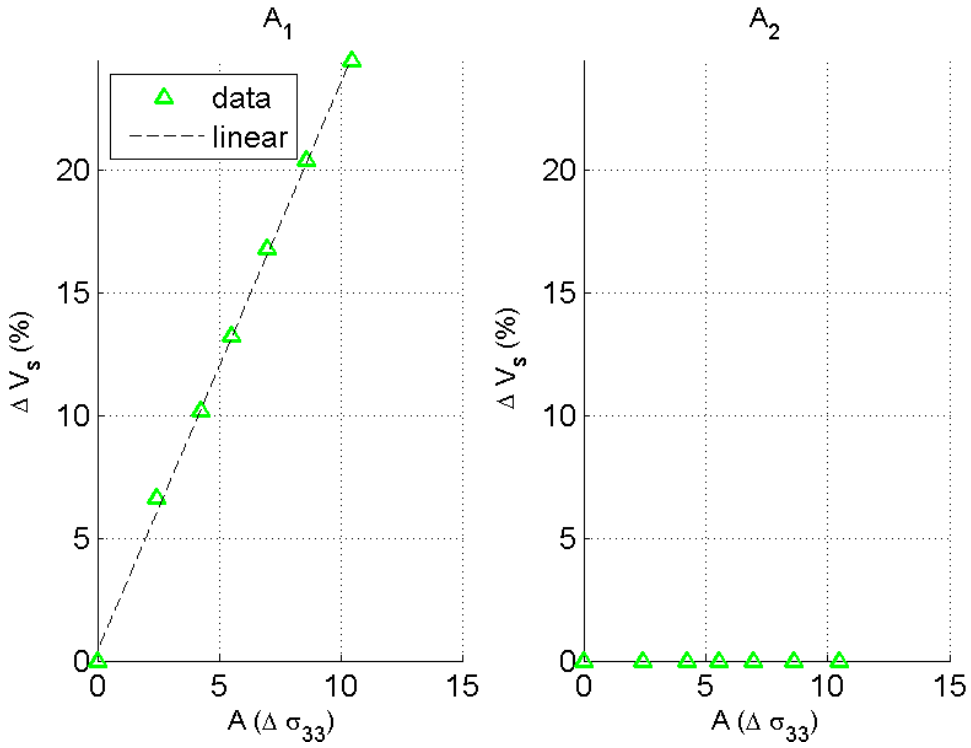

Figure 5-28: Relationship between maximum value on the contour area of stress differences and rebar volume reduction of damage Type II-II

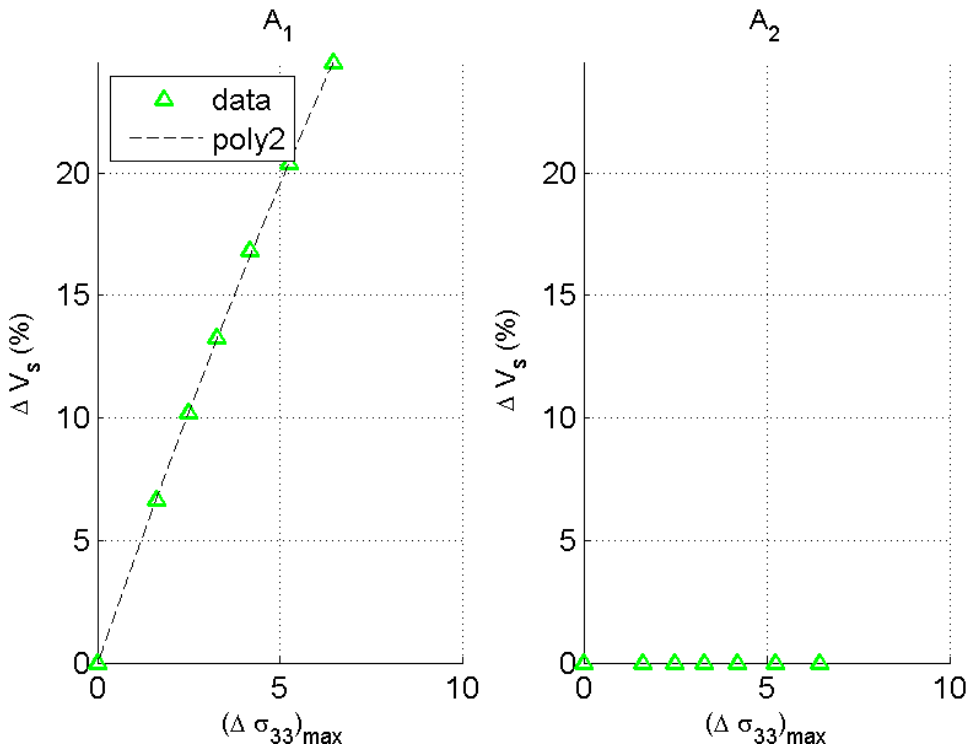

Figure 5-29: Relationship between rebar volume reduction and the maximum of stress difference in the damage Type II-II

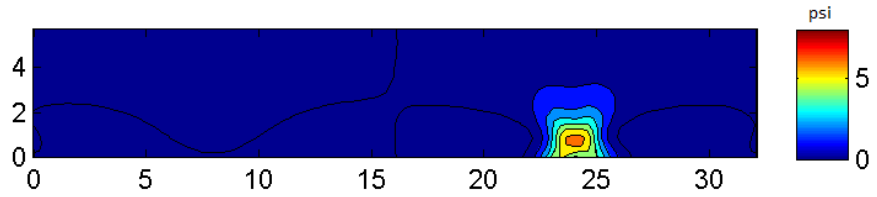

Figure 5-30: Surface stress difference due to damage Type III on side A_1, $\Delta_{36}\tilde{\sigma_k}$ (damage intencity was 36% cross sectional reducton on both rebars)

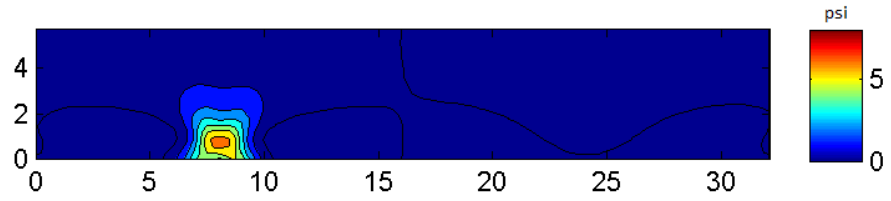

Figure 5-31: Surface stress difference due to damage Type III on side A_2, $\Delta_{36}\tilde{\sigma_k}$ (damage intencity was 36% cross sectional reducton on both rebars)

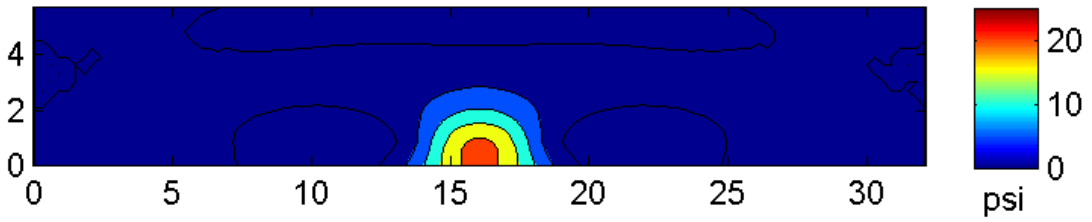

Figure 5-32: Surface stress difference due to damage Type IV-I, $\Delta_{36}\tilde{\sigma}_k$ (damage intencity was 36% cross sectional reducton on both rebars)

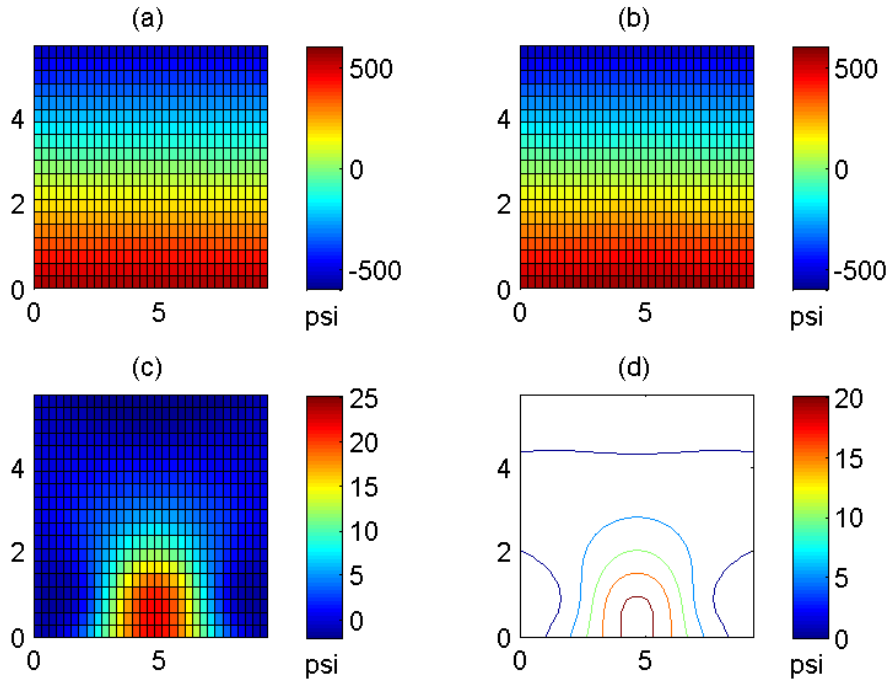

Figure 5-33: Stresses in zone of interest in damage Type IV-I

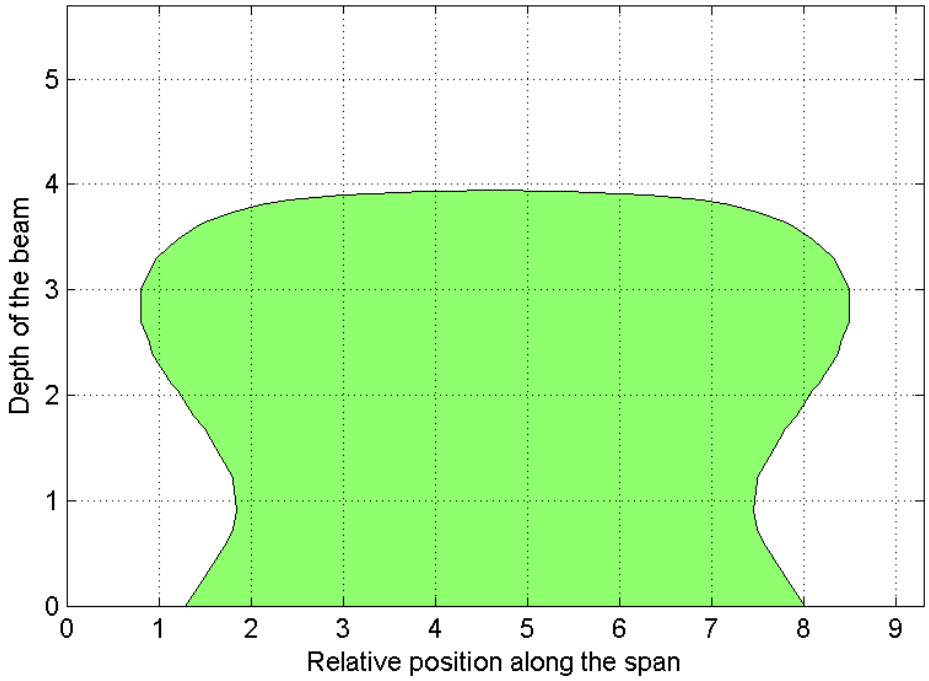

Figure 5-34: Area of least 1 psi magnitude change when damage was 36% reduction in rebars cross section in damage Type IV-I

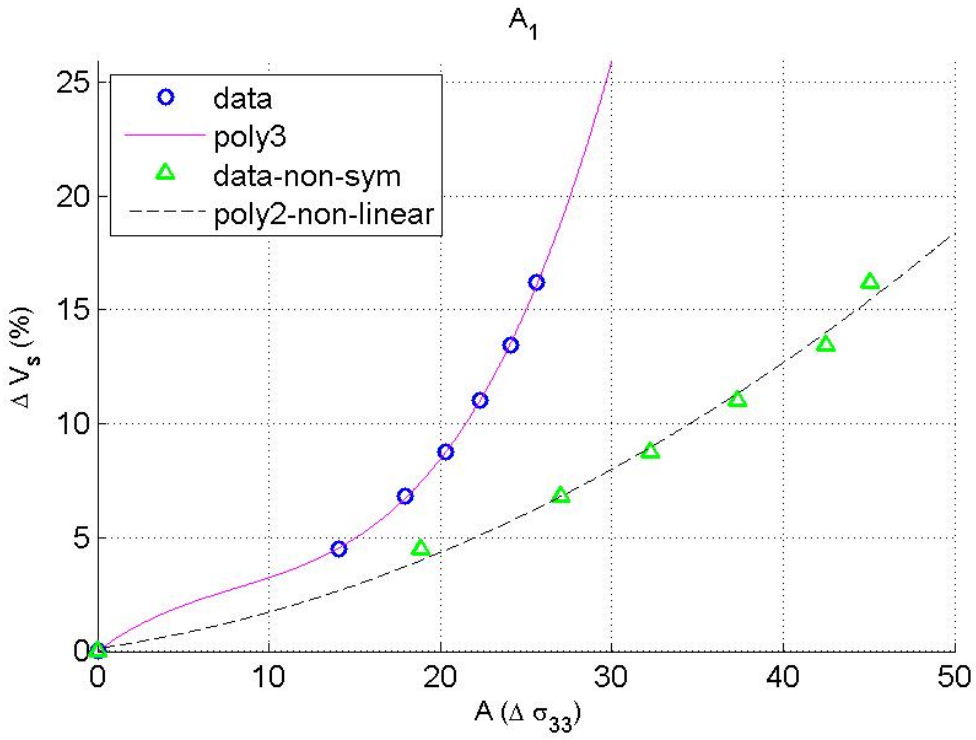

Figure 5-35: Relationship between rebar volume reduction and contour area of stress differences in damage Type IV-I and Type IV-II (on side A_1)

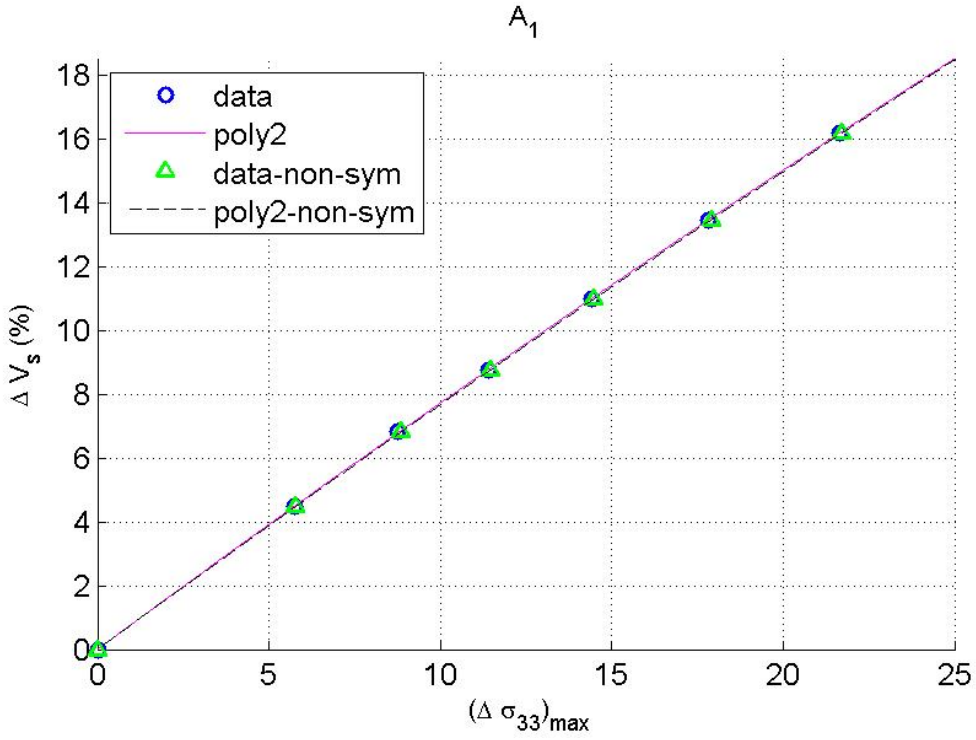

Figure 5-36: Relationship between maximum value on the contour area of stress differences and rebar volume reduction of Type IV-I and Type IV-II (on side A_1)

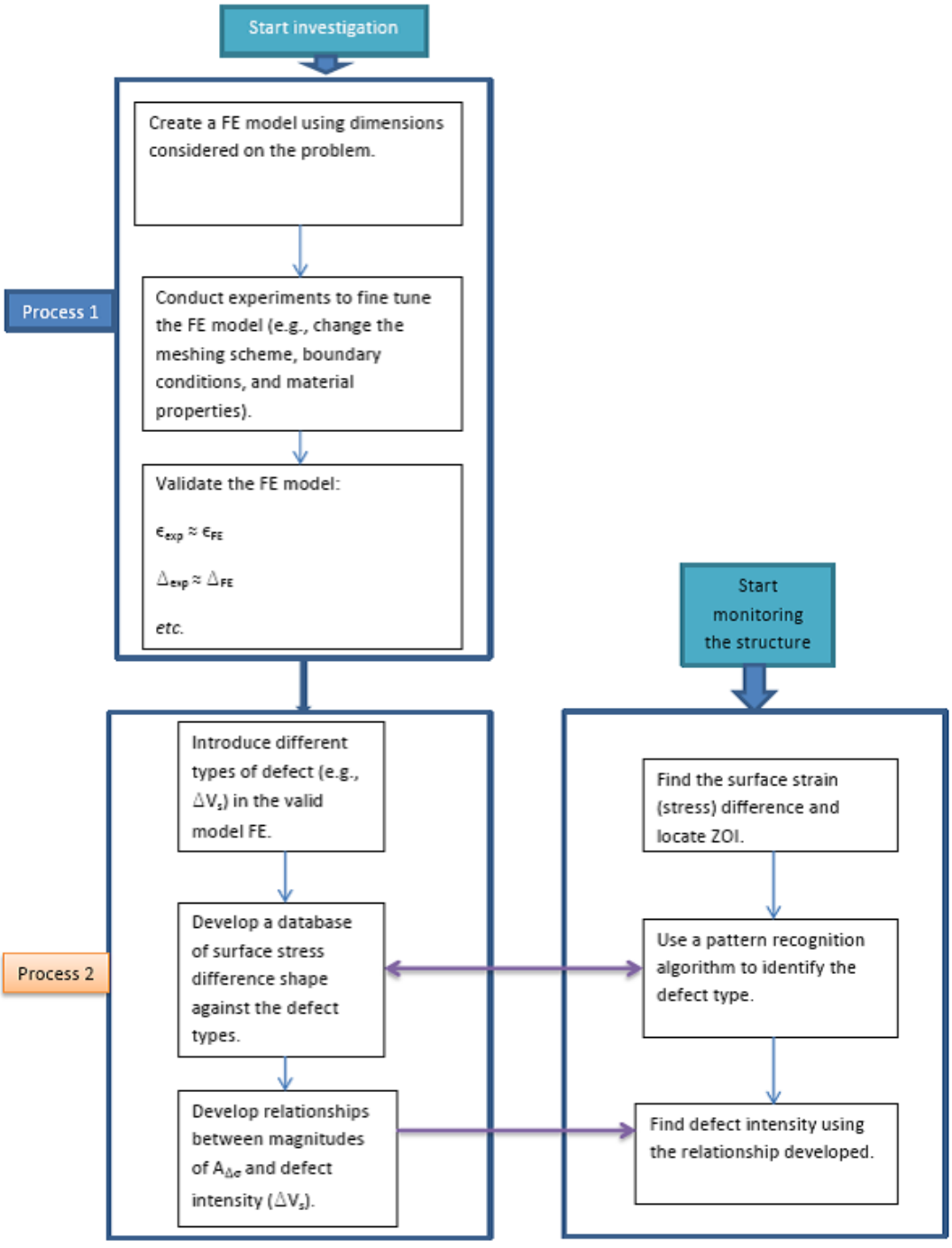

Figure 5-37: Proposed methodology to identify damage in RC structures

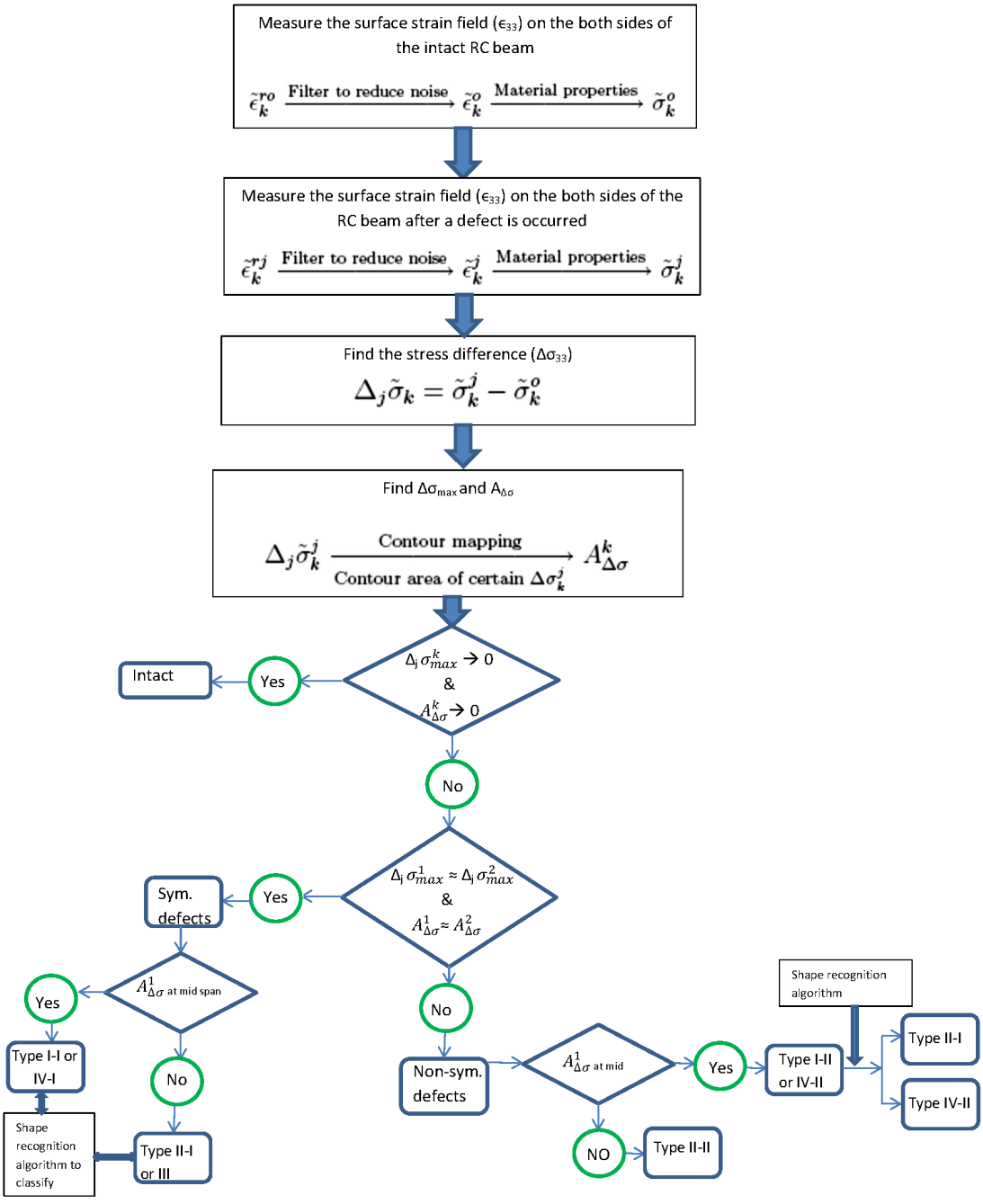

Figure 5-38: Proposed methodology to identify damage type

Chapter 6

Conclusions

In this chapter, research findings, contributions and the future work of this study are reported.

6.1 Research Findings

The research findings of this study are in the following:

- Behavior of a RC beam can be simulated using a commercial FE package ABAQUS®.
- FOS provides consistent measurements of surface strain during four-point bending tests. For example, FOS surface strain measurements during the four point bending test and FE simulation results are in good agreement.
- Simulated RC beam model response reveals that surface stress/strain field of a RC beam changes due to the presence of internal damage.

- Damage introduced in the rebar embedded in a RC beam can be accurately located using the surface stress difference.

- Relationships developed between surface stress-field change (includes σ_{max}, $A_{\Delta\sigma}$) and subsurface damage intensity (ΔV_s) for four damage types (tabulated in Table 6.2 and 6.1) can be used to predict damage intensity.

- Nonsymmetric damages yield more contour area of stress change than the symmetric damages (in Type I, Type II, and Type IV).

- Maximum stress change both in symmetric and nonsymmetric damage scenarios are close (1 ~5% change).

Table 6.1 shows the coefficients of Eq. (6.1) for different damage Types. Table 6.2 shows the coefficients of Eq. (6.2) for different damage types.

$$\Delta V_s = pA_{\Delta\sigma}^3 + qA_{\Delta\sigma}^2 + rA_{\Delta\sigma} + C_1 \tag{6.1}$$

$$\Delta V_s = A\Delta\sigma_{max}^2 + B\Delta\sigma_{max} + C_2 \tag{6.2}$$

Table 6.1: Relationships between $A_{\Delta\sigma}$ and ΔV_s

Damage type	p	q	r	C_1
Type I-I	0.00963	-0.0569	2.1690	0.0139
Type I-II	0.00000	0.0000	1.9220	0.0940
Type II-I	0.02307	0.2155	3.0690	0.0564
Type II-II	0.00000	0.0000	2.3160	0.4188
Type III	0.02307	0.2155	3.0690	0.0564
Type IV-I	0.00200	-0.0416	0.5687	-0.00216
Type IV-II	0.00000	0.0080	0.1800	0.1344

Table 6.2: Relationships between $\Delta\sigma_{max}$ and ΔV_s

Damage type	A	B	C_2
Type I-I	-0.0394	3.4420	0.04076
Type I-II	-0.03449	3.3700	0.04028
Type II-I	-0.05026	4.1590	0.03931
Type II-II	-0.07840	4.3070	0.06134
Type III	-0.07840	4.3070	0.06134
Type IV-I	-0.00208	0.7823	0.00674
Type IV-II	-0.00183	0.7849	0.00622

6.2 Contributions

Internal damage in a singly RC beam can be identified and quantified using the surface stress change. In this study, the simulated response of damaged RC beam models demonstrated relationships between internal damage intensity and surface stress change.

- A damage detection procedure and a methodology are proposed to identify internal damages in a RC structure using its surface strain measurement.
- The relationships established between internal damage intensity and external strain/stress field change can be used to determine artificial internal damage intensity on the rebars using the surface strain measurements.
- Applied FE modelling technique to simulate internal damage for modelling corrosion of steel rebars in RC structures.

6.3 Future Work

- Conduct experiment to confirm surface strain change patterns of RC structures.

- Develop a pattern recognition algorithm using the database of simulated surface stress change patterns vs. damage types to recognize experimental change patterns.

- Explore more damage types (*e.g.* honeycomb in concrete and slippage between concrete and rebars).

Bibliography

[1] S. Alih and A. Khelil. Behavior of inoxydable steel and their performance as reinforcement bars in concrete beam: Experimental and nonlinear finite element analysis. *Construction and Building Materials*, 37:481–492, 2012.

[2] ASTM. ASTM C39/39M-12a : Standard test method for compressive strength of cylindrical concrete specimens. *ASTM International, West Conshohocken, PA, DOI:10.1520/C0039_C0039M-12a, www.astm.org*, 2012.

[3] B. Bay, T. Smith, D. Fyhrie, and M. Saad. Digital volume correlation: three-dimensional strain mapping using X-ray tomography. *Experiential Mech.*, 39:217–226, 1999.

[4] P. Bergan, K. Bathe, and W. Wunjderlich. *Finite Element Method for Nonlinear Problems*. Springer-Verlag, 1985.

[5] B. Bonfiglioli and G. Pascale. Internal strain measurement in concrete element by Fiber Optic Sensors. *Journal of Materials in Civil Engineering ASCE*, 15:125–133, 2003.

[6] B. Cox and D. Marshall. The determination of crack bridging forces. *International Journal of Fracture*, 49:159–176, 1991.

[7] Dassault Systémes, 10 rue Marcel Dassault, CS 40501, 78946 Vélizy-Villacoublay Cedex - France. *Abaqus/CAE User's Manual Version 6.11, http://abaqus.ethz.ch:2080/v6.11/.*

[8] L. Deng and C. Cai. Applications of fiber optic sensors in civil engineering. *Structural Engineering and Mechanics*, 25:577–596, 2007.

[9] J.-F. Destrebecq, T. E., and F. E. Analysis of cracks and deformations in a full scale reinforced concrete beam using a digital image correlation technique. *Experimetal Mechanics*, 51:879–890, 2011.

[10] F. Hild and S. R. Measuring stress intensity factors with a camera: Integrated digital image correlation (I-DIC). *C. R. Mecanique*, 334:8–12, 2006.

[11] L. Hsu and C.-T. Hsu. Complete stress-strain behavior of high-strength concrete under compression. *Magazine of Concrete Research*, 46(169):301–312, 1994.

[12] H. Hu, F. Lin, H. Liu, Y. Huang, and T. Pan. Constitutive modeling of reinforced concrete and prestressed cconcrete structures strengthened by fiber-reinforced plastics. *Composite Structure*, 92:1640–1650, 2010.

[13] D. Kachlakev, T. Miller, S. Yim, and K. Chansawat. Finite element modeling of concrete structures strengthened with FRP laminates. Technical Report FHWA-OR-RD-01-17, Oregon Department of Transportation and Federal Highway Administration, 2001.

[14] M. Kamaya and M. Kwakubo. A procedure for determining the true stressstrain curve over a large range of strains using digital image correlation and finite element analysis. *Mechanics of Materials*, 43:245–253, 2011.

[15] A. Kenel, P. Nellen, A. Frank, P. Marti, and F. ASCE. Reinforcing steel strain measurement by bragging grating sensors. *J. of Mat. in Civil Eng. ASCE*, pages 423–431, 2005.

[16] K. Kesavan, K. Ravisankar, S. Parivallal, P. Sreeshylam, and S. Sridhar. Experimental studies on fiberber optic sensors embedded in concrete. *Measurement*, 43:157–163, 2010.

[17] S. Kubo. Inverse problems related to the mechanics of fracture of solids and structures. *JSME International Journal*, 31, 1998.

[18] D. Lecompte, V. J., and S. H. Crack detection in a concrete beam using two different camera techniques. *Structural Health Monitoring*, 5:59–68, 2006.

[19] K. Lee and J. Han. Fatigue behavior of composite beams with pyramidal shear connectors under repeated loading. *KSCE J. Civil Eng.*, 2:119–118, 1998.

[20] L. Li, Y. Guo, F. Liu, and J. Bungev. An experimental and numerical study of the effect of thickness and length of CFRP on performance of repair reinforced concrete beam. *Constr. Build. Mater.*, 20:901–909, 2006.

[21] M. Maalej, S. Ahmed, K. Kuang, and Paramasivam. Fiber Optic Sensing for monitoring corrosion-induced damage. *Structural Health Monitoring*, 3:165:165–176, 2004.

[22] J. Maeck. *Damage Assesment of Civil Engineering Structure by Vibration Monitoring*. PhD thesis, Katholieke Universiteit Leuven, 2003.

[23] M. Mulle, R. Zitoune, F. Collombet, L. Robert, and H.-Y. Grunevald. Embedded FBGs and 3-D DIC for the stress analysis of a structural specimen subjected to bending. *Composite Structure*, 91:48–55, 2009.

[24] I. Nazmul and T. Matsumoto. Inverse analysis to determine rebars' force from external crack widths measurement. *Journal of Applied Mechanics*, 07:1179–1186, 2004.

[25] I. Nazmul and T. Matsumoto. High resolution COD image analysis for health monitoring of reinforced concrete structures through inverse analysis. *International Journal of Solids and Structures*, 45:159–174, 2008.

[26] B. Peeters, M. Wahab, G. De Roeck, J. Visscher, W. Wild, J. Ndambi, and J. Vantomme. Evaluation of structural damage identification of structural damage by dynamic system identifiction. In *Proceedings of the 21st International Seminar on Modal Analysis*, volume 3, pages 1349–1361. Katholeike Universiteit Leuven, 1996.

[27] N. R. and H. A. Rasheed. Tension stiffening model for concrete beams reinforced with steel and FRP bars. *Journal of Materials in Civil Engineering ASCE*, 18(6):831–841, 2006.

[28] N. Rim and R. Hayder. Tension stiffening model for concrete beams reinfced with steel and FRP bars. *J. of Mat. in Civil Eng.*, 18(6):831–841, 2006.

[29] L. J. Segerlind. *Applied Finite Element Analysis*. John Wiley and Sons, 1984.

[30] H. Sinaei, M. Shariati, A. Abna, M. Aghaei, and A. Shariati. Evaluation of reinforced concrete beam behavior using finite element analysis by ABAQUS. *Scientific Research and Essays*, 7(21):2002–2009, 2012.

[31] B. Wahalathantri, D. Thambiratnam, T. Chan, and S. Fawzia. A material model for flexural crack simulation in reinforced concrete element using ABAQUS. In *The First International Conference on Engineering, Design and Developing the Building Environment for Suitalble Wellbeing*, pages 260–264, Queenland University of Technology, Brisbane, Qld, 2011. Queenland University of Technology.

[32] R. Walter and R. O. William. Description of stress-strain curves by three parameters. Technical Report 902, NASA, NASA scientific and technical information facililies. Washington: NASA, 1943.

[33] Z. Wu, R. H., Z. J., F. Xu, and W. Dong. Experimental investigation on the FPZ properties in concrete using digital image correlation technique. *Fracture Mechanics*, 78:2978–2990, 2011.

[34] W. X., N. Hu, F. Hisao, and Z. Yao. Structural damage identification using static test data and changes in frequencies. *Engineering Structures*, 23:610–621, 2001.

[35] J. Yang and L. Yuan. Package and installation of embedded fiber optic sesnors. *Optics and Lasers in Engineering*, 47:1085–1090, 2009.